SU-SEL-69-065

Interpretation of VLF Signals Observed on the OGO-4 Satellite

by

Rege Romeu Scarabucci

October 1969

Technical Report No. 3418-2

Prepared under
National Aeronautics and Space Administration
Contract NAS 5-3093 and Grant NGR-020-008

RADIOSCIENCE LABORATORY

STANFORD ELECTRONICS LABORATORIES

STANFORD UNIVERSITY · STANFORD, CALIFORNIA

SU-SEL-69-065

INTERPRETATION OF VLF SIGNALS OBSERVED ON THE OGO-4 SATELLITE

by

Rege Romeu Scarabucci

October 1969

Technical Report No. 3418-2

Prepared under
National Aeronautics and Space Administration
Contract NAS 5-3093 and Grant NGR-020-008

Radioscience Laboratory

Stanford University Stanford, California

ABSTRACT

In this report we present and interpret very-low-frequency (VLF) signals observed with the polar orbiting OGO-4 satellite. The VLF signals of interest in this research originate in the air space below the ionosphere and cover the frequency range $\sim$ 0.3 to $\sim$ 30 kHz. The sources are lightning flashes and high-power VLF transmitters. The observations are compared with calculations based on a full-wave treatment of transmission through the lower ionosphere and a ray theory treatment in the upper ionosphere and in the magnetosphere.

In this research we consider several situations related to the propagation of VLF waves. Included are the amplitude of the wave fields when OGO 4 is in the vicinity of VLF stations, two equatorial phenomena corresponding to propagation at low latitudes, and several phenomena observed at mid-high latitudes. The study also includes the differences between daytime and nighttime propagation.

The equations determining the ionospheric wave-field amplitudes of the signals radiated by a ground-based vertical dipole are derived. The equations are based on geometrical factors, on a transmission coefficient through the lower ionosphere given by a full-wave technique, and on a focusing factor which is derived from the analysis of the ray trajectories in the ionosphere. Calculations based on the derived equations agree well with the wave-fields generated by the Omega transmitter (frequency = 12.5 kHz) of Forest Port, New York.

A study of VLF propagation at low latitudes reveals two different phenomena. One effect, called "equatorial erosion," occurs on the dayside and involves frequency-dependent attenuation, with all VLF signals from ground sources eventually disappearing below the level of detectability

as the satellite approaches the equator. The above phenomenon is explained primarily by absorption in the D and E regions of the ionosphere and to a lesser extent by the ray trajectories followed by the waves above the F-region. The other phenomenon, interpreted as "equatorial defocusing" is observed in the nighttime ionosphere and involves abrupt decreases in the intensity of manmade VLF signals. This effect is caused by ionospheric defocusing of VLF rays near the magnetic equator. The defocusing is related to the change of the vertical gradient of ionization that exists near the transition height.

In addition to the equatorial phenomena just described, world-wide measurements of signals from mid-latitude VLF stations show two remarkable phenomena in the conjugate hemisphere. One is an enhancement of the signals in the conjugate region of the transmitter and the other is a high-latitude "erosion" of the signals in the conjugate hemisphere. A detailed study of the ray trajectories in realistic models of the magnetosphere shows that the signals radiated from mid-latitude stations reach the conjugate hemisphere after following trajectories not aligned with the geomagnetic field lines. This study leads to the theory of the prolongitudinal (P-L) mode of whistler propagation. The P-L mode is characterized by propagation with the wave normal inside a characteristic cone relative to the geomagnetic field. The propagation properties of the P-L mode account for the wave-field amplitudes observed in the conjugate region of the transmitters and for almost all whistlers observed by OGO 4 at mid-high latitudes. The high-latitude "erosion" of the downcoming signals is explained by a latitudinal cutoff that occurs for the P-L mode. This cutoff is caused by gradients of electron density inside the plasmasphere and by steep gradients at the plasmapause.

TABLE OF CONTENTS

		Page
I.	INTRODUCTION	1
	A. Objectives	1
	B. The Early Work	1
	C. Brief Description of Experiment 02 Aboard OGO 4	5
	D. OGO-4 Observations	7
	E. Contributions of the Present Work	19
II.	EXCITATION OF WHISTLER-MODE WAVES THROUGH THE LOWER IONOSPHERE	22
	A. Some Properties of the Numerical Full-Wave Method	24
	B. Ionospheric Wave Fields Generated By Ground Transmitters	31
	1. Power Radiated by a Small Vertical Grounded Dipole	33
	2. Transmission in the Lower Ionosphere	34
	3. Focusing Gain	35
	4. The Magnetic Wave Field at the Satellite	37
	C. OGO-4 Amplitude Measurements of Wave Fields in the Vicinity of Ground Transmitters	40
III.	OGO-4 OBSERVATIONS OF EQUATORIAL ABSORPTION AND DEFOCUSING OF VLF ELECTROMAGNETIC WAVES	52
	A. INTRODUCTION	52
	B. THE EQUATORIAL EROSION	56
	1. Qualitative Explanation of the Observation	56
	2. Details of the Analysis	57
	3. Daytime Ray Trajectories Around the Equator	61
	C. Equatorial Defocusing	69
	D. Factors Affecting the Equatorial Defocusing	77
	E. Seasonal Variation of the Equatorial Defocusing	83
	F. Conclusions	85

TABLE OF CONTENTS (cont.)

Page

IV. OGO-4 AMPLITUDE MEASUREMENTS OF SIGNALS GENERATED BY GROUND VLF TRANSMITTERS 87

A. Nighttime Measurements 87

1. Enhancement of the Signals in the Conjugate Region of the Transmitter 90

2. High-Latitude "Erosion" in the Conjugate Hemisphere . 90

3. Equatorial Defocusing 91

4. Enhancement of the Signals in the Hemisphere of the Transmitter 91

5. Rings of Noise in the Auroral Rggion 93

B. Daytime Measurements 93

C. Signals in the Conjugate Hemisphere 99

D. Propagation in a Model Magnetosphere 109

E. Conclusions 124

V. THE PRO-LONGITUDINAL MODE OF WHISTLER PROPAGATION 125

A. Introduction 125

B. High-Latitude Cutoff in the Occurrence of Whistlers 125

C. Whistlers with Latitude-Independent Time-Delay 129

D. Whistlers Received on the Ground 134

E. Conclusions 140

VI. AMPLITUDE FADING 143

A. Introduction 143

B. Amplitude Fading Related to Plasmapause Crossing 143

1. Interference Caused by Multiple Hops Below the Ionosphere 149

2. Interference Caused by Longitudinal Gradients of Ionization 149

3. Interference Caused by Latitudinal Gradients of Ionization 149

TABLE OF CONTENTS (cont.)

Page

C. Conclusions 151

REFERENCES 154

LIST OF TABLES

Table — Page

1 Table for computing wave fields 46

LIST OF ILLUSTRATIONS

Figure		Page
1	Portion of strip-chart displaying demodulated PCM data corresponding to signals received by the stepping receivers and by the phase tracking receiver.....	8
2a	Segments of a continuous strip-chart recorded by OGO 4 on 19 February 1968.....	11
2b	A continuation of Figure 2a.....	12
2c	A continuation of Figure 2b.....	13
3	Ground projection of OGO-4 trajectory for the records of Figures 2a,b,c.....	14
4	The assumed geometry.....	23
5	Three ionospheric profiles a,b,c for the nighttime D-region and the effective collision frequency are shown on the right side of the figure.....	26
6	Transmission coefficients for the penetrating mode, vertical polarization and horizontal polarization at 17.8 kHz.....	29
7	Variation of the polarization of the penetrating mode along the meridian.....	30
8	Ray-trajectory between a ground VLF transmitter and a satellite.....	32
9	Tube of rays and geometrical parameters for determining the focusing gain.....	36
10	Variation of angles as functions of the distance for an ionosphere whose height is 90 km.....	39
11	Combination of PCM and analog data from OGO 4.....	41
12	OGO-4 trajectory for the records of Figure 11.....	43
13	Receiving latitudes of rays and the corresponding longitudinal refractive index for waves of 12.5 kHz as a function of the input latitude.....	45
14	Transmission coefficients at 12.5 kHz along the meridian..	48
15	Comparison between calculated and OGO-4 observations of magnetic field amplitude of 12.5 - 12.6 kHz signals transmitted by Omega (New York).....	49

Figure		Page
16	Frequency-time spectra of broadband VLF data from OGO 4 showing a typical example of daytime "equatorial erosion"	53
17	OGO-4 records showing the NAA magnetic field amplitude as measured by the satellite phase-tracking receiver in two consecutive equatorial crossings	54
18	Height distributions of electron density at midday equinox and electron collision frequency	59
19	Daytime equatorial model of the ionosphere above 100 km	60
20	Total ionospheric loss (reflection plus absorption) as a function of magnetic latitude for several frequencies	62
21	Ray trajectories for 1 kHz waves in the equatorial ionosphere using the electron-density model of Figure 10	63
22	Input latitudes at 120 km and the related latiuudes where 1 kHz rays will be detected by a 600 km polar-orbiting satellite	65
23	Ionospheric loss observed by a 600 km polar-orbiting satellite as a function of latitude	68
24	Typical daytime and nighttime ray trajectories followed by waves of 17.8 kHz near the magnetic equator	70
25	Correspondence between the latitudes where the rays leak from the earth's waveguide and the latitude where they will be detected by a satellite whose height is h_s	72
26	The continuous curves show the focusing gain as a function of the satellite latitude calculated for two different satellite heights	74
27	Lower-ionosphere transmission coefficient for penetrating mode waves traveling southward	77
28	Three ionospheric models A, B, and C	79
29	Correspondence between the latitudes where the rays leak from the earth's waveguide and the latitude where they will be detected by a satellite at 700 km for the two ionospheric models B and C	81
30	The continuous curves show the focusing gain as a function of the satellite latitude for ionospheric model B	82

LIST OF ILLUSTRATIONS (cont.)

Figure		Page
31	Position of the defocusing region relative to the magnetic equator	84
32	OGO-4 amplitude measurements of NAA signals at 17.8 kHz	88
33	OGO-4 trajectories for Figure 32	89
34	OGO-4 record displaying the high-latitude "erosion" phenomenon	92
35a	OGO-4 stip-chart recorded on 19 November 1967	95
35b	Continuation of the strip-chart shown in Figure 35a	96
35c	Continuation of the strip-chart shown in Figure 35b	97
36	Ground projection of satellite trajectory for Figures 35a, b, and c	98
37	Geometry assumed for the two-dimensional ray equation	103
38	Ray trajectories in a latitudinally constant magnetosphere and in a magnetosphere presenting an increasing trend of ionization toward the equator	108
39	Geometry for developing the equations of ionization oriented along the field lines	112
40	Electron density at 1000 km as a function of latitude for the model magnetosphere	114
41	The equatorial ionization profile of the assumed magnetospheric model	115
42a	Ray-trajectory for 17.8 kHz waves that start with vertical wave-normal at 120 km height and at 58^{o} latitude	116
42b	Latitudinal behavior of the angle between the geomagnetic field and the wave-normal of the 17.8 kHz wave corresponding to the ray path of Figure 42a	117
43	Arrival latitude and corresponding travel times for waves of 17.8 kHz as a function of the input latitude in the northern hemisphere	121
44	Details of the last descending part of the ray that produces the high-latitude cutoff of NAA waves	123
45	Arrival latitudes as a function of input latitudes in the northern hemisphere for waves from 1 to 20 kHz	126

LIST OF ILLUSTRATIONS (cont.)

Figure		Page
46	Travel times as a function of the receiving latitudes.....	130
47	Predicted "hook" whistler to be received at 500 km height and at -52^{o} latitude.....	131
48	Pieces of the OGO-4 record displayed in Figure 34.....	133
49	Horizontal component of the refractive index for down-going waves in the southern hemisphere at 120 km height as a function of input latitude.....	135
50	Range of latitudes where whistler frequencies of 1.0, 2.5, 5.0, 7.5, 10.0, 12.5 and 15.0 kHz present $\lvert\mu_H\rvert \leq 1$.....	137
51	Magnetic field amplitude of NAA signal and 0 to 12.5 kHz broadband spectrum as functions of time UT and L value of OGO 4.....	144
52	Repetition of the features displayed in Figure 51 for 21 September 1968.....	145
53	Ground projections of the two OGO-4 trajectories corresponding to the records of Figures 51 and 52.....	146
54	Receiving latitudes at 600 km for rays that start between the input latitudes of 59.95^{o} and 60.35^{o}.....	152

ACKNOWLEDGMENTS

The author is greatly indebted to Professor R. A. Helliwell for his guidance and stimulating discussions during the course of this research. The author also wishes to express his appreciation to Dr. R. L. Smith and Dr. J. J. Angerami for their interest and helpful criticisms. The assistance and encouragement of Mr. John Katsufrakis in supplying experimental data for this research, and the assistance of Mr. Ken Howell in the interpretation of the data are gratefully acknowledged.

This research was supported by the National Aeronautics and Space Administration under contract NAS 5-3093 and grant NGL-05-020-008. Support of the National Science Foundation through the Office of Computer Sciences under grant NSF GP-948 is also acknowledged.

The research was carried out under a graduate student research assistantship awarded by Stanford University and a scholarship awarded by C.N.A.E. - Brazil.

I. INTRODUCTION

A. OBJECTIVES

The main purpose of this research is to present and interpret measurements of very-low-frequency signals observed with the low-altitude, polar-orbiting, OGO-4 satellite. The interpretations of the measurements are based on amplitude and spectrum analysis of the received signals as well as on the related position of the satellite. The phenomena to be discussed in this research are observed on nearly all revolutions of OGO 4. The present study is mainly concerned with signals generated on the ground by lightning strokes and by VLF transmitters.

This research may also be classified as a global study of very-low-frequency propagation in the ionosphere and in the magnetosphere of the earth. It includes the general problem of excitation of waves through the lower ionosphere under different conditions and the characteristics of propagation inside the anisotropic plasma above the earth. The study covers a variety of situations, including signals received when OGO 4 is relatively close to the ground sources and signals received at low, middle, and high latitudes. The differences between daytime and nighttime propagation are also included in this study.

B. THE EARLY WORK

The burst of current produced during a lightning flash involving a cloud-to-cloud or cloud-to-ground electric discharge radiates electromagnetic energy like an electric dipole. The surge of current whose duration is of the order of 100 milliseconds radiates a large spectrum of waves extending from a few Hertz up to about 20 MHz. These waves are heard as clicks in radio receivers tuned to any frequency inside the

above band and correspond to the power spectrum radiated in the pass-band of the receiver. The radiated waves (whose spectrum usually peaks between 5 and 10 kHz) enter the ionosphere and travel inside the magnetosphere following curved trajectories. The wave components radiated by the lightning source travel with different velocities because the magnetosphere is a dispersive medium, and finally they may penetrate the air space below the ionosphere in the conjugate hemisphere. When reproduced in audible form these wave components usually sound like whistling tones of steadily falling pitch, known simply as "whistlers." Whistlers represent a valuable tool for studying properties of the magnetosphere because some of the whistler characteristics are directly related to ionization and gradients of ionization that exist in the magnetosphere.

The first successful study of whistlers based both on experimental observations and on theoretical treatment was presented by Storey [1953]. Since then the number of publications concerning the propagation of VLF waves in the magnetosphere has increased steadily. Substantial contributions to the understanding of whistlers and related phenomena have been provided by the VLF Group of Stanford University during the last 15 years [Helliwell, 1965].

Storey [1953] showed that if the frequencies of the whistler components were much smaller than both the electron gyrofrequency and the plasma frequency along the whistler path, then the whistler-packet should travel approximately along the earth's magnetic field. Under the above circumstances the maximum departure of the rays relative to the fieldlines would be $19^{o}29'$. Storey also observed long trains of echoing whistlers that presented very low amplitude decrement from each

whistler to the corresponding echo. He suggested that ionospheric irregularities like columns of auroral ionization could have a guiding effect on the waves and thus explain the low amplitude decrement.

Helliwell et al. [1956] reported whistlers whose frequency-time spectrum presented a rising and a falling branch connected together at a frequency of minimum delay time relative to the causative lightning discharge. These whistlers are known as "nose" whistlers and the frequency of minimum delay is called the nose frequency. The authors showed that the whistler dispersion was explained by the magnetoionic theory when the frequency components of the whistlers were permitted to be comparable to the electron gyrofrequency along the whistler path in the magnetosphere.

Smith et al. [1960] developed quantitatively the existing ideas of magnetospheric ducting, proposing a theory of trapping of whistlers in field-aligned ducts of enhanced ionization. Smith [1961a] presented some evidence of ducted propagation and showed that the theory of trapping also predicted a cutoff frequency of approximately one-half the minimum gyrofrequency along the whistler path.

Since then whistlers have been used to measure the profile of electron density at the equator. The method is based on finding the propagation trajectories of the whistlers from their nose frequencies [Helliwell, 1961; Smith, 1961b, Carpenter, 1962].

In a study based on whistlers Carpenter [1963] showed that the electron distribution in the magnetosphere does not fall off smoothly. He frequently found an abrupt decrease of electron density usually at fieldlines with an equatorial radius of about 4 earth radii. This very steep decrease of ionization, known as the plasmapause, exhibits inward/

outward motions related to the geomagnetic activity and is a permanent feature of the magnetosphere.

With the advent of the space age new tools became available for the study of whistler-mode propagation. It was then possible to observe whistlers inside the magnetosphere before they reached the low region of the ionosphere where they can be reflected, transmitted or absorbed by the medium. Similarly it was possible to observe whistlers that do not return to the earth. With satellite measurements new forms of whistlers were observed in the magnetosphere, namely the "subprotonospheric" whistler [Carpenter et al., 1964], the "ion cyclotron" whistler [Gurnett et al., 1965], the "helium" whistler [Barrington et al., 1966], the "magnetospherically reflected" and the "Nu" whistler [Smith and Angerami, 1968], the "ion cutoff" whistler [Muzzio, 1968], and the "walking-trace" whistler [Walter and Angerami, 1969].

The satellite age also brought the possibility of controlled experiments in VLF propagation by means of satellite observations of signals transmitted by ground-based U. S. Navy stations. VLF waves were first observed in the magnetosphere in 1961 by the Lofti-I satellite [Leiphart et al., 1962]. In this experiment VLF signals were received from the U. S. Navy stations, NBA (24 kHz) in the Canal Zone and NPG (18.6 kHz) in Jim Creek, Washington. A number of features of the data were interpreted by Rorden et al. [1964].

Observations aboard OGO 1 and OGO 2 of whistler-mode waves generated by U. S. Navy stations were reported by Heyborne [1966]. He found several interesting features presented by the VLF signals from NPG and NAA, both located in the northern hemisphere. He observed a northern hemisphere latitudinal cutoff in the amplitude of the signals; reception

of whistler-mode signals in the southern hemisphere at latitudes "forbidden" by the theory of cutoff at one-half of the gyrofrequency [Smith, 1961a]; an amplitude cutoff at high latitudes in the southern hemisphere; and a dip of field intensity over the geomagnetic equator.

Storey [1966] described the main features of the French satellite FR-1 and presented some preliminary results from wave-field measurements of VLF signals transmitted by NBA in the Canal Zone and by FUB (16.8 kHz) in Sainte Assise, France. FR-1 was able to measure the wave-normal direction of the waves. For example, an important result from FR-1 reported by Aubry [1967, 1968], is that the wave normals of the waves generated by FUB and received at midlatitudes in the northern hemisphere are directed toward the equator. Sometimes the wave normal is tilted toward the equator by more than 50° with respect to the vertical at 750 km. He interpreted the phenomenon in terms of horizontal gradients of electron density that effectively bend the waves toward regions of higher ionization.

C. BRIEF DESCRIPTION OF EXPERIMENT 02 ABOARD OGO 4

The Orbiting Geophysical Observatory OGO 4, is a multi-experiment satellite that was launched into a polar orbit in July 1967. The orbit period is of the order of 100 minutes, the height varies from approximately 400 to 900 km and the orbit inclination is 86°. OGO 4 carries more than 20 different experiments, one of which will be described briefly below.

The Stanford University/Stanford Research Institute experiment aboard OGO 4 consists of a loop antenna, a broadband preamplifier that drives three stepping receivers, two broadband receivers, and one phase-tracking receiver. The loop antenna may effectively work as an electric

or as a magnetic field sensor depending on the position of switches suitably placed at the antenna and at the input of the preamplifier. All the measurements shown in this report were taken when the loop antenna was working as a magnetic antenna. The VLF spectrum covered by the broadband preamplifier ranges from 30 Hz to 100 kHz. The stepping receivers (No. 1, No. 2, and No. 3) operate together, the tuning frequency for Band 3 being 8 and 64 times the tuning frequencies for Band 2 and Band 1, respectively. The stepping receivers provide the following amplitude measurements of the electric or magnetic wave fields.

	Frequency range	3 db bandwidth
Band 1	130 - 1560 Hz	± 20 Hz
Band 2	1.05 - 12.5 kHz	± 75 Hz
Band 3	8.4 - 100 kHz	± 250 Hz

Each band may be tuned to one of 256 different frequencies when operating in fixed-frequency mode or the stepping receivers may sweep in frequency from the bottom to the top of each band in 256 successive steps when operating in the sweeping mode.

The broadband receivers provide spectral information in the range 30 to 300 Hz (ELF channel) and 0.3 to 12.5 kHz (VLF channel).

The phase tracking receiver measures amplitude and phase of waves in the range 14 to 27 kHz. The phase of the arriving wave is measured by comparison with the phase of a stable spacecraft oscillator and the amplitude is measured in a sharp-edged passband of ±25 Hz that falls approximately 30 db at ±50 Hz from the tuned frequency.

Amplitude measurements with the phase tracking receiver and the stepping receivers are telemetered to ground in a form of pulse-code-modulated (PCM) signals. The signal may be sampled in a low bit rate

(4 kbit/sec) which is suitable for tape storage inside the spacecraft or it may be sampled in a high bit rate (64 kbit/sec) when telemetering in "real time" to ground.

The amplitude and the spectrum content of the signals received by the broadband receivers are telemetered in analog form and in real time to ground. The signal is log-compressed in amplitude and then used to modulate a voltage-controlled-oscillator (VCO) between 15 and 20 kHz. The spectrum content is obtained after the signal is fed into a saturating clipper and its output filtered to retain frequencies between 30 Hz to 12.5 kHz. The VCO has several uses, namely it can be modulated by the amplitude of the ELF and VLF channels and also by the output of the stepping receiver No. 3. (In this case, therefore the telemetry of the stepping receiver No. 3 is obtained in analog form.)

Experiment 02 onboard OGO 4 is nearly similar to the corresponding experiment carried onboard OGO 2. More details about the equipment can be found in a publication prepared for OGO 2 by Ficklin et al. [1965].

D. OGO-4 OBSERVATIONS

A systematic coverage of VLF phenomena throughout the world is obtained by recording continuously the signals from the stepping receivers and the phase tracking receiver onboard the satellite. In the course of the present research the interpretations of several phenomena have been initiated by observing the data from these four receivers. We start with a discussion related to the kind of measurements that are basic in this work and the global features presented by the OGO-4 receivers during a complete revolution of the satellite.

Figure 1 shows a portion of a strip-chart displaying PCM data

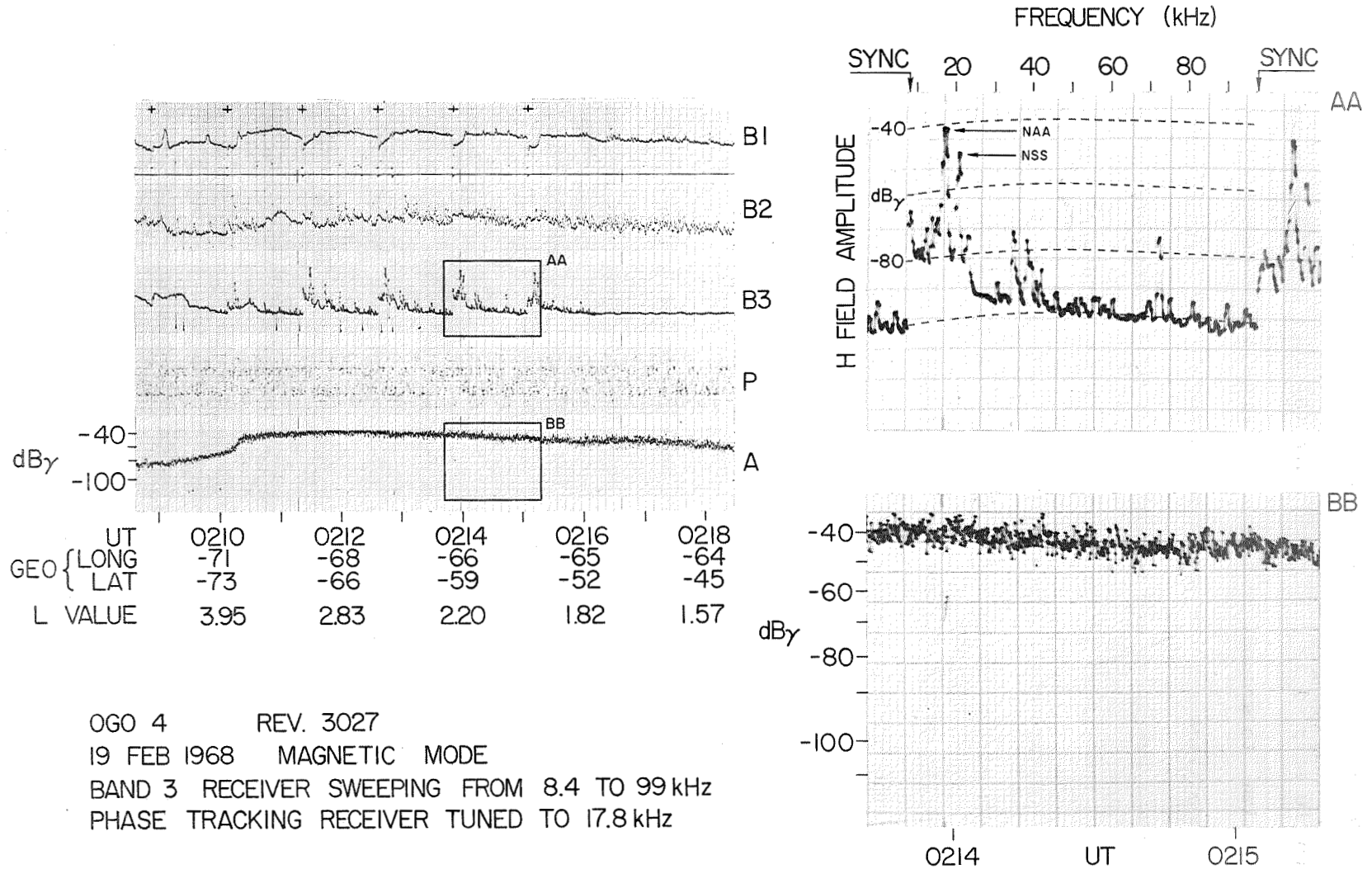

Figure 1. Portion of strip-chart displaying demodulated PCM data corresponding to signals received by the stepping receivers (B1, B2, B3) and by the phase tracking receiver (P and A).

stored by OGO 4 and subsequently received by tape-dumping at the telemetry station in Rosman, North Carolina. Five records are illustrated, reading from top to bottom: outputs of Band 1 (B1), Band 2 (B2), and Band 3 (B3) of the stepping receivers operating in the sweeping mode, phase (P), and amplitude (A) of the phase tracking receiver. Nearly 10 minutes of PCM data are shown as a function of universal time (UT), geographic position, and the L value of the satellite. Small crosses above the Band 1 record show the position of synchronizing pulses where each frequency sweep starts. The 256 steps of each sweep occur during an interval of 73.6 seconds. At about 0216 UT the stepping receivers were switched to a fixed mode of operation commanded by the telemetry station at Santiago, Chile.

The phase tracking receiver is tuned to NAA at 17.8 kHz. The phase P is useless when the transmission mode of operation is CW or FSK (the present case) because the phase is random during the Morse code intervals corresponding to "no signal" (CW) or "another frequency" (FSK). The phase may be useful during intervals of key-down mode transmission. The phase and the amplitude of the phase tracking receiver are each sampled 512 times in each 73.6 sec interval. The magnetic field of the waves is measured in db relative to 1 gamma, represented here by the symbol dbγ. Gamma is related to ampere/meter by

$$1\gamma = \frac{1}{4\pi \times 10^{2}} \text{ Amp/m} = 7.9577472 \times 10^{-4} \text{ Amp/m} \qquad (1.1)$$

The data recorded by the stepping receivers and by the phase tracking receiver are independently processed. This fact is very important for interpreting the measurements correctly. For example, if

a reasonable value of wave field is measured by the phase tracking receiver then a spike must appear at the corresponding frequency during the sweep of Band 3. This is shown on the right side of Figure 1 where two rectangular segments of B3 and A are displayed on an expanded scale. Observe that the NAA signal measured by the phase tracking receiver is easily recognized by a spike of the same amplitude recorded by the stepping receiver No. 3 at 17.8 kHz. It is also possible to observe the signal transmitted by NSS at 21.4 kHz.

The presence of noise is easily detected by the stepping receivers when, instead of spikes, a continuous curve is displayed during the sweep. For example, Figure 1 shows that at 0210:30 UT the NAA signal is detected by the phase tracking receiver as recognized by the corresponding spike at B3. However, the sweep starting at about 0209 UT exhibits a continuous amplitude behavior denoting a band of noise that goes from about 13 kHz to 50 kHz. Therefore the amplitude measured at A is noise and not signal from NAA.

PCM data of a complete revolution of OGO 4. Figures 2a to 2c show portions of a continuous strip chart corresponding to 139 minutes of PCM data stored by OGO 4 on 19 February 1968 between 0017 and 0236 UT. The onboard tape recorder began to store data just after tape dumping at the telemetry station at Orroral, Australia; later at 0236:30 UT the stored data were telemetered to Rosman, North Carolina. The ground projection of the satellite trajectory is superimposed on the mercator projection of world shown in Figure 3. The numbers on the satellite trajectory indicate times (UT) of interesting events which will be discussed below.

Figures 2a to 2c show the amplitudes of the three stepping receivers,

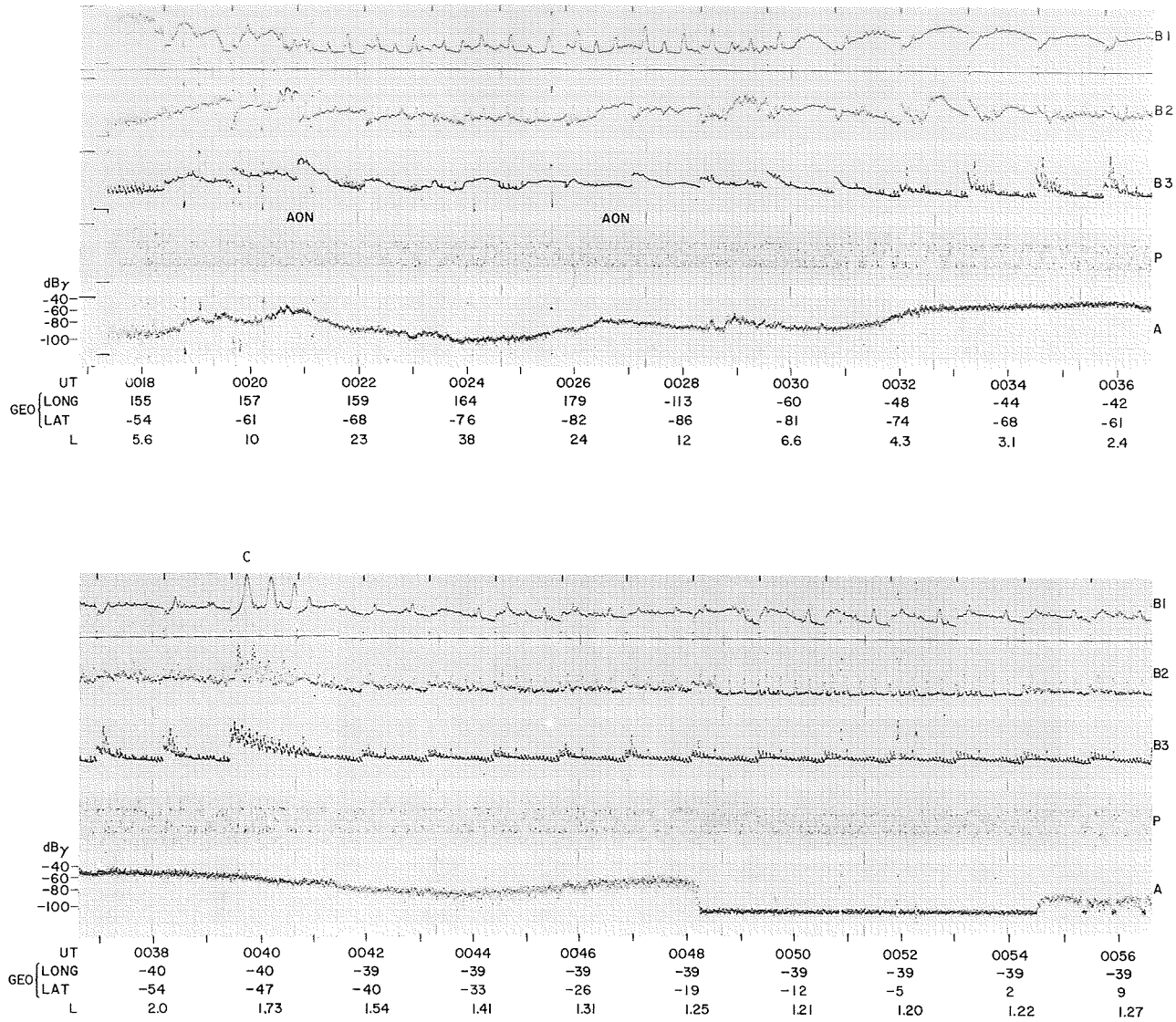

Figure 2a. Segments of a continuous strip-chart recorded by OGO 4 on 19 February 1968. B1, B2, B3 are the amplitudes of the stepping receivers operating in sweeping mode as indicated in Figure 1. The phase tracking receiver (P and A) was tuned to NAA at 17.8 kHz. C denotes a calibration sweep which occurs after 16 consecutive sweeps.

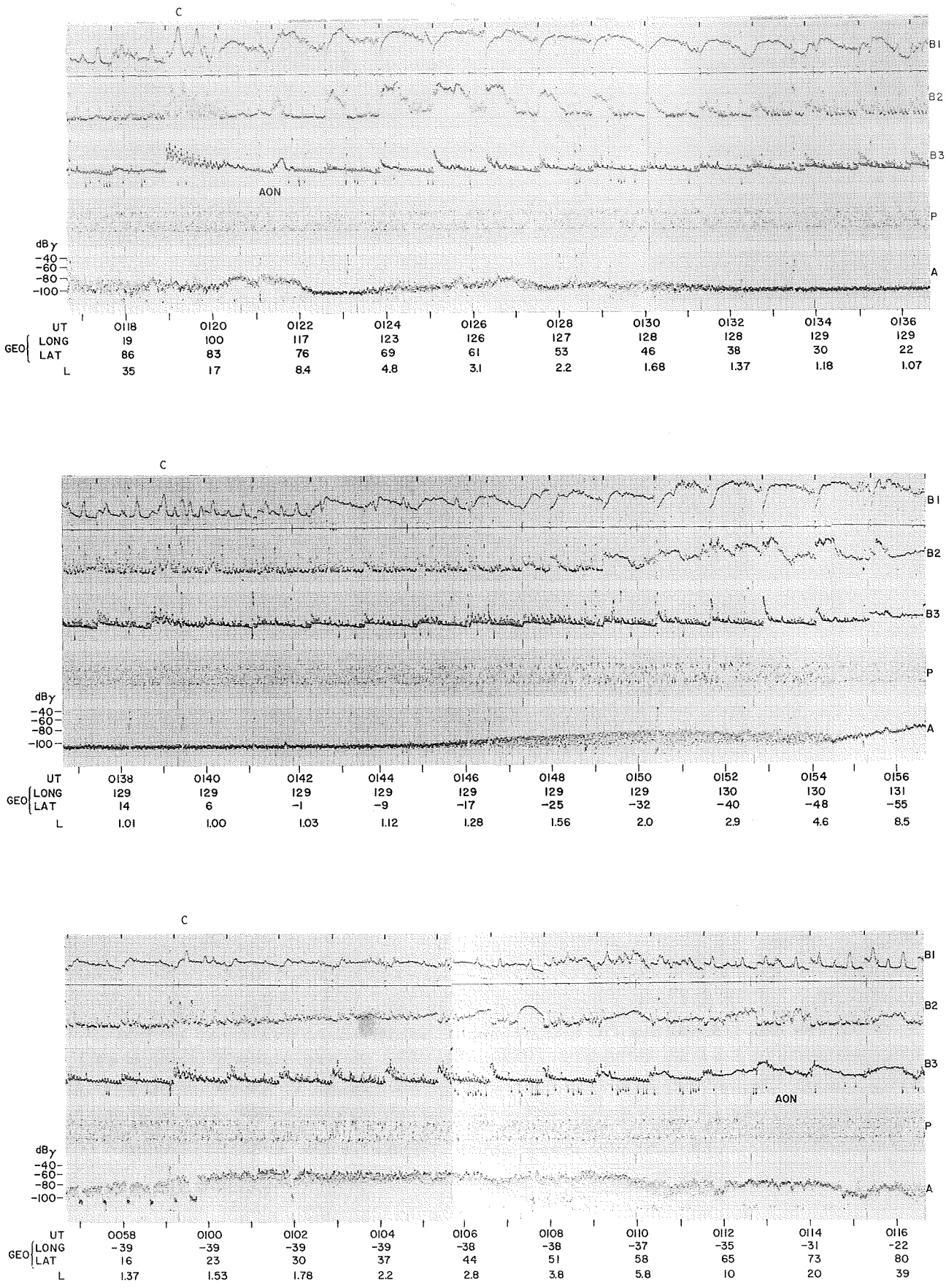

Figure 2b. A continuation of Figure 2a.

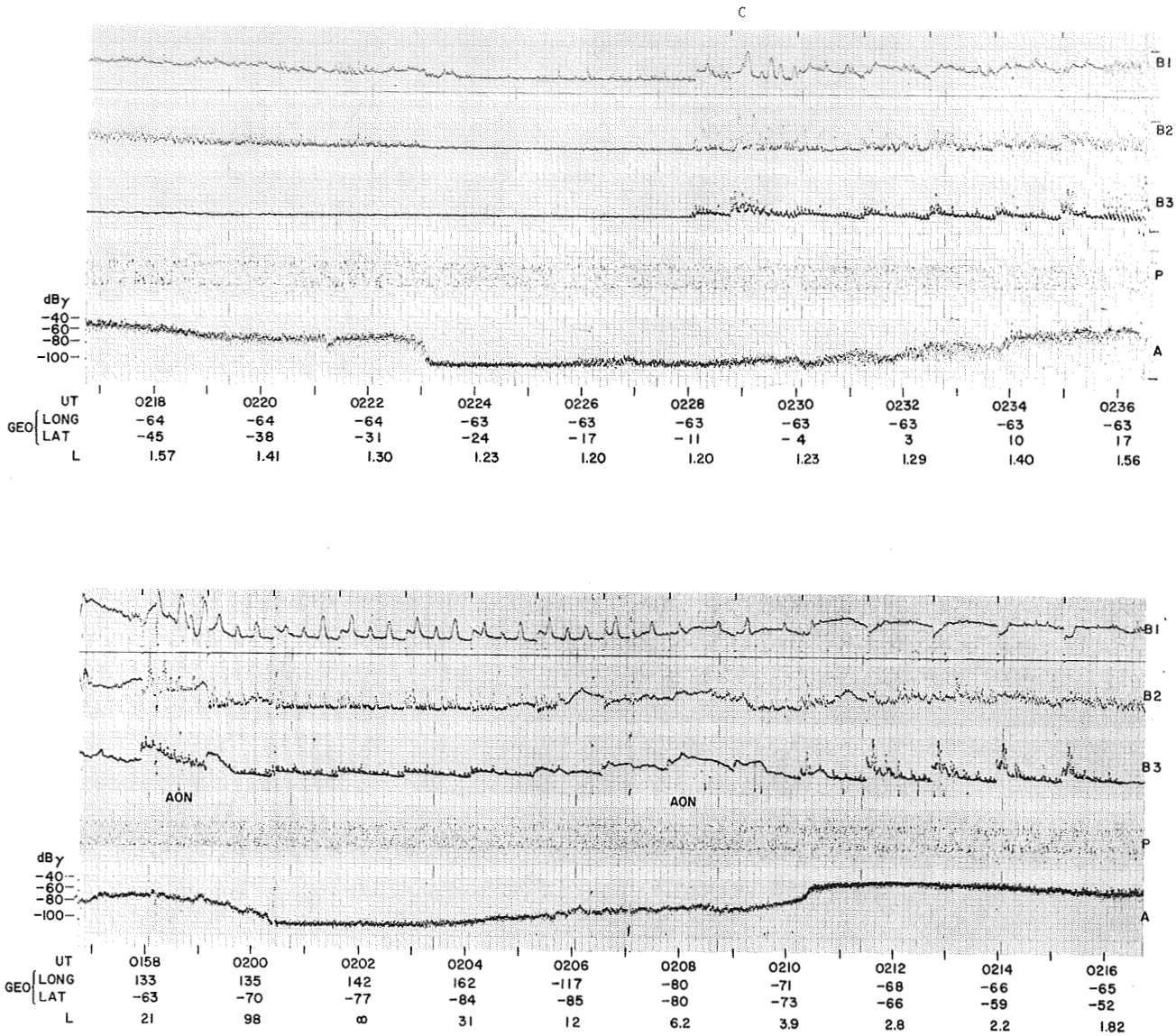

Figure 2c. A continuation of Figure 2b.

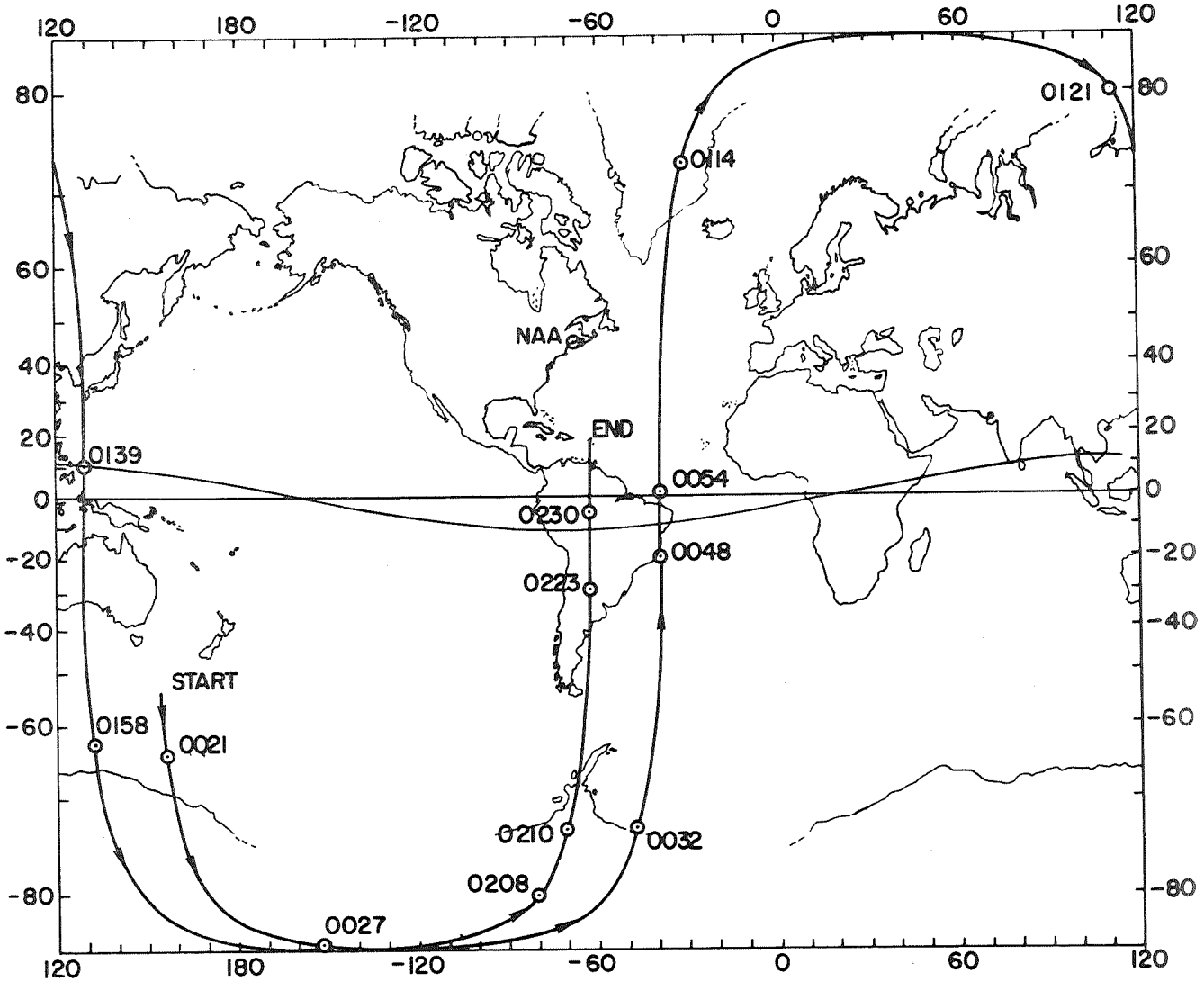

Figure 3. Ground projection of OGO-4 trajectory for the records of Figures 2a,b,c.

B1, B2, and B3, operating in the sweeping mode and the phase (P) and the amplitude (A) of the phase tracking receiver tuned to NAA at 17.8 kHz. The synchronizing pulses for the band receivers are represented by vertical bars in the top record B1. The main features presented by B1, B2, B3 and A are discussed below.

1) Low latitude observations.

The signal levels from mid-latitude VLF transmitters decrease at low latitudes. There is an abrupt decrease of signal at nighttime equatorial crossings as shown in Figure 2a between $\sim$ 0048 and $\sim$ 0054 UT and in the subsequent pass between 0223 and $\sim$ 0230 UT (Figure 2c). The geographic positions of these regions where the NAA signal drops below the threshold level of the equipment is shown in Figure 3. There is an absence of signal in B2 and B3 while B1 measures some signal below $\sim$ 1 kHz. There are spikes in the stepping receivers corresponding to interference lines that appear when the external signal level is very low. The common interference lines for B1 are 400, 800, and 1200 Hz corresponding to harmonics of the power supply line at 400 Hz. For B2 the interference lines are harmonics of the spacecraft dc converters at 2461 kHz. The interference in B3 are odd harmonics of 2461 kHz. Measurements in real time with the broadband receiver indicate the presence of whistlers at these low latitudes during the night. The reason for the total absence of signals in B2 and B3 is because these whistlers present small dispersion at the higher frequencies and therefore they are ignored by the low sampling rate of the equipment.

During daytime equatorial crossings the signal from the transmitter situated in the nightside decreases progressively and goes below the detectability level as the satellite approaches the equator (see

Figure 2b about 0139 UT and the satellite position in Figure 3). B1, B2, and B3 follow the same pattern of A, as shown in Figure 2b. Observe that the decrease of the external signal level is quite marked in B1. When real time data are analyzed the above effect is manifested by a progressive disappearance of the high frequencies of whistlers as the satellite approaches the equator. There is a complete absence of signals in satellite records obtained near the magnetic equator during daytime.

2) Mid-latitude observations.

There is an enhancement of signals transmitted by mid-latitude VLF stations and received by the satellite at mid-latitudes in both hemispheres. In the hemisphere of the VLF transmitter a maximum signal is received when the satellite is nearly east-west from the transmitter (see Figure 2a about 0104 UT for nighttime and about 0127 UT when the satellite is in the dayside over Russia). These signals reach the satellite from below, after traveling inside the ground-ionosphere space from the transmitter to the foot of the ray trajectory between the low-ionosphere and the satellite. In the conjugate hemisphere of the transmitter the signals that reach the satellite coming from above are much stronger than signals excited from below. (This was checked by measuring the travel times of signals.) Therefore the signal levels observed in the conjugate hemisphere are related to fields measured in the hemisphere of the transmitter. Enhancements of NAA signals in the southern hemisphere are observed at $\sim$ 0038 UT and in the succeeding revolution at $\sim$ 0214 UT (both in the nightside) and $\sim$ 0150 UT (dayside) when the satellite is over Australia.

The signal level in Band 1 and Band 2 increases toward mid

latitudes on both sides of the equator, and also for both dayside and nightside (see B1 at left and right of 0052 UT (nightside) and 0139 UT (dayside)). The signal behavior in B1 and B2 is characterized by scattered points caused by the reception of whistlers. The whistler energy that lies inside the bandwidth of the sweeping receiver is more efficiently sampled at mid-latitudes where downgoing whistlers present greater dispersion. Some noise probably is also present inside B1 and B2 at mid-latitudes but this noise is masked by the reception of whistlers. Whistler energy is also observed in fewer cases by B3 at mid-latitudes. The spikes related to whistlers are different from those related to signals transmitted from VLF stations because in this last case the spikes remain at the same frequency for all sweeps.

3) High-latitude observations.

There is a high-latitude cutoff in the intensity of the signals from mid-latitude transmitters observed in the conjugate hemisphere (see the cutoff in amplitude A of the NAA signal at 0032 UT and in the following revolution of OGO 4 at 0210 UT). The phenomenon is well documented by the disappearance at higher latitudes of the NAA spike in B3. The high-latitude cutoff in the conjugate hemisphere of the transmitter is also detected in the dayside (see Figure 2b at 0154 UT) although in this case the cutoff is less pronounced.

The high-latitude cutoff in the conjugate hemisphere of NAA is in fact a particular case of a more general phenomenon detected in every OGO-4 pass, namely a high-latitude "erosion" of downgoing whistlers. The cutoff in the occurrence of whistlers at high latitudes is more easily observed with the broadband receiver. However it can be reasonably observed in Figure 2c near 0210 UT: as the signal of NAA decreases

the signal in B2 disappears and the signal in B1 progressively decreases toward higher latitudes (to the left of 0210 UT). This effect converted to whistler observation means that the downgoing whistlers are "eroded" at high latitudes with the higher frequencies disappearing first as the observation goes from mid latitude to the nearest pole. Disregarding the occurrence of well-localized auroral noise AON (discussed below) the stepping receivers exhibit typically empty bands in polar regions (see B1, B2, and B3 about 0024, 0117, and 0202 UT).

In every revolution of OGO 4 it is possible to identify two rings of intense noise around each magnetic pole. The same ring is crossed twice during each high-latitude pass. The regions labeled AON in Figures 2a, b, and c stand for auroral oval noise. This noise has a typical spectrum ranging from 2 - 5 kHz to above 50 kHz, but the intensity of the noise seems to depend upon the zenith angle of the sun. AON's are observed in the southern hemisphere near 0021 and 0027 UT and in the succeeding revolution of OGO 4 near 0158 and 0208 UT. In the northern hemisphere AON's are observed near 0114 and 0121 UT. The amplitude of this auroral noise in the 50 Hz bandwidth of the phase tracking receiver is very intense as shown in the record of amplitude A just below the AON symbols in Figures 2a, b, and c.

In the hemisphere of the mid-latitude transmitter there is also a high-latitude decrease in the intensity of the upgoing signals related to the position of the AON. In this case the signal from a powerful VLF transmitter competes with the AON level and the signal returns when the satellite crosses the polar region. Observe for example the decrease of the NAA signal as the satellite moves northward at 0112 UT. A close observation of B3 indicates that the NAA spike

competes with the noise level near 0113 to 0116 UT and the signal from NAA remains (although in a somewhat irregular fashion) when the satellite crosses the polar region near 0117/0119 UT.

E. CONTRIBUTIONS OF THE PRESENT WORK

In this research the excitation of VLF waves through the lower ionosphere is studied by means of a "full-wave" treatment of the wave equations. The related computer program is fully discussed in a report by Scarabucci [1969].

The wave fields set up by VLF stations in the nearby ionosphere of the transmitter are calculated by means of the full-wave computer program and a ray-tracing computer program developed by Walter [1969]. It is shown that very good agreement is obtained between calculated and measured signal levels (Chapter 2).

A study of VLF propagation at low latitudes reveals two different phenomena. During daytime equatorial propagation is dominated by collisional absorption in the lower ionosphere which increases sharply at lower latitudes. This effect is manifested by a complete disappearance from satellite records at low latitudes of all signals originating on the ground. During nighttime the collisional absorption is less important and it will be shown that in this case the propagation is highly dependent upon the change of vertical gradient of electron density at the $[O^+ - H^+]$ transition height. These vertical gradients of ionization produce defocusing of VLF waves near the equator. The above equatorial phenomena are discussed in Chapter 3.

In Chapter 4 a simple interpretation of the amplitude measurements in the conjugate hemisphere of NAA also justifies several properties of

commonly received whistlers aboard OGO 4. It is shown that the VLF signals radiated by mid-latitude stations are received at mid-high latitudes in the conjugate hemisphere after following a trajectory that is not aligned with the geomagnetic fieldlines. A ray that starts at high latitudes travels inward, crosses the equator at relatively low heights and follows a descending path toward high latitudes in the conjugate hemisphere. This ray behavior is demonstrated by a realistic model of magnetosphere that includes latitudinal gradients of electron density. A detailed study of ray trajectories in the magnetosphere leads to the theory of the "pro-longitudinal" (P-L) mode of whistler propagation. The P-L mode is characterized by propagation with the wave normal of the waves inside a characteristic cone relative to the geomagnetic field, producing travel times and downgoing wave normals that are typical of purely longitudinal propagation along the field-lines. The P-L mode accounts for almost all whistlers received by OGO 4 at mid-high latitudes and also provides a possible interpretation for certain whistlers received on the ground.

The high-latitude cutoff of downgoing signals is interpreted as a result of the existing gradients of electron density inside the plasma-sphere and the steep gradients at the plasmapause. The calculated cutoff follows very closely the satellite observations (Chapter 5).

Finally a class of deep fading in the amplitude of wave-fields set up by ground-based VLF transmitters is tentatively explained in Chapter 6.

An important result of this research and one strongly suggesting further studies is that the P-L mode predicts a concentration of VLF energy between ~ 1.9 to ~ 2.5 earth radii over the equator. This

result may be the starting point for future research relative to wave-particle interactions at these equatorial heights.

II. EXCITATION OF WHISTLER-MODE WAVES THROUGH THE LOWER IONOSPHERE

In the lower region of the ionosphere the electron concentration shows substantial variation over distances comparable to the local wavelengths of very-low-frequency waves. The propagation of these VLF waves inside the D-region of the ionosphere is dominated by internal reflections, coupling between different modes of propagation and by collisional absorption. The amplitude of the propagation wave fields does not present a sinusoidal vertical variation, thus ruling out field solutions of the form $\exp(-j\beta z)$. Under the above circumstances a "full-wave" method of solution must be used in which the wave-field solution is constructed point by point inside the ionosphere by solving numerically the related wave equations.

The set of differential equations governing the propagation of plane waves inside a horizontally stratified anisotropic ionosphere was derived by Clemmow and Heading [1954]. These linear differential wave equations are numerically integrated throughout the D and E ionospheric regions by specifying the height distribution of the local ionospheric parameters and the direction and polarization of an incident wave. A computer program for integrating the Clemmow-Heading equations for waves generated below the ionosphere has been developed by Scarabucci [1969]. The numerical technique assumes that there is an electromagnetic plane wave propagating in free space which is incident upon a planarly stratified ionosphere that varies only in the z-direction as shown in Figure 4. The geometry is such that the planes of stratification are parallel to the (x-y) plane. The y axis is parallel to the ground and in the

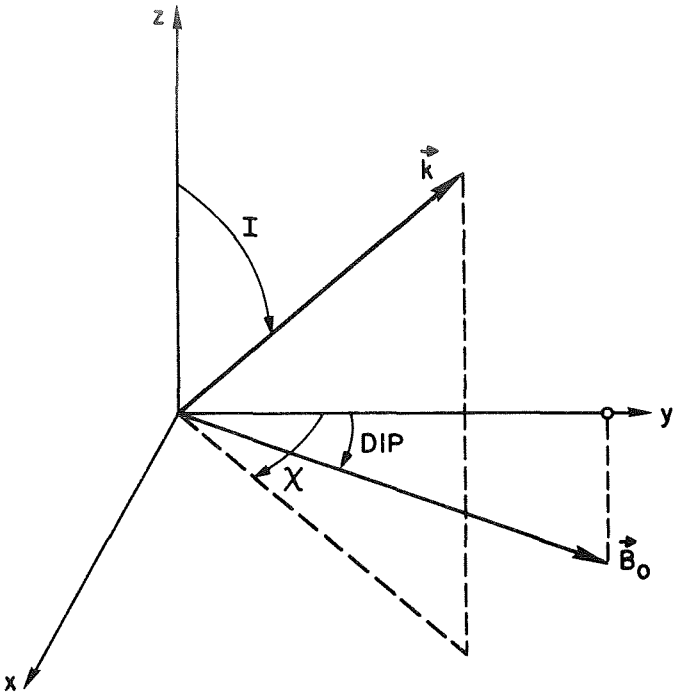

Figure 4. The assumed geometry. Planes of stratification are parallel to the (x-y) plane. DIP is the angle between the geomagnetic field $\vec{B}_o$ and the y-axis. $\vec{B}_o$ lies in the (y-z) plane. I is the angle between the vertical and the wave-normal vector $\vec{k}$. χ is the azimuthal angle for $\vec{k}$.

magnetic meridian (plane y-z) with its positive direction pointing northward. The earth's magnetic field is in the y-z plane making an angle DIP with the y axis. The wave normal of the incident wave makes an angle I with the z axis (angle of incidence) and an angle χ with the magnetic meridian (azimuthal angle).

In this chapter the full-wave computer program of Scarabucci [1969] will be used for studying the excitation of VLF waves through the lower ionosphere. First some properties of the full-wave method of solution

will be discussed. This discussion is followed by a derivation of the equations required for calculating the ionospheric fields generated by ground transmitters by making use of the full-wave method. The equations may be used for predicting the ionospheric fields generated by ground-based VLF transmitters or, similarly, the ionospheric fields originated from naturally occurring lightning flashes. The bursts of current produced by lightning flashes simulate the radiation of a small vertical electric dipole when the discharge occurs between cloud and ground. The process of calculation is then applied for computing the wave fields that should be measured by a polar satellite during its pass in the nearby ionospheric region of a 12.5 kHz transmitter. More specifically the purpose of the calculation is to compare the computed field with measurements made aboard the OGO-4 satellite near the Omega transmitter located in New York. The results are discussed and it is shown that the full-wave method produces field values that match the measurements in a very consistent and stable manner.

A. SOME PROPERTIES OF THE NUMERICAL FULL-WAVE METHOD

Most of the properties presented by the numerical full-wave method have been extensively studied in three brilliant papers by Pitteway [1965], Piggot et al. [1965], and Pitteway and Jespersen [1966]. The purpose here will be to establish some fundamental properties that will be continuously used from now on and to emphasize aspects of the method that have not been covered by the above referenced papers.

The full-wave solution for the problem of incidence of upgoing waves in the lower ionosphere is given in terms of "penetrating" and "non-penetrating" mode waves. Given the direction of the incident wave, the

penetrating mode is found by determining the polarization of the incident wave which maximizes the power transmitted through the lower ionosphere. The non-penetrating mode has polarization such that no power-flow is produced at the top of the ionosphere. Therefore the ability of an incident wave to generate whistler-mode waves inside the ionosphere is directly related to the degree of similarity between the polarizations of the incident wave and that of the penetrating mode.

Figure 5 shows the envelope of the total $Z_o H_x$ field set up by a penetrating mode wave of 18.6 kHz that encounters the D region of the ionosphere at an angle of incidence of 30^o and travels from east to west ($\chi = -90^o$). The field envelope is shown together with some nighttime height distributions of electrons and electron collision frequency (right side of Figure 5) in order to emphasize some relationships between the wave field distribution and the assumed models of electron density and collision frequency. The ionospheric profiles a, b, and c were derived by Deeks [1966a] based on measurements of reflection coefficients made in England and using the full-wave computer program of Pitteway. The nighttime profile b is appropriate for winter at sunspot maximum and also for summer and equinox at sunspot minimum. This profile will be used extensively in this report.

Laboratory experiments (Huxley [1959], Phelps and Pack [1960]) have shown that the collision frequency of electrons with air molecules (nitrogen, oxygen) is directly proportional to electron energy. Using the above relationship for the collision frequency and the theoretical approach of Sen and Wyller [1960] for the susceptibility of a medium having a Maxwellian distribution of electrons, Deeks [1966b] derived new wave equations describing propagation of waves through the ionosphere.

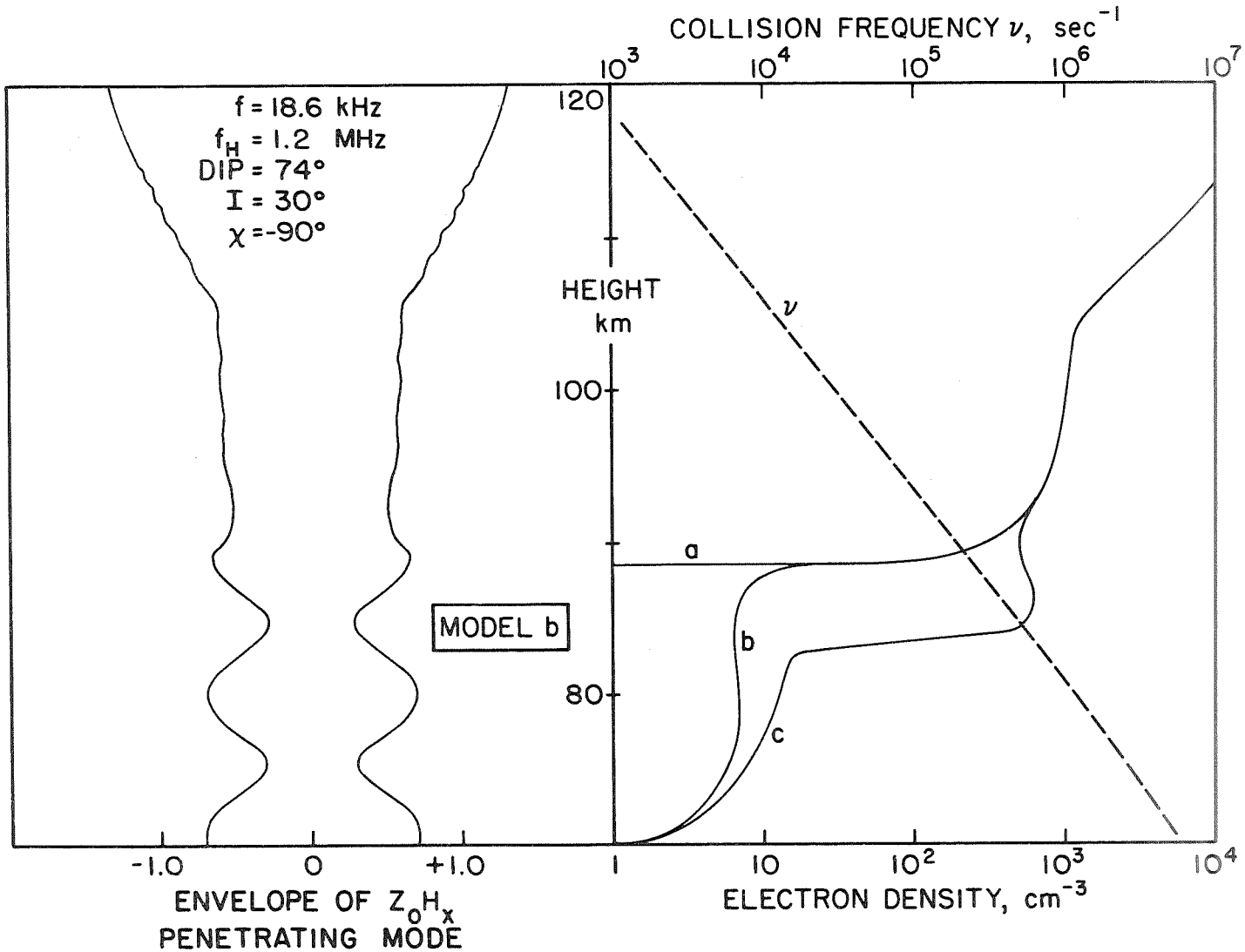

Figure 5. Three ionospheric profiles a,b,c for the nighttime D-region and the effective collision frequency ν are shown on the right side of the figure [Deeks, 1966a,b]. The resulting envelope of $Z_o H_x$ for the penetrating mode whose parameters are shown on the left (top) are given for ionospheric model b. Z_o is the impedance of free space.

He showed that no essential new features were introduced into the results of full-wave calculations by the use of the generalized theory and that a suitable choice of effective classical collision frequency gives numerical results in good agreement with the more complicated theory. The effective classical collision frequency ν in Figure 5 was calculated by Deeks [1966b] based on experimental results and is valid for VLF waves.

For daytime and mid-latitudes appropriate electron density models of the D region were given by Mechtly and Smith [1968]. However, no calculations for daytime at mid-latitudes will be presented in this report.

The envelope of the penetrating $Z_o H_x$ field shown at the left of Figure 5 presents a standing wave pattern below the principal reflection level at $\sim$ 89 km. It shows that the small electron densities provided by model b below 89 km do not substantially interfere with the propagation of the 18.6 kHz waves because the distance separating peaks or valleys in the standing wave is essentially that resulting from propagation in free space. Above 90 km the amount of energy reflected is very small, the "wave length" decreases and although some absorption is occurring at these heights the magnetic wave field increases because of impedance transformation. Some small reflections still occur above 104 km where the electron density exhibits again substantial vertical variation. However the wave length inside the medium becomes smaller and soon the medium is a slowly varying ionosphere for 18.6 kHz waves as denoted by the smooth variation of the envelope of $Z_o H_x$ above 115 km. Therefore an incident penetrating mode wave gives rise to a reflected downgoing wave and to an upgoing whistler-mode wave high in the ionosphere. Although the power carried through by the whistler-mode wave is maximized by the choice of a suitable polarization (penetrating mode) for the

incident wave, it does not necessarily produce the smallest amount of reflected power.

Figure 6 illustrates the behavior of the transmission coefficients in the lower ionosphere for 17.8 kHz waves as a function of the angle of incidence and for propagation along the north-south meridian ($\chi = 0^{o}$). The ionospheric model used is the one labeled b in Figure 5. The earth's magnetic field and the wave frequency are such that Figure 6 simulates nighttime conditions near the VLF Navy transmitter NAA in Cutler, Maine (44.7^{o}N, 67.3^{o}W). The square of the transmission coefficient is defined as the ratio between the z-directed power flow carried by the whistler-mode wave high in the ionosphere and the z-directed power flow of the incident wave (see Scarabucci [1969]). The transmission coefficient characterizes the total loss (reflection plus absorption) suffered by the input wave. Figure 6 shows the transmission coefficient T_p for the penetrating mode and the coefficients T_h and T_v corresponding to horizontal and vertical polarizations. T_h and T_v are related to T_p by

$$T_v^2 + T_h^2 = T_p^2 \qquad (2.1)$$

Figure 6 shows that the transmission coefficients decrease for I approaching the limiting angles of $\pm 90^{o}$ and that they present a broad maximum around $I \cong -15^{o}$ when the incident wave normal is directed along the earth's magnetic field (DIP = 75^{o}). Figure 6 also shows that for the assumed ionospheric conditions the vertical polarization is related to more losses relative to horizontal polarization. However observe that for angles of incidence near -15^{o} we have $T_h \cong T_v$ and $T_p = \sqrt{2}\, T_h$, which means that both vertically and horizontally polarized

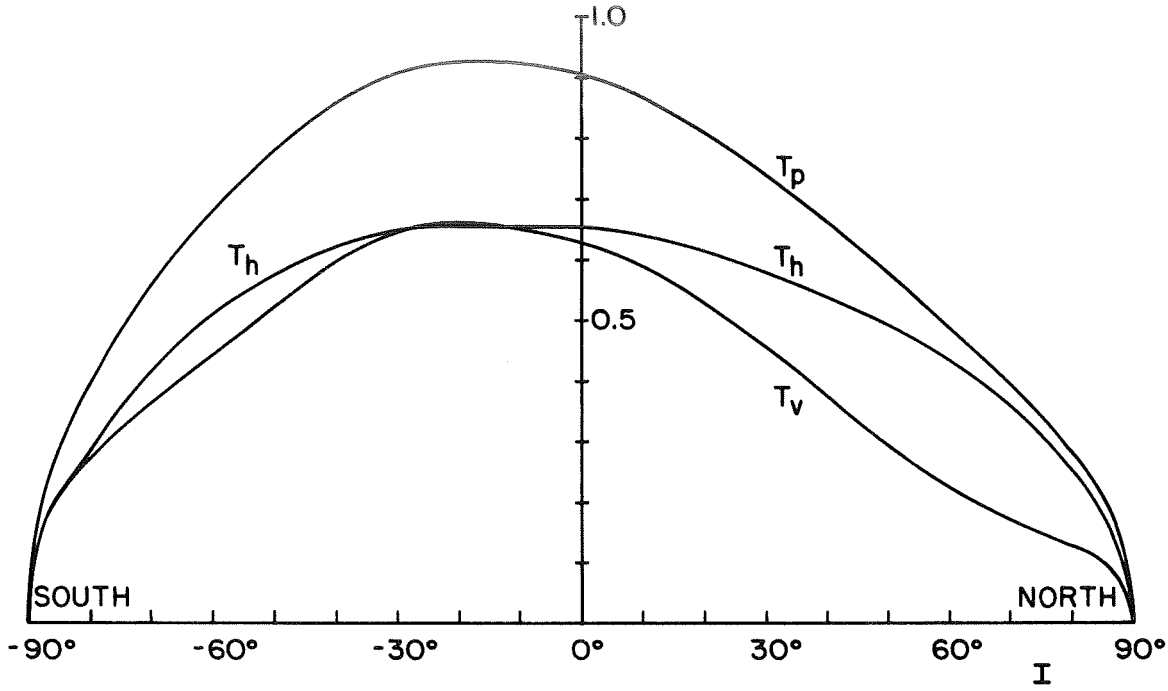

Figure 6. Transmission coefficients for the penetrating mode T_p, vertical polarization T_v and horizontal polarization T_h at 17.8 kHz. DIP = 75^o, f_H = 1.6 MHz and the propagation is along the meridian $\chi = 0^o$. Ionospheric profile b from Figure 5.

waves only lose 3 db relative to the whistler-mode wave set up by the penetrating mode.

Figure 7 shows the polarization ρ_p of the penetrating mode for the same conditions of Figure 6. The polarization is defined here by the ratio between the electric field component in the plane of incidence $E_{P.I.}$, and the horizontal component of the electric field E_{HOR}. Figure 7 shows that the polarization of the penetrating mode is nearly circular to the left near $I = -15^o$ where $|\rho_p|$ is close to 1 and $\underline{|\rho_p}$ is close to -90^o.

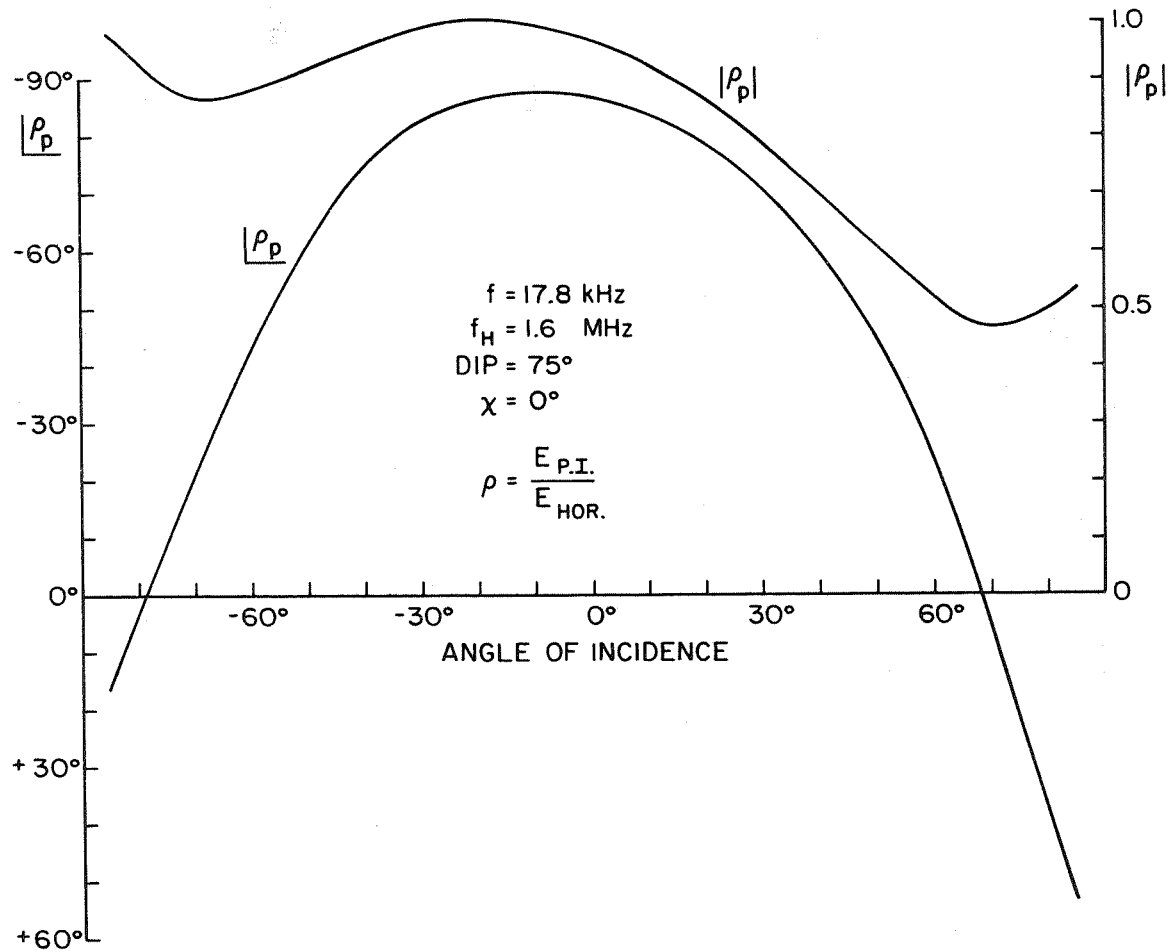

Figure 7. Variation of the polarization ρ_p of the penetrating mode along the meridian.

Figure 7 shows that for most angles of incidence the penetrating mode is elliptically polarized to the left. However when the angle between the incident wave normal and the magnetic field is very large the optimum polarization changes the sense of rotation from left to right after achieving linear polarizations at $I \cong 68.5^{o}$ and $I \cong -79^{o}$. These linear polarizations of the penetrating mode are neither horizontal nor vertical for the ionospheric conditions of Figure 7. For example, at $I = 68.5^{o}$, $\rho_p \cong 0.47$ which means that the penetrating incident electric wave field makes an angle of $\sim 25^{o}$ with the horizontal plane.

B. IONOSPHERIC WAVE FIELDS GENERATED BY GROUND TRANSMITTERS

In this section we derive the equations for calculating the wave fields high in the ionosphere produced by a ground-based small vertical dipole antenna. The adopted geometry is given in Figure 8 where a ray trajectory from the ground transmitter T to a satellite S is shown. The wave radiated by T hits the lower boundary of the D region of the ionosphere whose height is h after traveling a distance s. The wave normal of the incident wave bends toward the vertical during the D region crossing and the ray is finally launched in the whistler medium above the E region of the ionosphere. The point of entry in the lower ionosphere occurs at a ground distance d from the transmitter and the angle of incidence is I as shown in Figure 8. Observe that in addition to the ray shown in Figure 8 other rays may also reach the satellite by bouncing one or more times between the lower edge of the ionosphere and the ground, finally following a trajectory that also intercepts the satellite S. This fact introduces the possibility of fading and will be discussed near the end of this section. The equations to be derived

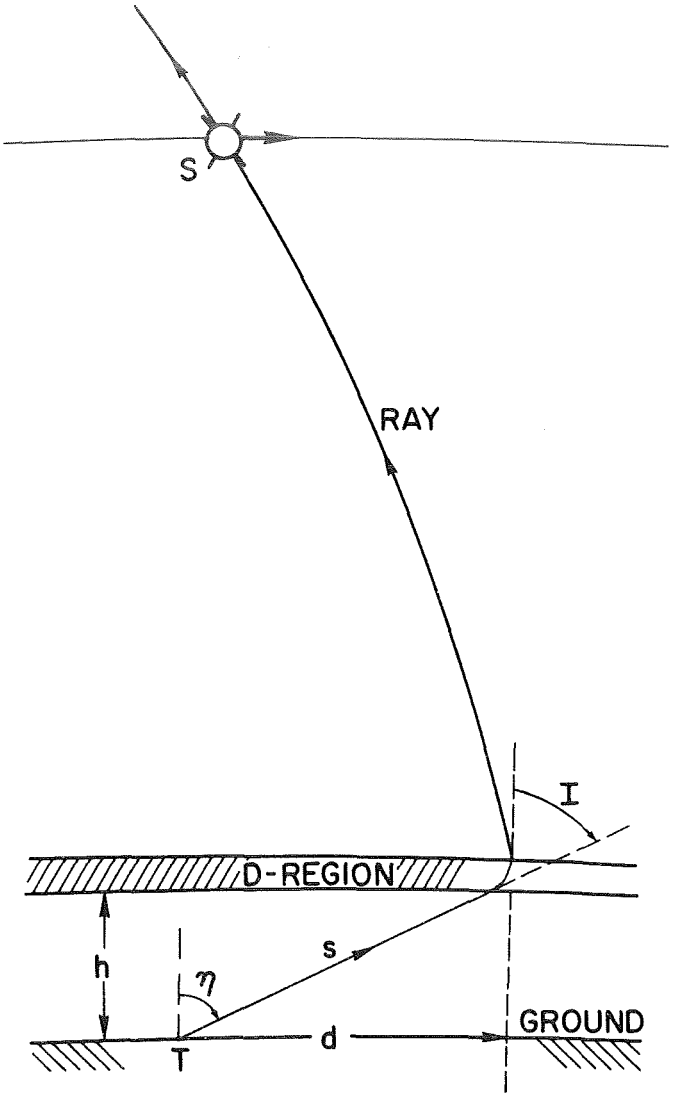

Figure 8. Ray-trajectory between a ground VLF transmitter T and a satellite S.

are valid for distances d inside a circle of radius $\sim$ 1000 km where the polarization of the waves hitting the ionosphere may easily be determined. For distances d larger than 2000 km a better procedure is to discard the ray approach between the transmitter and the point of entry in the ionosphere, and to assume the earth ionosphere waveguide

approach. In order to determine the leakage of the waveguide, further assumptions must be made by assuming only the existence of the waveguide mode $n = 1$ and a transmission coefficient in the lower ionosphere given by the penetrating mode. Obviously the accuracy of the calculation must be relaxed.

Heyborne [1966] calculated ionospheric wave fields using results deduced by Crary [1961] in which a sharply bounded model of the lower ionosphere was assumed. Among other assumptions, Crary assumed a vertical magnetic field and a homogeneous ionosphere. Heyborne assumed some values for the reflection coefficient and that ionospheric loss was represented only by absorption. The polarization and the azimuthal direction of the incident wave were disregarded.

The process of calculation used here differs significantly from the one presented by Heyborne [1966] because of a different mathematical approach followed here which simplifies the analysis. The behavior of the waves in the lower ionosphere is studied by using the full-wave computer program of Scarabucci [1969], while the ray trajectories above the E region are analyzed by means of a ray-tracing computer program developed by Walter [1969].

1. Power Radiated by a Small Vertical Grounded Dipole

The power flux p radiated by a vertical grounded dipole whose length is much smaller than the wave length at the frequency of excitation is purely radial relative to the dipole and is given by

$$p = F \sin^2\eta/s^2 \qquad \text{watt/m}^2 \tag{2.2}$$

where η is the declination angle shown in Figure 8 and F is a constant that depends on the amount of radiated power P. The radiation pattern

of the small grounded dipole at any vertical plane that contains the dipole is a half "eight" figure (see for example Terman [1955] Sec. 23-6) which means that η is defined between 0^{o} and 90^{o}. The radiated power P is found from p by summing up all the fluxes emanating from a closed surface that contains the dipole, for example

$$P = \oint_{\text{sphere}} p\,dS = \int_{o}^{\pi/2} \frac{F \sin^2\eta}{s^2} \cdot (2\pi s \cdot \sin\eta) \cdot s\,d\eta = \frac{4\pi F}{3} \tag{2.3}$$

Therefore, the power-flux, Eq. (2.2) is given by

$$p = \frac{3P\sin^2\eta}{4\pi s^2} \tag{2.4}$$

2. Transmission in the Lower Ionosphere

The z-directed power flux p'_z above the E region is related to p by the transmission coefficient for vertical polarization, i.e.,

$$T_v^2 = \frac{p'_z}{p\cos I} \tag{2.5}$$

Above the E region the W.K.B. method replaces profitably the full-wave method. The assumption of planar stratification for the medium is discarded and a ray-tracing technique is used in order to find the trajectories of the upgoing rays. The ray trajectories may involve more attenuation caused by further absorption above the E region and divergence of rays. On the other hand there may be some gain caused by focusing of rays.

Absorption above the E region is caused mainly by Coulomb collision. Calculations of absorption using a realistic collision

frequency profile and for several electron-density profiles provide 1 to 3 db extra attenuation, depending on the ionization between 120 and 600 km. This extra loss is small and will not be considered in the following calculations.

3. Focusing Gain

Under the above circumstances the power flux that arrives at the satellite is related to the input power above the E region by the ray behavior. The focusing gain is defined by the ratio between the input and the output cross-section areas of a "tube of rays." The tube of rays may be determined by two adjacent rays separated in latitude by $\Delta\phi$, and by a longitudinal increment $\Delta\lambda$. If we suppose that the rays remain in the same magnetic meridian, which is a good assumption for the purpose of power calculation, the focusing gain is then independent of $\Delta\lambda$ and is given by

$$G_F = \left(\frac{r_i}{r_s}\right)^2 \frac{\Delta\phi_i \cos\phi_i \cos\beta_i}{\Delta\phi_s \cos\phi_s \cos\beta_s} \qquad (2.6)$$

where i refers to the position of input above the E region and s to the position of the satellite. Figure 9 shows the geometrical parameters involved in Eq. (2.6):

r is the geocentric radius

ϕ is the magnetic latitude

and β is the angle between the ray and the local vertical.

All elements in Eq. (2.6) are determined by the ray-tracing computer program. The focusing gain defined by Eq. (2.6) may assume values above or below the unity which means that divergence of rays is also considered in Eq. (2.6).

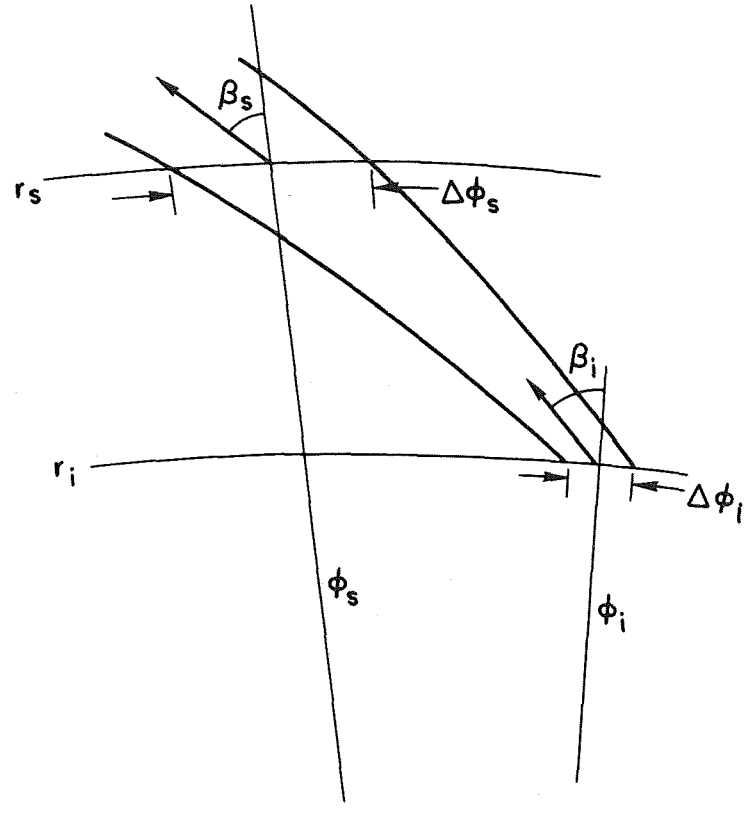

Figure 9. Tube of rays and geometrical parameters for determining the focusing gain.

The power flux p'' at the satellite is related to the power-flux just above the E region by

$$\frac{p''}{p'_z/\cos\beta_i} = G_F \tag{2.7}$$

Observe that p'_z is the vertical component of the total power flux $p'_z/\cos\beta_i$ just above the E region.

Equations (2.5) and (2.4) are substituted in Eq. (2.7) to give

$$p'' = \frac{3PG_F T_v^2}{4\pi s^2} \cdot \frac{\cos I \sin^2 \eta}{\cos \beta_i} \tag{2.8}$$

In Eq. (2.8) s is the distance from the transmitter to the lower edge of the ionosphere as shown in Figure 8.

4. The Magnetic Wave Field at the Satellite

Brice [1964] showed that under the Q.L. approximation the magnetic field of the wave is related to the average power flux by

$$p'' = \frac{Z_o H^2}{\mu_s} \tag{2.9}$$

where H is the amplitude of the magnetic field and μ_s is the longitudinal refractive index at the satellite height. Equation (2.9) is independent of the wave normal direction, an approximation that is good unless the angle between the wave-normal and the magnetic field is close to the resonance cone [Brice, 1964]. Replacing p'' from Eq. (2.9) in Eq. (2.8) we obtain

$$H = \left(\frac{3\mu_s PG_F \cos I}{4\pi Z_o \cos \beta_i} \right)^{1/2} \cdot \frac{T_v \sin \eta}{s} \tag{2.10}$$

If in Eq. (2.10) we express P in kilowatt and s in kilometer and recall that $Z_o \cong 120\pi$ ohms we have

$$H = \left(\frac{\mu_s G_F P \cos I}{\cos \beta_i} \right)^{1/2} \cdot \frac{T_v \sin \eta}{s} \cdot \frac{1}{4\pi \times 10^2} \quad \text{Amp/m} \tag{2.11}$$

Finally we express H in gammas (γ):

$$H \text{ Amp/m} = 4\pi\times10^{2}\ H\ \gamma \tag{2.12}$$

Therefore, the field at the satellite will be given by

$$H = \left(\frac{\mu_s G_F P \cos I}{\cos\beta_i}\right)^{1/2} \cdot \frac{T_v \sin\eta}{s} \qquad \gamma \tag{2.13}$$

P in kilowatt

s in kilometer

In order to use Eq. (2.13) to calculate the magnetic wave field at the satellite the following procedure is used.

1. Ray trajectories in a model ionosphere determine the focusing gain G_F and the longitudinal refractive index μ_s at the satellite height as a function of satellite position. In particular, given a point S high in the ionosphere the ray-tracing technique determines the latitude and the longitude where the ray begins just above the E region.

2. The distance d is then calculated (see Figure 8). Observe that in general the ray trajectory above the E region is not coplanar with the trajectory below the ionosphere.

3. The distance s, the angle of incidence I and the declination angle η are then determined by

$$s = \left\{h^2 + 2r_o(r_o+h)[1-\cos(d/r_o)]\right\}^{1/2} \tag{2.14}$$

$$\tan I = \frac{\sin(d/r_o)}{(h/r_o) + 1 - \cos(d/r_o)} \tag{2.15}$$

and

$$\eta = I + d/r_o \tag{2.16}$$

r_o is the earth radius.

I and η are shown in Figure 10 as a function of the distance d from transmitter and for $h = 90$ km.

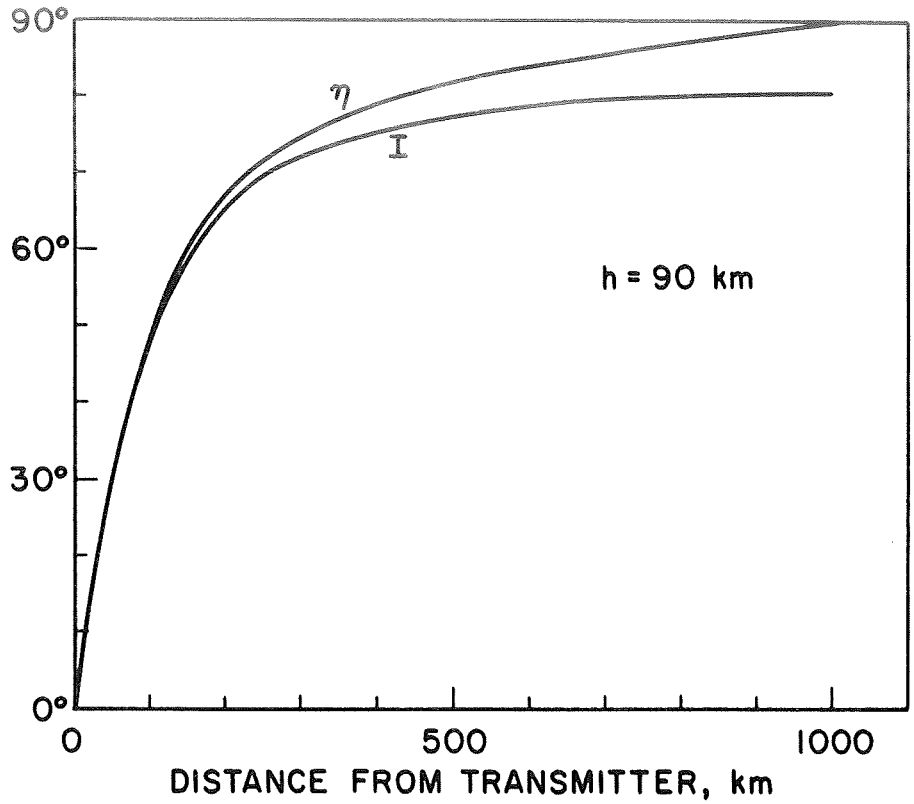

Figure 10. Variation of angles I and η as functions of the distance d for an ionosphere whose height is 90 km.

4. Given I and the azimuth χ of the ray direction below the ionosphere is then possible to determine T_v.

5. Equation (2.13) determines the amplitude of the magnetic wave field at S.

Finally we discuss briefly the possibility of fading caused by interference between the direct ray (the one calculated by Eq. (2.13)) and other rays. These interfering rays may bounce two or more times between the ground and the lower edge of the ionosphere before following a trajectory that also intercepts the direct ray at S. The calculation of the ionospheric fields under these circumstances is somewhat involved because the phase of the wave must be computed in all steps of calculation.

Furthermore the transmission coefficient can be greatly modified after each ground-ionosphere hop because the polarization of the reflected waves is used as input for the succeeding incidence in the ionosphere. Extensive calculations of fading have been done for profile b of Figure 5 and for propagation of 12.5 kHz waves along the meridian at mid latitudes. The results indicate a spatial pattern of fading, presenting a maximum of $\sim$ 5 db between the peaks and valleys of the signal. However the fading usually observed aboard the OGO-4 satellite is much deeper than 5 db which shows that the above kind of fading is not the dominant factor controlling the total field strength.

There are several other effects that can produce deep fading at the satellite. One of these effects, likely to occur in the actual ionosphere, is interference between direct rays that enter the ionosphere at different points and that follow ray trajectories that intersect at the satellite height. Such intersections would be caused by horizontal gradients of electron density. The analysis of deep fading in the amplitudes of ionospheric wave fields will be pursued further in Chapter 6.

C. OGO-4 AMPLITUDE MEASUREMENTS OF WAVE FIELDS IN THE VICINITY OF GROUND TRANSMITTERS

In this section we present typical nighttime amplitude measurements of signals recorded aboard the OGO-4 satellite in the vicinity of ground VLF transmitters. The theory developed in the previous sections is now applied in order to predict the signal levels that should be measured in a specific case. Calculated and measured wave fields are compared and good agreement is obtained.

Figure 11 presents OGO-4 records showing amplitude measurements of signals transmitted by NAA at 17.8 kHz and Omega (New York) at 12.5 to

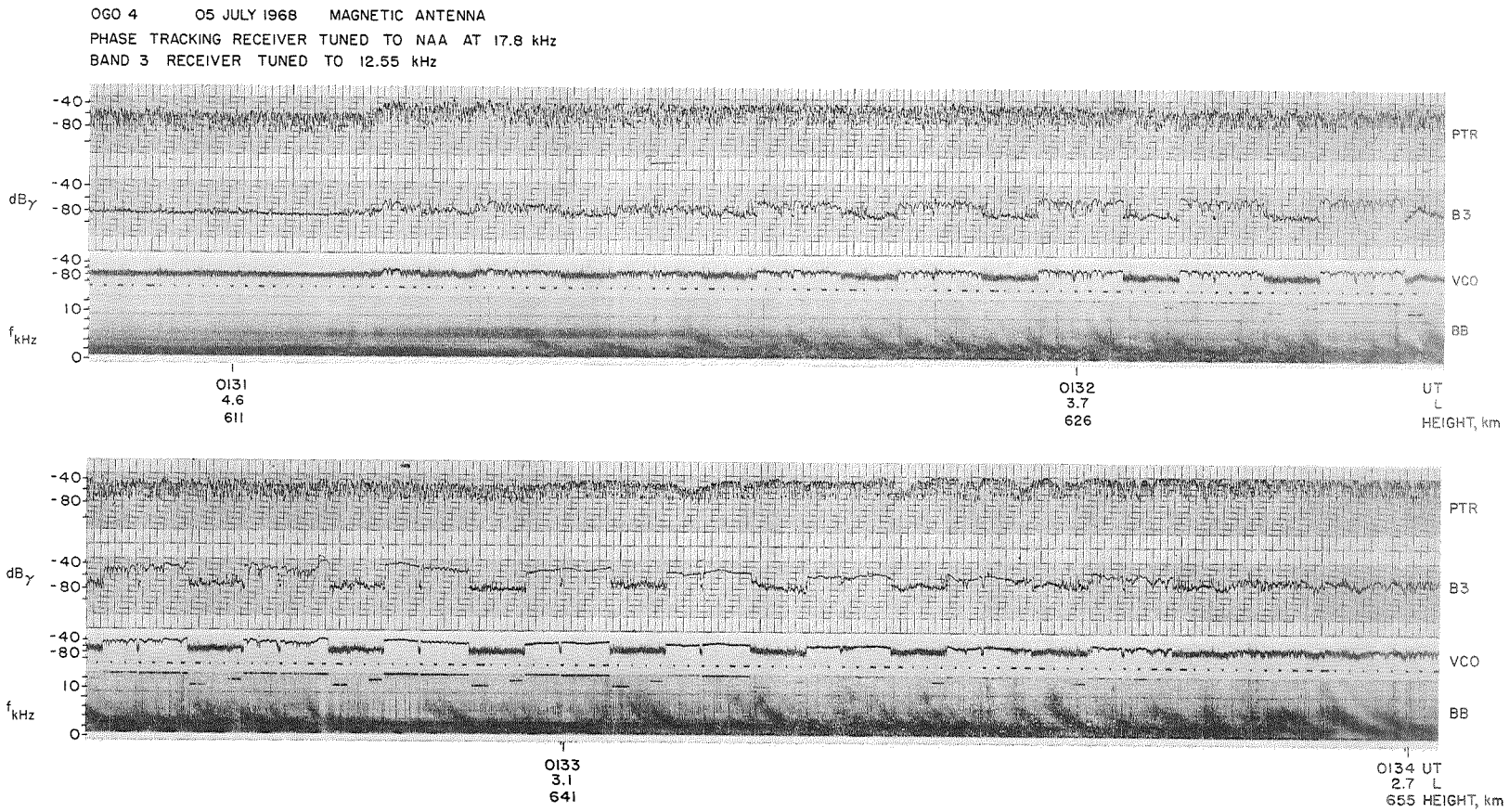

Figure 11. Combination of PCM and analog data from OGO 4. From top to bottom: magnetic field - of NAA (PTR); magnetic field of 12.5 - 12.6 kHz Omega signals (B3); the same as in B3 measured by the VCO; time marks; broadband spectrum from 300 Hz to 12.5 kHz (BB).

12.6 kHz as well as broadband spectrum information for wave frequencies between 300 Hz to 12.5 kHz. Each panel of Figure 11 includes about 1.5 minutes of data and the measurements are presented as functions of time (0131 UT to 0134 UT), L value and height of the satellite. In each panel there are 5 independent records, namely from top to bottom:

1. magnetic field of 17.8 kHz waves measured by the phase-tracking receiver (PTR);
2. magnetic field of 12.5 to 12.6 kHz waves measured by the stepping receiver No. 3 (B3);
3. same as in B3 but telemetered to ground via VCO;
4. time marks at one second intervals;
5. broadband spectrum from 300 Hz to 12.5 kHz (BB).

The magnetic field amplitudes are given in db relative to 1 gamma (db_γ). Several aspects of the data displayed in Figure 11 will be analyzed in Chapter 6. Here we concentrate on the amplitude features presented by the stepping receiver No. 3 relative to signals transmitted by the Omega station of Forest Port, New York. The schedule of Omega (New York) was composed of transmission segments at 10.2, 11.33, 12.5, 12.6 and 13.6 kHz. With the exception of the 13.6 kHz segment, lying outside the pass band, the transmission segments are observed by the broadband spectrum receiver (bottom record of each panel). The transmission segments detected by the stepping receiver No. 3 correspond to 12.5 kHz radiated in the interval [0, 3.4] sec and 12.6 kHz in the interval [7.4, 9.8] sec inside each 10 second interval (see Figure 11).

Figure 12 shows the satellite trajectory and the locations of the Omega (New York) and NAA transmitters in respect to geographic coordinates. Also shown is a magnetic meridian plane that crosses the satellite trajectory near the Omega transmitter in order to illustrate schematically how a signal radiated from the transmitter reaches the satellite at S.

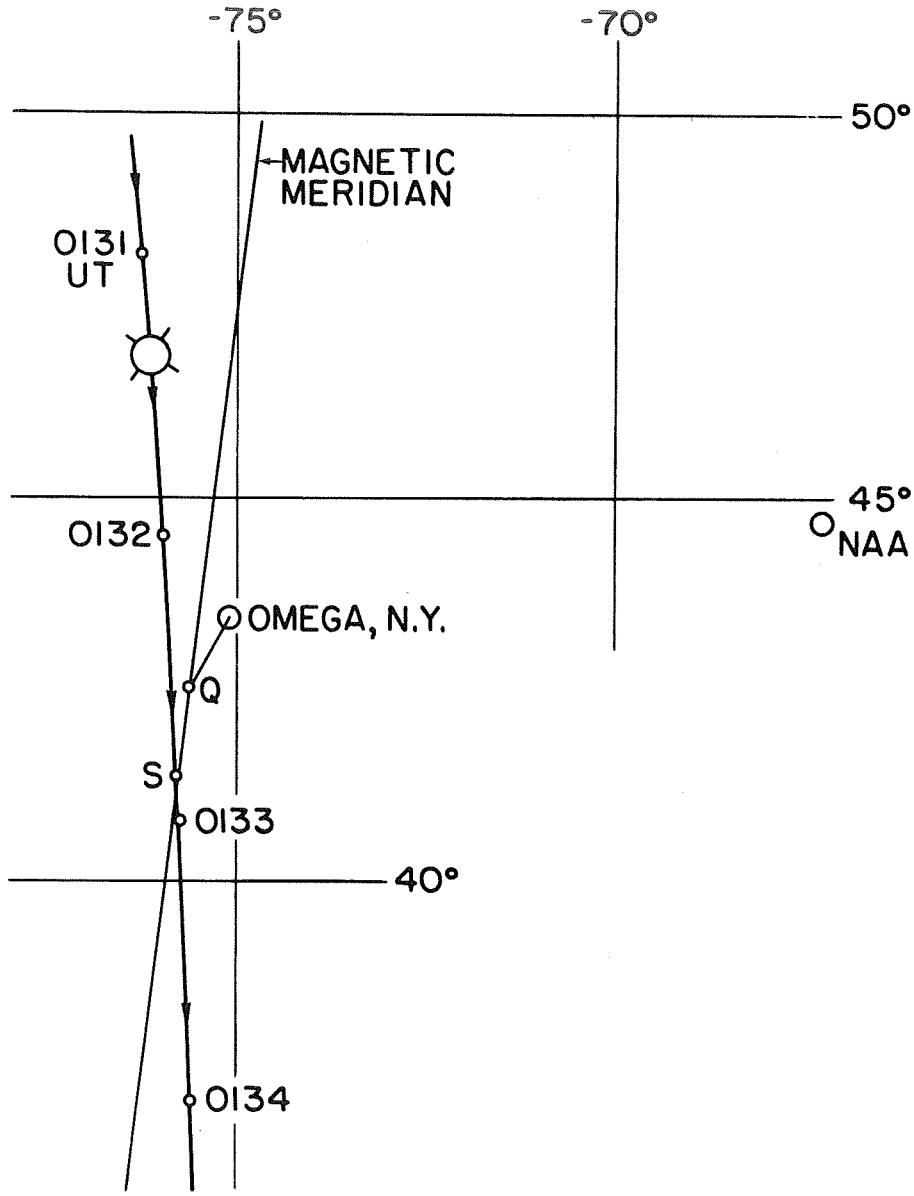

Figure 12. OGO-4 trajectory for the records of Figure 11.

The wave travels below the ionosphere to the entry point Q in the lower edge of the D region, is launched in the whistler medium above the E region and finally follows a ray path nearly along the magnetic meridian to the satellite.

In order to calculate the fields at the satellite by using Eq. (2.13) we start with the ray trajectories of 12.5 kHz waves in a model magnetosphere. The model used here includes latitudinal variation of electron density and is the same model employed in Chapter 5 where it is used for the purpose of studying general characteristics of the ray trajectories in the magnetosphere. The details of the assumed model are given in Section D of Chapter 4. Figure 13 shows the receiving latitudes of rays for a satellite at 640 km altitude as a function of the input latitudes, where the rays start at 120 km. Also shown is the longitudinal refractive index at 640 km for the assumed magnetospheric model. Once Figure 13 is determined by the ray-tracing computer program, we introduce the magnetic latitudes of the satellite for the pass of Figure 11 by means of time marks. Using Figure 13 and the angles β_s from the ray-tracing computer program, we determine the ratio $G_F/\cos\beta_i$ which is independent of β_i as shown in Eq. (2.6). This ratio varies from 1.02 to 0.92 when the magnetic latitude of the satellite changes from 60^o to 50^o for the model magnetosphere.

Another important use of Figure 13 is to determine the entry point Q (see Figure 12) at 120 km for each satellite position. This is shown in Table 1 where the geographic latitudes and longitudes of the entry points are given in the second and third columns as functions of time. With the locations of the entry points we determine the distance d by using a standard equation of spherical triangles. Distances s are then

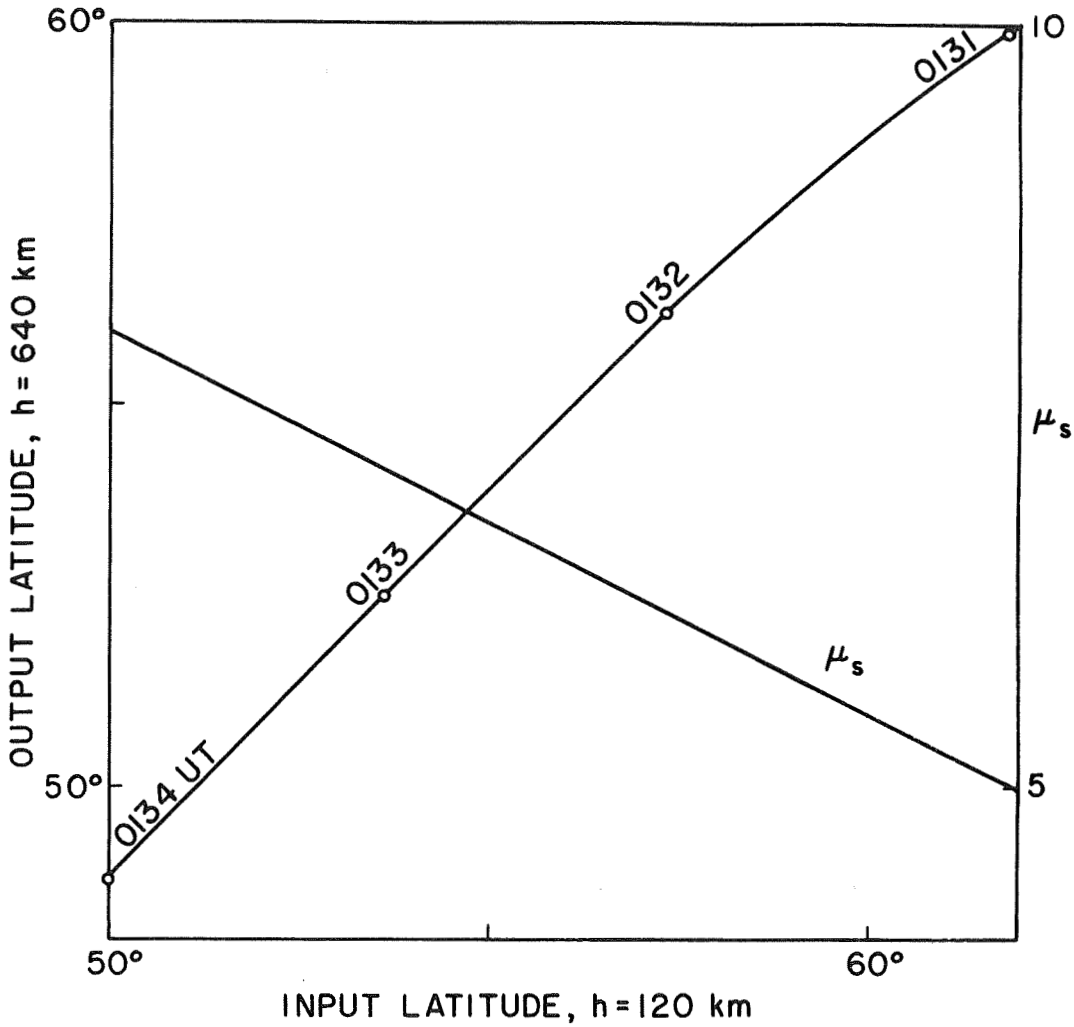

Figure 13. Receiving latitudes of rays and the corresponding longitudinal refractive index μ_s for waves of 12.5 kHz as a function of the input latitude. The ionospheric model is given in Chapter 4, Section D.

TABLE 1.

TIME	ENTRY Q		d	s	I	η	χ	T_v	FULL-WAVE		RAY-ABSORPTION	
UT	LAT	LONG	km	km					H, $10^{-3}\gamma$	H, dBγ	H, $10^{-3}\gamma$	H, dBγ
131.0	50.0	-76.0	727	737	80	86	-15	0.21	0.149	-76.6	0.665	-63.6
131.5	47.6	-76.0	461	473	77	81	-18	0.23	0.282	-71.0	1.15	-59.0
132.0	45.6	-75.8	239	257	68	71	-24	0.30	0.820	-61.7	2.56	-52.0
132.5	43.8	-75.8	75	118	40	40	-70	0.59	3.70	-48.6	5.90	-44.6
133.0	41.9	-75.6	183	205	-63	65	+9	0.48	1.93	-54.3	3.77	-48.5
133.5	40.1	-75.5	378	391	-75	78	0	0.41	0.730	-63.0	1.67	-55.6
134.0	38.4	-75.4	565	576	-79	84	-4	0.38	0.420	-67.6	1.04	-60.0

calculated by Eq. (2.14) and angles I and η are taken from Figure 10. Values for d, s, I, and η are shown in Table 1. The knowledge of all pertinent geometrical factors affecting the propagation is completed by determining the azimuthal angles χ at the points of entry in the lower ionosphere. χ is added to Table 1.

The next step is to find the nighttime transmission coefficients in the lower ionosphere suitable for the region of New York. The ionospheric profile b from Figure 5 is used together with a gyrofrequency of 1.6 MHz and magnetic field dip of 75^{o} as input to the full-wave computer program. The resulting transmission coefficients are shown in Figure 14a for north-south propagation ($\chi = 0^{o}$) and Figure 14b for east-west propagation ($\chi = -90^{o}$). Among other features, Figures 14a and 14b show that vertically polarized waves have greater transmission coefficients relative to horizontally polarized waves when propagating westward and southward.

For the values of χ shown in Table 1, the transmission coefficients for vertical polarization are found by interpolating T_{v} between Figures 14a and 14b, shown in Table 1.

The powers radiated by the Omega transmitter of Forest Port, New York during the period 0129 to 0135 UT on 5 July 1968 were 278 watts at 12.5 kHz and 295 watts at 12.6 kHz (information provided by M. L. Tibbals). In the following calculation a radiated power of 285 watts has been assumed. Now all the factors affecting Eq. (2.13) are known and the value of the magnetic field at the satellite can be estimated. This is shown in Table 1 and plotted in Figure 15. Figure 15 shows the predicted "full-wave" magnetic field amplitudes in db relative to one gamma (continuous curve) as a function of time. In addition Figure 15 shows the amplitude measurements of Omega signals displayed in Figure 11 and also the magnetic

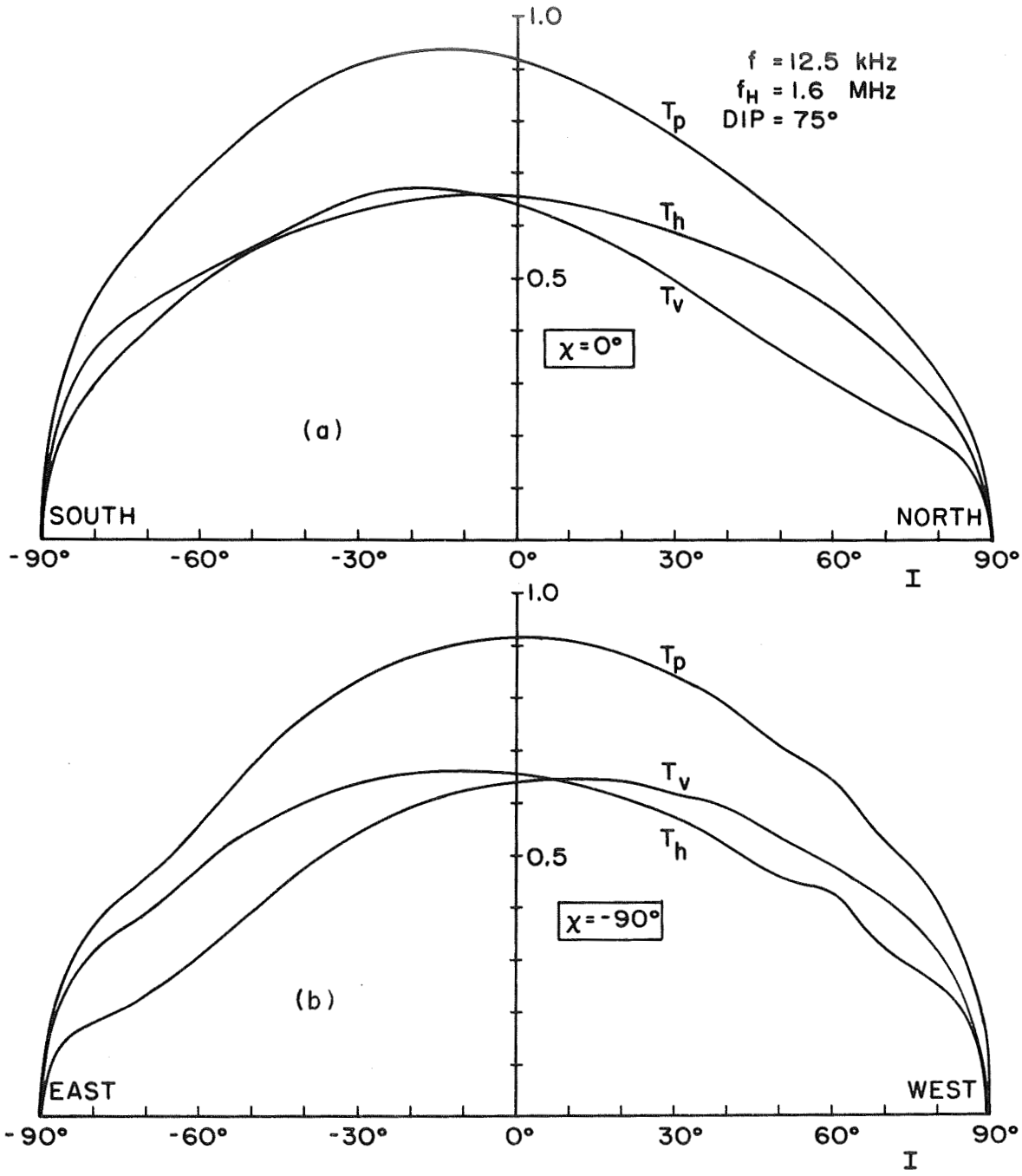

Figure 14. (a) Transmission coefficients at 12.5 kHz along the meridian, $\chi = 0^{o}$. (b) Transmission coefficients at 12.5 kHz in the east-west azimuth, $\chi = -90^{o}$.

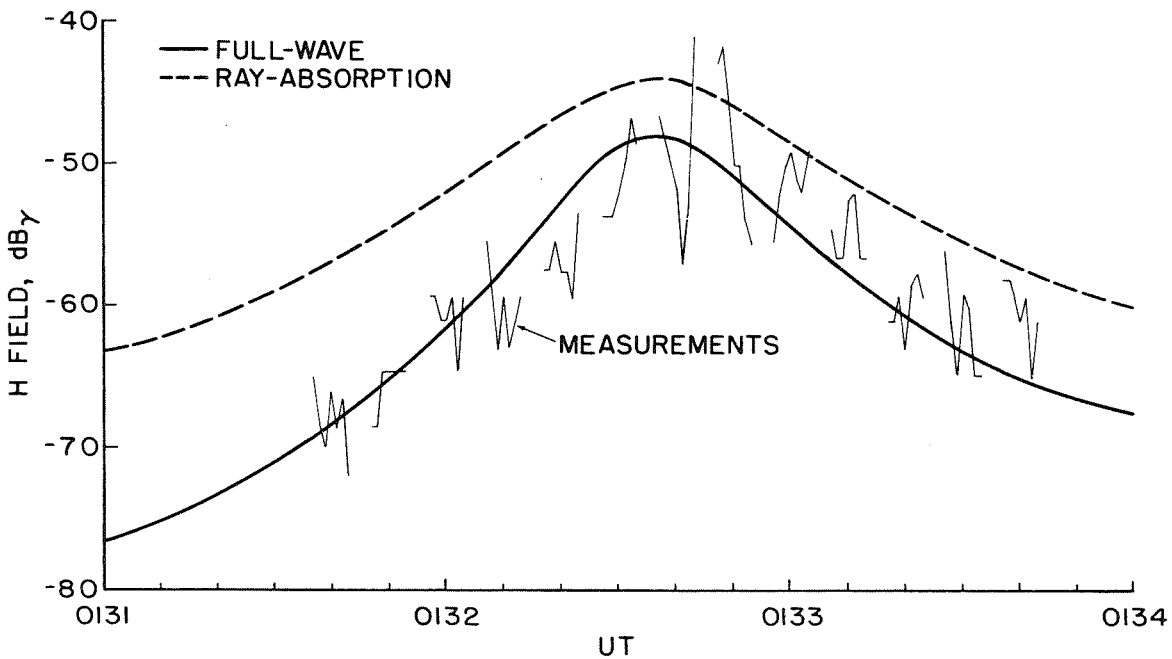

Figure 15. Comparison between calculated and OGO-4 observations of magnetic field amplitude of 12.5 - 12.6 kHz signals transmitted by Omega - New York between 0131 and 0134 UT on 5 July 1968.

field values that would be predicted using a ray-absorption method (dashed curve). The measurements are represented in Figure 15 by broken lines where the corresponding amplitude values at each integer second are the average values of the field measured by OGO 4 during one second.

The field values predicted by the ray-absorption method are also shown in Table 1. They were calculated by integrating the imaginary part of the refractive index through the same ionospheric profile b of Figure 5 and hence finding the total absorption. The resulting transmission coefficient has a constant value of 0.937. The fields were then calculated with Eq. (2.13), replacing T_v by a constant value of 0.937.

Figure 15 shows that the wave fields predicted with the full-wave method agree very well with the average measurements made on OGO 4. The reason for the success of the full-wave method is that this process takes into account all the important factors that control the losses in the lower ionosphere, namely polarization of the wave, reflection and absorption. On the contrary the ray-absorption method only takes into account the absorption of the wave. Therefore the shape of the related curve displayed in Figure 15 is almost exclusively controlled by the variation of the distance s (see Eq. (2.13)). As a consequence the predicted field amplitude varies as $\sim 1/s$ at great distances from the transmitter which is inadequate as shown in Figure 15.

Observe finally that the values supplied by the ray-absorption method are in better agreement with the measurements south of the transmitter (after $\sim$ 0133 UT). This happens because the transmission coefficient for vertically polarized waves is only about 3 db below the coefficient for the penetrating mode wave when propagation is southward as shown in Figure 14a. However, the transmission coefficient for

vertically polarized waves traveling northward is smaller (Figure 14a). Therefore the values predicted by the ray-absorption method in this case lie well above the field measurements recorded by OGO 4 north of the transmitter as shown in Figure 15 between 0131 and 0132:30 UT.

III. OGO-4 OBSERVATIONS OF EQUATORIAL ABSORPTION AND DEFOCUSING OF VLF ELECTROMAGNETIC WAVES

A. INTRODUCTION

In this chapter two new ionospheric phenomena involving the propagation and absorption of VLF waves near the magnetic equator are presented and discussed. Both phenomena are related to attenuation of VLF signals received aboard a polar orbiting satellite when the spacecraft travels at low latitudes. One effect, called "equatorial erosion," occurs on the dayside and involves frequency-dependent attenuation, with all VLF signals from ground sources eventually disappearing below the level of detectability as the satellite approaches the equator. An example of equatorial erosion observed from OGO 4 is shown in Figure 16, which displays frequency from 0 to 10 kHz versus magnetic latitude and time on a northbound pass. As the satellite moves toward the equator between 2049 and 2050 UT, broadband VLF whistler signals are 'eroded,' cutting off at successively lower frequencies with decreasing latitude. The activity recovers north of the equator, but in somewhat irregular fashion.

The other new phenomenon, interpreted here as "equatorial defocusing," is observed in the nighttime ionosphere and involves abrupt decreases in the intensity of manmade VLF signals, typically more than 15 db in less than 50 km. Two examples of equatorial defocusing are shown by the OGO-4 records of Figure 17. The two panels show for two consecutive nighttime equatorial passes the amplitude of the magnetic field of signals transmitted by NAA (17.8 kHz) and received aboard the satellite by the phase tracking receiver. The records show NAA signal levels of about -80 to -90 dbγ when the satellite is at geographic latitudes of about -25^{o} and as the satellite moves northward a pronounced drop in signal intensity

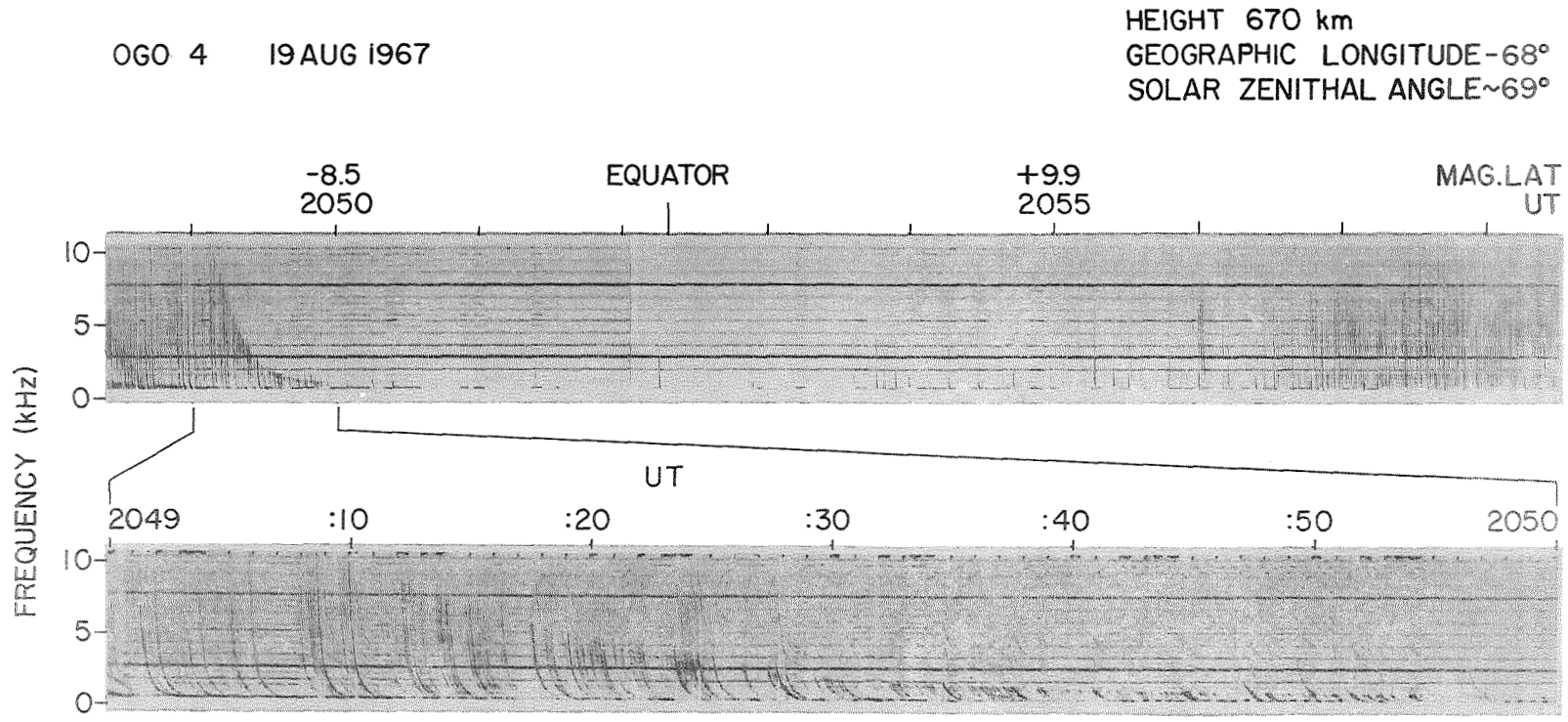

Figure 16. Frequency-time spectra of broadband VLF data from OGO 4 showing a typical example of daytime "equatorial erosion." The bottom panel shows a portion of the upper record in expanded time scale where downgoing whistlers entering the ionosphere in the conjugate hemisphere exhibit a latitude-dependent upper cutoff. The horizontal lines are caused by interference from the odd harmonics of the spacecraft dc converters at 2461 kHz (heavy lines) and even harmonics from the 400 Hz power supply line (weak lines) which show up when the external signal level is very low.

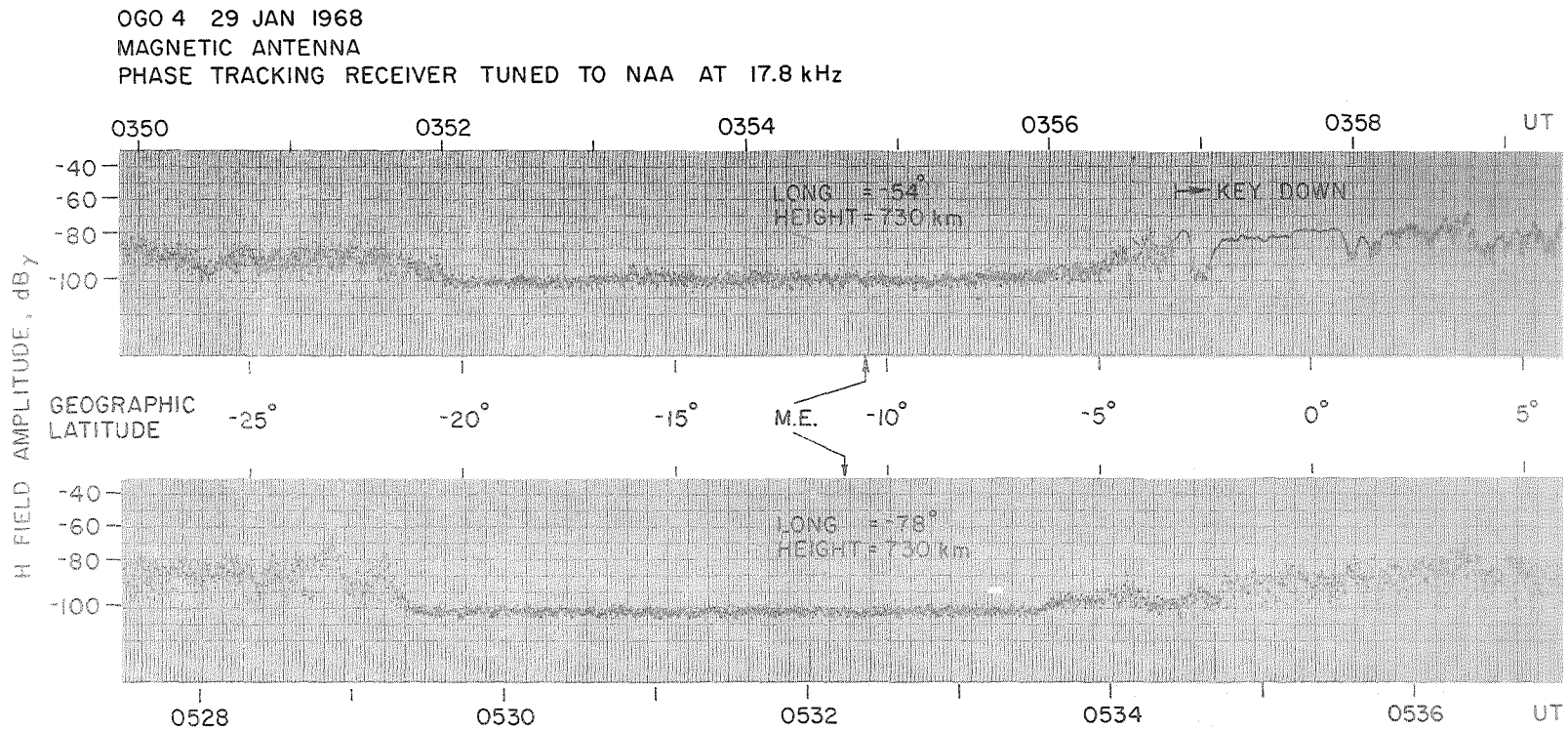

Figure 17. OGO-4 records showing the NAA magnetic field amplitude as measured by the satellite phase-tracking receiver in two consecutive equatorial crossings. The records present the nighttime "equatorial defocusing" with the amplitude of the signal dropping below equipment threshold at about -100 dbγ. The relative position of the magnetic equator is indicated by M.E. At about 0357 UT the pattern of NAA signal changes to Key-down mode, preceding the major change from CW (0300-0400 UT) to FSK (0400-0500 UT) in the mode of transmission.

occurs at the vicinity of -20^{o} with the field strength dropping below the noise level of about -100 dbγ. The signal remains below the noise level in the succeeding 15^{o} of northward satellite flight and emerges from the noise at a geographic latitude of about -5^{o}.

Very-low-frequency waves were first observed in the magnetosphere in 1961 by the Lofti-I satellite [Leiphart et al., 1962]. In this experiment VLF signals were received from U.S. Navy stations NBA in the Canal Zone and NPG in Jim Creek, Washington. Interpreting these measurements, Rorden et al. [1964] reported a higher attenuation in the signals from NBA, and suggested that the difference could be attributed to a greater absorption at low latitudes. A more systematic observation of this kind was reported by Heyborne [1966] who studied the continuous reception aboard the OGO-2 satellite of VLF signals from NPG and NAA. The records showed a consistent drop of the VLF wave fields at each satellite pass over the equator. It was shown that this effect could be attributed to higher ionospheric absorption around the equator.

Better observations of equatorial phenomena have been obtained from the stabilized satellite OGO 4 which provides repeatability of measurements and more confidence in data analysis. Data interpretation has been aided by a new approach involving a full-wave study of the transmission coefficient in the lower ionosphere and a ray-tracing technique to determine effects such as defocusing of the power flow. This approach has led to a satisfactory interpretation of the data, in which the roles of absorption and defocusing in the day and night regimes have been separately identified.

The present work will show that the equatorial erosion is caused by the combined effect of high absorption in the D region at low latitudes

plus the ray trajectories followed by the signals above the F region. At night the absorption effect is less important, with low-altitude equatorial propagation being dominated by a pronounced ionospheric defocusing caused by a rapid increase of the electron-density scale-height above about 500 km. It will be shown that the defocusing phenomenon represents a method of detecting large variations in the vertical gradient of electron density. Therefore, this effect may be used for measuring the nighttime $[O^+ - H^+]$ transition height at the equator.

B. THE EQUATORIAL EROSION

The equatorial erosion effect is manifested in every one of about 200 OGO-4 records of equatorial crossings obtained in daytime during 1967 and 1968. Frequency-time records such as those of Figure 16 typically show that as the satellite approaches the equator the highest frequencies disappear first. Although Figure 16 is typical with respect to the sharpness of the cutoff south of the equator, it shows an unusually smooth variation as compared with most records. Sometimes the erosion is not complete, and the lowest whistler frequencies are observed throughout the equatorial crossing. The erosion effect is also consistently observed at the output of the stepping receivers when these receivers are working in the sweeping mode. It is then usually observed as a disappearance of all ground-source VLF signals from 0.13 to 100 kHz, as shown in Figure 2 near 0139 UT.

1. Qualitative Explanation of the Observations

The equatorial erosion may be understood in terms of an increase in the transmission loss through the ionosphere with decreasing magnetic latitude. In daytime all VLF waves propagate upward with nearly vertical

wave normals, a consequence of applying Snell's law to the lower stratified layers of the ionosphere. Hence, in the region of high VLF absorption (70 to 80 km), the angle between the wave normals and the earth's magnetic field increases as the satellite approaches the equator. The medium becomes optically thicker which means that the wave numbers inside the medium increases, and therefore the wave experiences greater collisional absorption. Thus for a collision-frequency constant in latitude, the absorption should become greater at lower latitudes.

Above 100 km and except under conditions of strong sporadic-E ionization, the ionosphere is a slowly varying medium for all VLF waves, and geometrical optics may be applied in order to determine the path followed by a wave packet. The ray trajectories are not symmetrical around the equator which, as will be seen, accounts partially for the non-symmetrical properties of the erosion effects displayed in Figure 16. In fact daytime propagation around the magnetic equator is influenced primarily by the high vertical gradient of electron density above the F-region, and to a lesser (but nevertheless important) extent by the nearly flat profile of ionization around the bulge of the F region and the curvature of the earth's magnetic field. The high vertical gradient extends to heights above 1000 km for daytime conditions, and is a consequence of a scale-height dominated by oxygen and helium ions. For the range of latitudes where erosion is observed, it has been found that the ray trajectories are curves that cross the equator below 1000 km. Hence the effects of equatorial erosion are observable only by satellites operating below $\sim$ 1000 km at low latitudes.

2. Details of the Analysis

The equatorial erosion phenomenon can be predicted by a study

of D-region absorption, followed by a study of ray trajectories to determine the region of space where the effect should be observed at the satellite.

The ionospheric model used included the electron collision frequency and density profiles for the daytime D region of Piggott et al. [1965], shown in Figure 18. For heights above 100 km an analytical electron-density profile was developed satisfying measurements made by Alouette II in August 1967 (data provided by L. Colin). This profile of ionization is shown in Figure 19 together with Alouette measurements.

The wave equations governing reflection and transmission in the lower ionosphere were numerically integrated by means of a "full-wave" computer program [Scarabucci, 1969]. The main interest here was to determine the transmission coefficient in the lower ionosphere as a function of the magnetic latitude. At each magnetic latitude the direction of the incident wave was chosen so as to give maximum transmission. The polarization at each latitude was selected to be the polarization of the "penetrating mode." Under the above condition the total loss (reflection plus absorption) in the lower ionosphere is given by

$$L = 20 \log_{10} T_p \text{ db} \qquad (3.1)$$

where T_p is the transmission coefficient for the penetrating mode defined in Section A of Chapter 2. Equation (3.1) represents the minimum loss, since L is calculated for the angle of incidence that gives maximum T_p. The computer calculation was programmed to stop at 120 km, where the collision frequency is small and where the W.K.B. method can replace the "full-wave" method. The remaining E-F region absorption is small compared with the D-region absorption, and has been neglected.

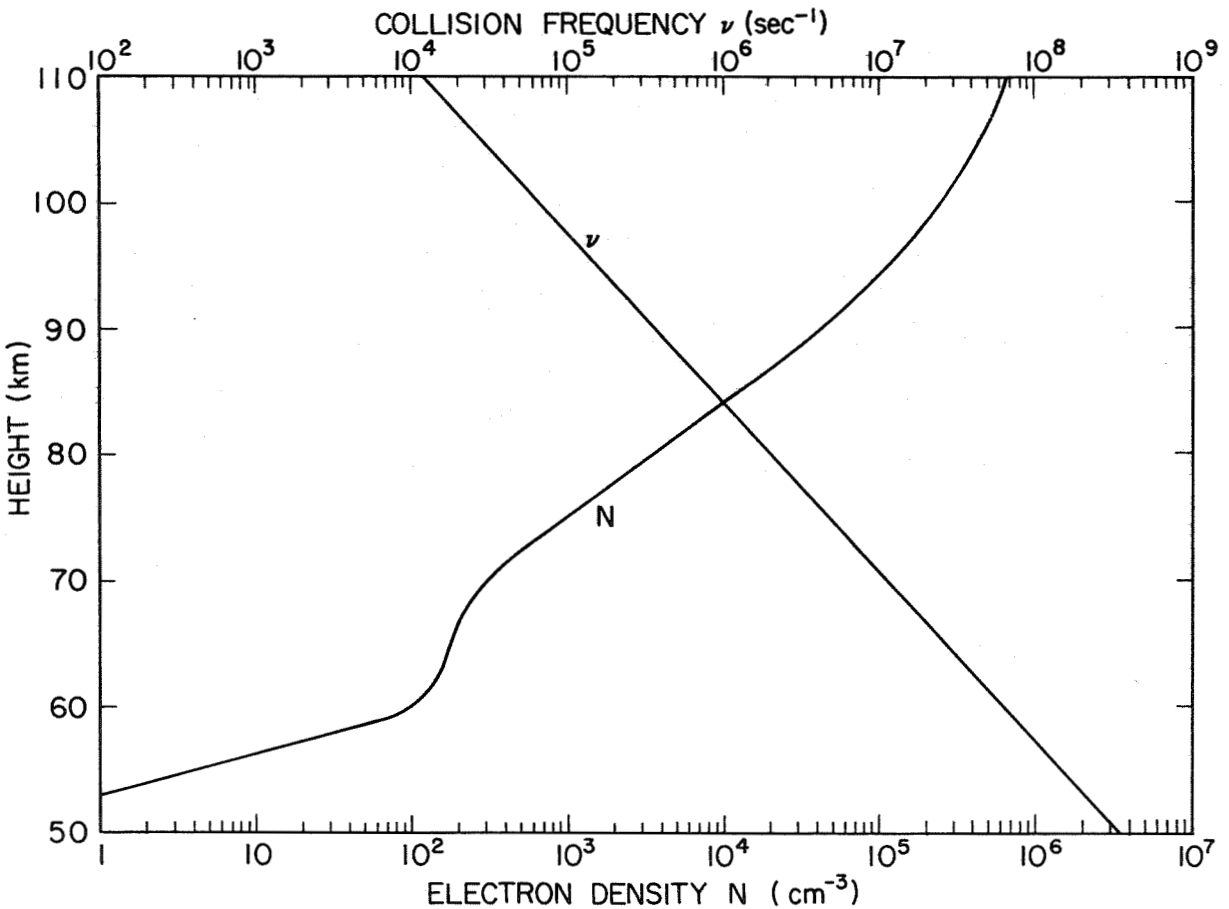

Figure 18. Height distributions of electron density at midday equinox (N) and electron collision frequency (ν) [Piggott et al., 1965].

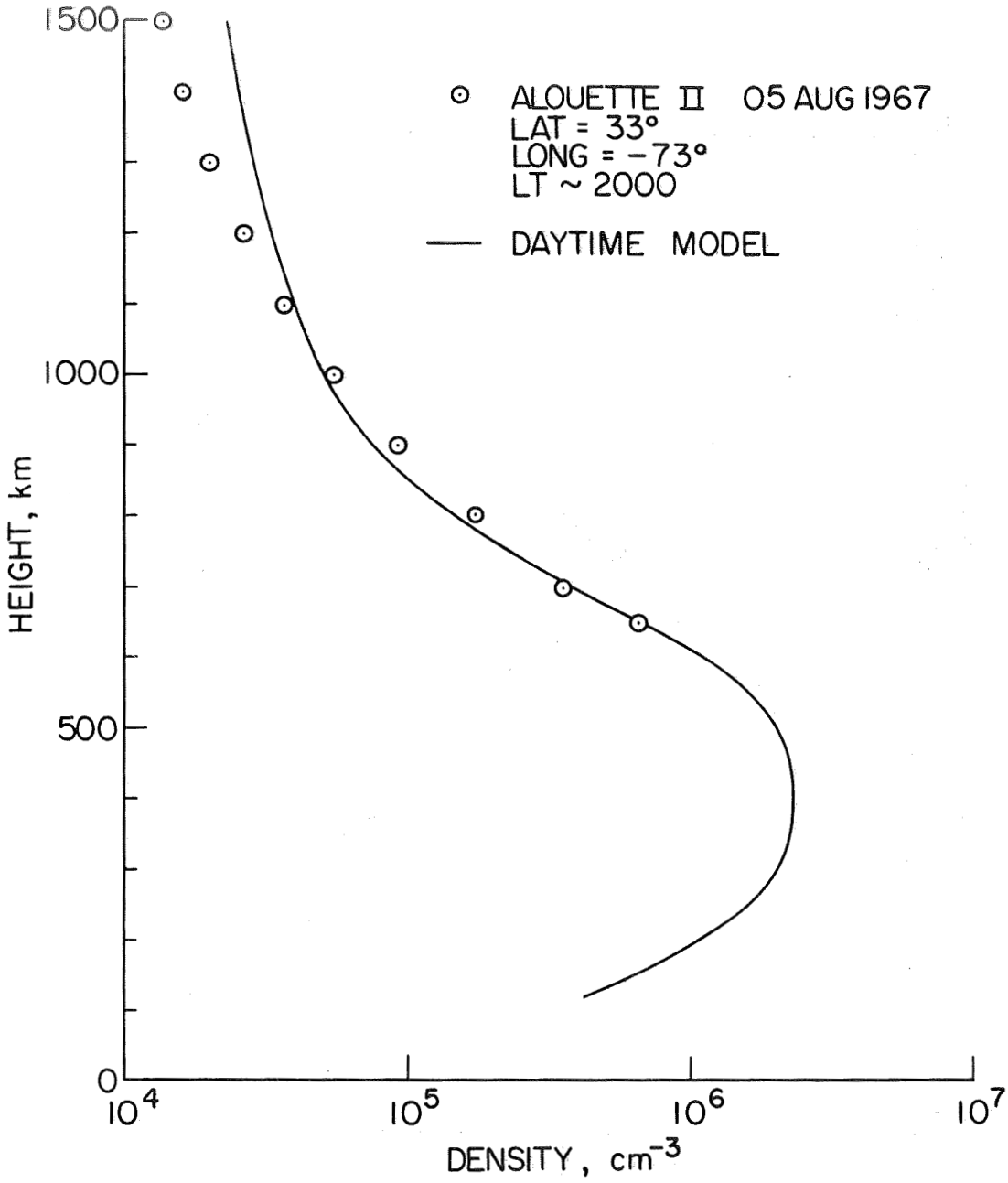

Figure 19. Daytime equatorial model of the ionosphere above 100 km. Electron-density measurements from Alouette 2 are also shown (data supplied by L. Colin).

Figure 20 gives the ionospheric loss L as a function of input magnetic latitude for a range of frequencies. The higher frequencies exhibit relatively greater losses, and both the amount of loss and its frequency dependence increase rapidly toward lower latitudes.

Figure 20 shows that if the receiver threshold is constant with frequency the highest frequencies should disappear first and the lowest frequencies later for a satellite approaching the equator. Thus the absorption analysis qualitatively explains the equatorial erosion effect.

For daytime ionospheric models the transmission loss is caused almost exclusively by absorption, the amount of loss introduced by reflection being comparatively small. Hence, the behavior shown in Figure 20 could be predicted with a simpler technique. As an example, curves of absorption given by Helliwell [1965, Chapter 3], which are based on the integral of the imaginary part of the refractive index, agree reasonably well with Figure 20.

3. Daytime Ray Trajectories Around the Equator

The next necessary step is to follow the ray trajectories in order to determine further effects and the satellite positions where the absorption introduced by the lower ionosphere will be detected. Figure 21 shows some 1 kHz ray paths produced by a ray-tracing computer program [Walter, 1969] using the ionospheric model shown in Figure 19. The illustrated rays start at the height of 120 km and at 8, 10, 12, and 14 degrees of latitude with vertical wave normals, as indicated by small arrows. The ray that starts at 8^{o} follows a trajectory well-inclined toward the equator because of the guiding effect of the magnetic field which has low dip angles at these latitudes. The result is that a substantial length of the ray trajectory occurs at the height of the bulge

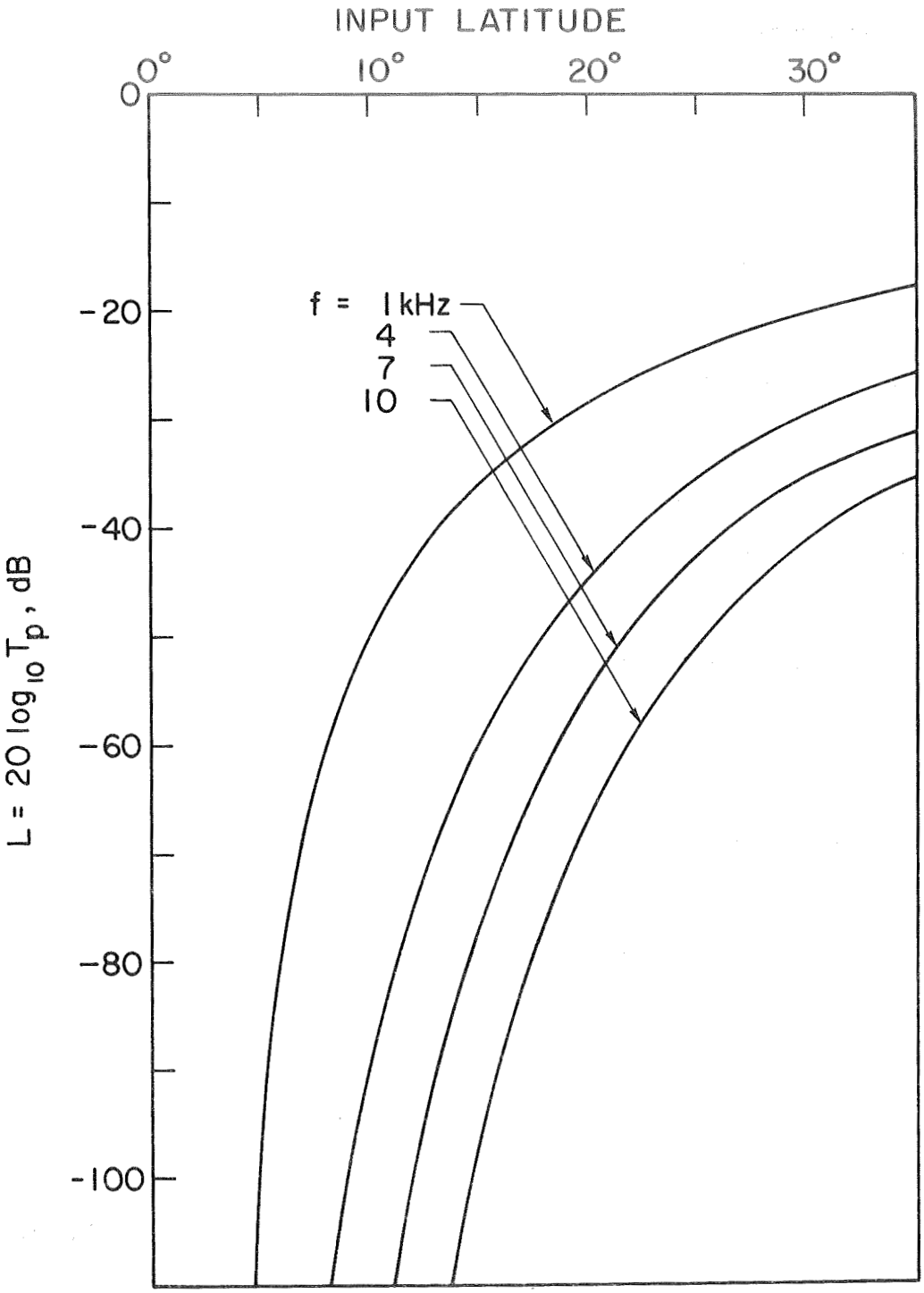

Figure 20. Total ionospheric loss (reflection plus absorption) as a function of magnetic latitude for several frequencies.

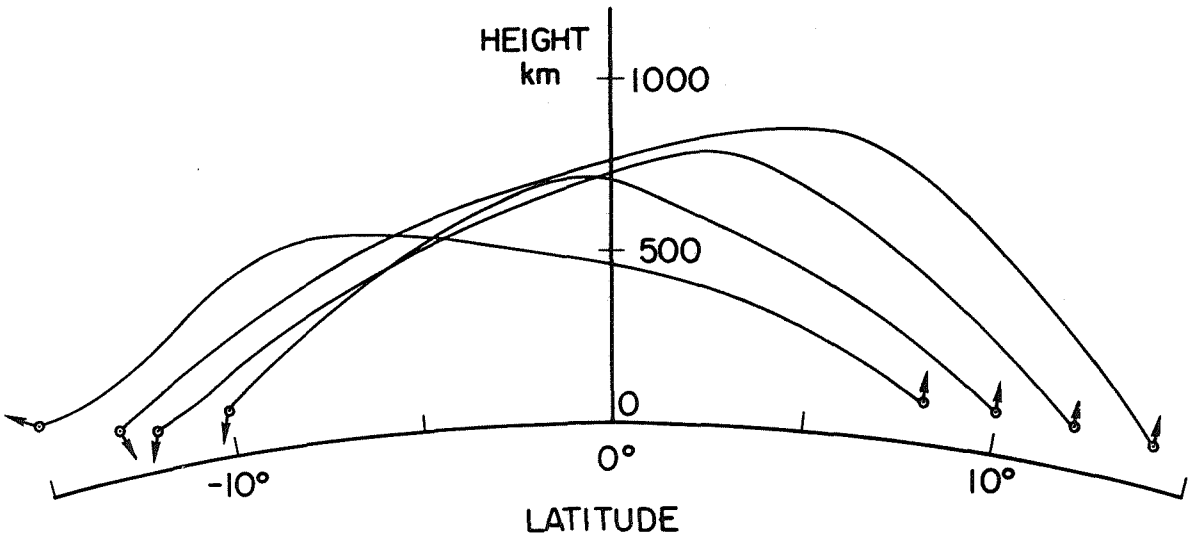

Figure 21. Ray trajectories for 1 kHz waves in the equatorial ionosphere using the electron-density model of Figure 10. The assumed dipole geomagnetic field has an equatorial gyrofrequency of 870 kHz at the ground.

region of the F-region where the vertical gradient of electron density is small. Therefore, the rate of change of the wave-normal direction which is primarily dependent on the vertical ionization gradient is also small. Hence the ray proceeds upward until higher gradients of electron density are met above 500 km which then bend the wave normal downward and the ray returns to the lower ionosphere.

Rays that start above 8^{o} of latitude are affected by magnetic field lines with higher dip angles and therefore the rays cross the F-region less obliquely (see Figure 21). Such rays will be affected by the high electron-density gradient above the F-region closer to the input latitude for successively higher input latitudes. As a consequence the apogees of the trajectories move from negative to positive latitudes when the input latitude varies from 8 to 14 degrees as shown in Figure 21. The resulting downgoing rays present the possibility of wave interference because of ray crossings and also some focusing caused by ray bunching. The ray trajectories for wave frequencies between 1 and 10 kHz are almost equal to the curves shown in Figure 21, the maximum difference being approximately half degree in latitude for some rays at 10 kHz. Therefore it is only necessary to show the propagation properties displayed by one wave frequency.

Figure 22 shows the relationship between the input latitude at 120 km where 1 kHz rays start and the latitudes where a 600 km polar-orbiting satellite would receive the rays (continuous curve) together with the related travel times (dashed curve). Figure 22 is to be used in the following way: Given an upgoing ray at a specified latitude (left side of figure) it will cross the height of 600 km at two latitudes, namely as an upgoing wave (section CD) or as a downgoing wave (section ABC).

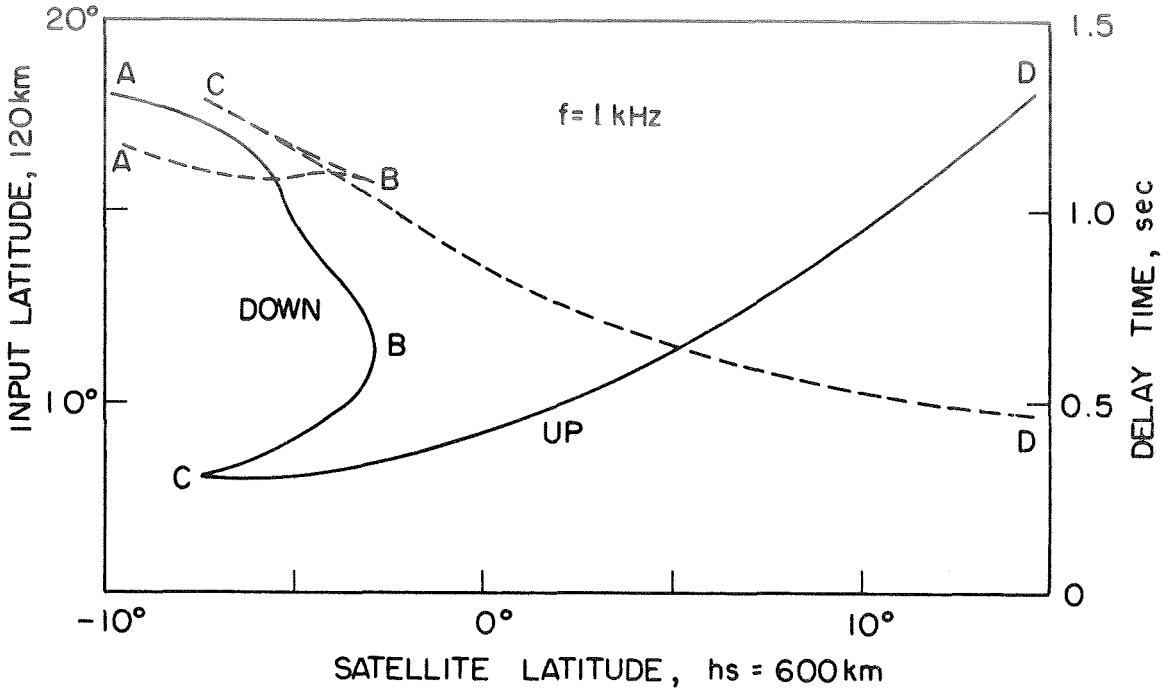

Figure 22. Input latitudes at 120 km and the related latitudes where 1 kHz rays will be detected by a 600 km polar-orbiting satellite. For a given satellite latitude (bottom) the related travel time can be read at the right hand side of the figure (dashed curve).

For a given satellite latitude the travel times are read on the right side of the figure. For example, a 1 kHz ray that starts at 10^{o} of latitude will be received by the satellite at 2^{o} as an upgoing wave with a delay time of 0.76 sec, and will also be detected at -3.6^{o} as a downoing wave with 1.10 sec time delay.

Figure 22 shows the fact already described by Figure 21 that the trajectories are not symmetrical around the equator: there is bunching of rays at negative latitudes and some divergence of rays at positive satellite latitudes. Numerical calculations indicate that the above divergence loss and focusing gain represent less than ±3 db, a number that is negligible in comparison with the low ionosphere absorption

shown in Figure 20. A strong focusing of rays may occur at point B where the derivative of the curve is infinite; this point will be discussed later.

Figure 22 also shows that wave interference should occur in a certain range of negative latitudes where rays that come from different starting latitudes are observed at one point. Although this statement is certainly true for a sinusoidal wave of long duration it requires a further discussion for the case of whistler reception where each wave frequency exists only during a short duration. For example, if the satellite location is -5^{o} it would receive 3 distinct rays (see Figure 22) whose delay times are 1.090, 1.155 and 1.170 seconds but the last 2 rays would appear as 2 distinct traces only if the duration of the 1 kHz packet is smaller than 15 milliseconds at the receiving point. Otherwise and more generally if two interfering rays are received at the same location they will produce wave interference only during the period when both packets coexist. The amplitude of the interfering waves may be very different because they were affected differently by the lower ionosphere absorption (as given in Figure 20) although the above effect may be compensated by the position of the lightning source relative to the entry points below the ionosphere. Therefore the complete picture of whistler interference near the equator is somewhat involved. It depends on several factors, namely ionospheric profile (controlling the delay times and trajectories), frequency, and relative positions of lightning source and satellite. Typical OGO-4 records of downgoing whistlers at low latitudes display fading in the whistler traces as well as the occurrence of almost coincident traces which sometimes merge together. The above features together with the erosion effect are present in the

OGO-4 spectrogram of Figure 16 at negative latitudes where downgoing whistlers are being received (see bottom panel).

Using Figure 22 the ionospheric loss of Figure 20 is related to the satellite latitude by following the ray trajectories up to 600 km. This is shown in Figure 23 for wave frequencies 1, 4, and 7 kHz. Figure 23 shows that the erosion effect should be unsymmetrical around the equator if the lightning sources are located at one side of the magnetic equator. For example, the curve for 1 kHz shows that for a northbound equatorial pass of a 600 km satellite the signal decreases 10 db between -5.4^{o} and -3^{o}. However, this loss is recovered north of the equator between 5^{o} and 11.6^{o}. Figure 23 also shows that the rate of loss with latitude is greater at higher frequencies.

The predicted focusing of the rays at the latitude B of Figure 22 is probably effective only at the low frequencies where ionospheric losses have not been excessively high. The focusing is ineffective at higher frequencies because these waves are absorbed by the lower ionospheric medium.

The asymmetry of the erosion effects around the equator is caused in part by the non-symmetrical ray trajectories around the equator and partially because of the response of the receiver under different regimes. This is the difference in the response of the satellite receiver to "short" upgoing whistlers and "dispersed" downgoing signals and the fact that upgoing whistlers were concentrated north of the magnetic equator and downgoing whistlers on the southern side. In the case of short upgoing whistlers received north of the equator the peak signal is large; the instantaneous AGC of the log-compressor receiver acts to lower the gain so as to reveal some amplitude details (hence the

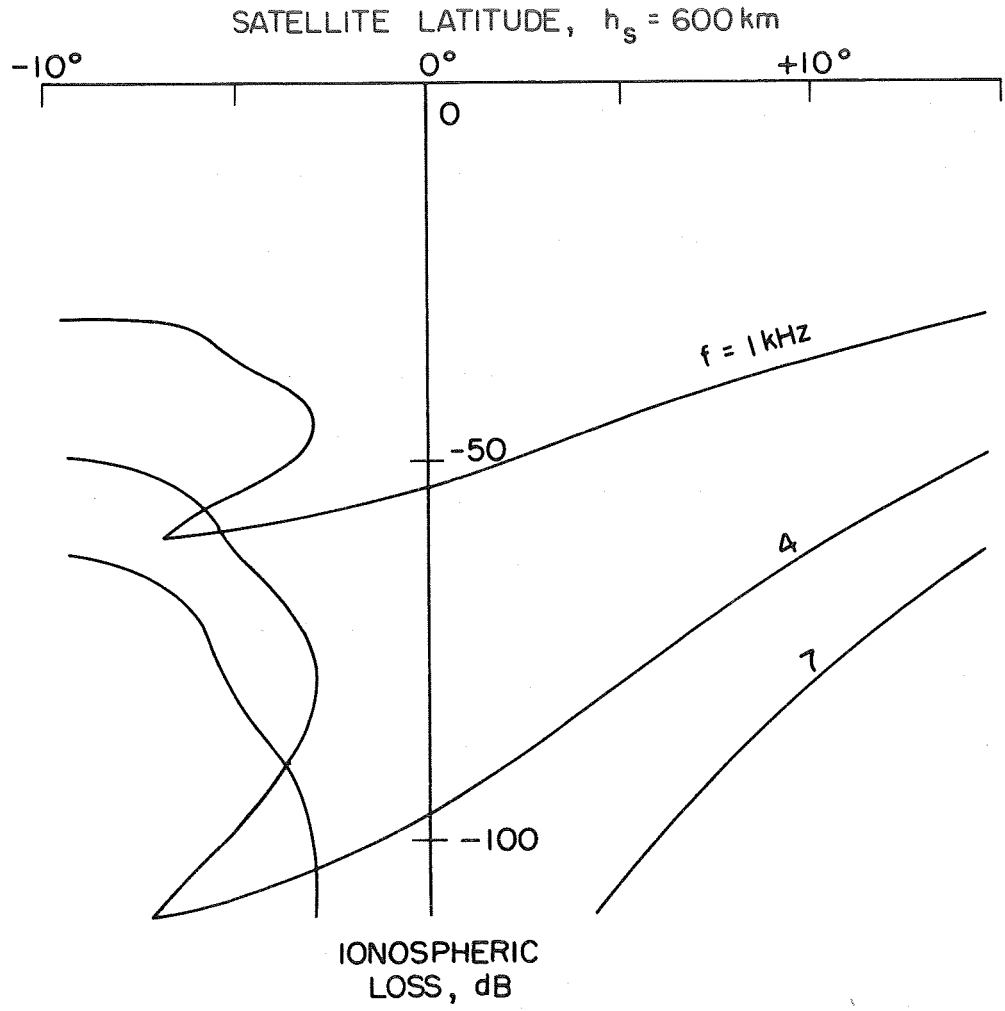

Figure 23. Ionospheric loss observed by a 600 km polar-orbiting satellite as a function of latitude. The curves are parametric in frequency.

irregular structure of Figure 16) that fall below a certain clip level. In the case of dispersed downgoing whistlers observed south of the equator the signal is on the average relatively weak and of long duration, the AGC action maintains high gain levels with much of the signal near the clip level and the result is an abrupt change in darkness of the display at the cutoff or beginning of high attenuation.

C. EQUATORIAL DEFOCUSING

At nighttime the transition height at which the equatorial ionosphere changes from a scale-height dominated by oxygen to a scale-height dominated by hydrogen is usually below 1000 km (see for example, Prasad [1968]). Therefore the vertical gradient of electron density may change rapidly between the peak of the F region and 1000 km. In what follows we use the results of a ray-tracing computer program [Walter, 1969] to analyze the effects of this change in ionization gradient upon the propagation characteristics of VLF waves.

Figure 24 shows some ray tracings for typical day and nighttime electron-density profiles. Both daytime and nighttime profiles simulate Alouette 1 topside measurements taken over the equator in November 1962. The ray path shown for the daytime profile (dashed curve) is more or less typical for waves starting between 5^{o} and 15^{o}, i.e., the ray trajectories are approximately symmetric around the equator. In this case the curvature of the earth's magnetic field plus the high vertical gradient of electron density above the F region provide a significant rate of change of the wave normal direction all the way along the path. As a consequence the wave normals bend initially toward the equator, cross the equator oriented almost horizontally and finally bend rapidly inward from the field line direction. These waves arrive in the D region

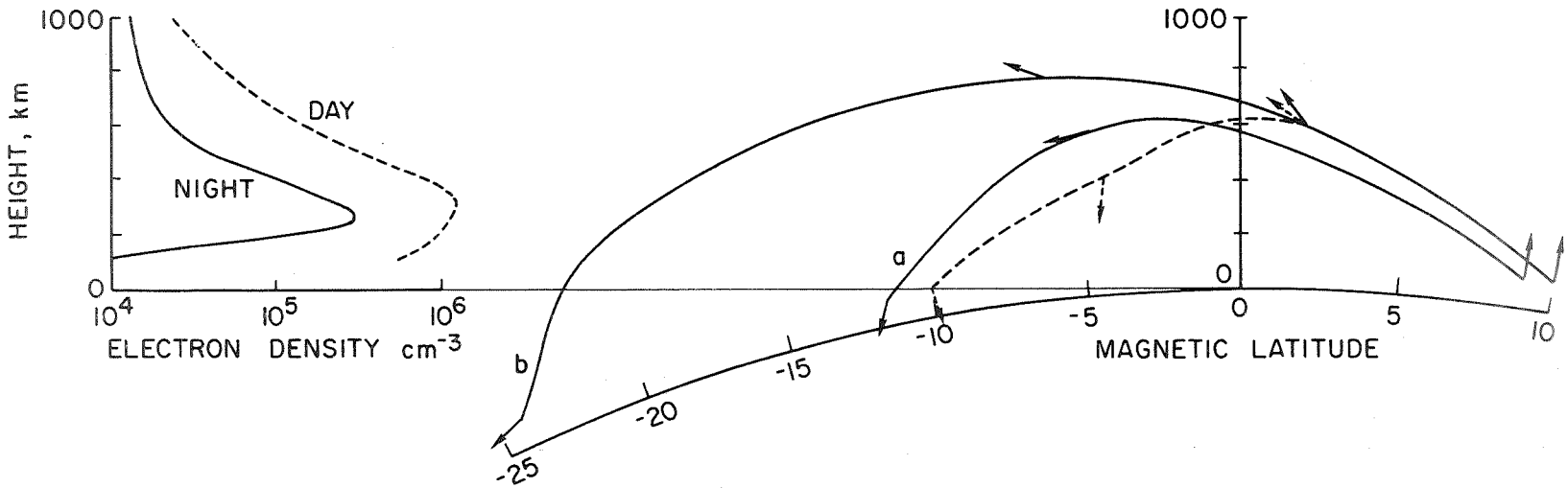

Figure 24. Typical daytime and nighttime ray trajectories followed by waves of 17.8 kHz near the magnetic equator. The directions of the wave normal are represented by small arrows, showing that the equatorial defocusing occurs when the medium loses the ability of effectively bending down the wave normal. This effect is caused by a weak vertical gradient above the transition height in the nighttime electron-density distribution.

of the conjugate hemisphere with almost vertical wave normals.

The two ray paths shown for the nighttime profile (solid curves) present two types of behavior. The ray path that starts at $+9^{o}$ is typical of waves whose incident latitude is relatively close to the equator. This path is similar to the one presented by the daytime curve, in that the wave normals bend rapidly earthward in the region of high vertical gradient of ionization below 600 km, where the nighttime profile is dominated by the O^{+} scale-height. The nighttime ray whose starting latitude is $+10^{o}$ presents a behavior that is typical for rays starting above $\sim 10^{o}$, i.e., it crosses the equator above the transition height. As a consequence, the rate of change of the ray direction, which is approximately proportional to the vertical gradient of ionization, is much smaller for this group of rays. Figure 24 shows that in this case the wave-normal remains pointing upward over a wide range of latitudes, bends slowly toward the horizontal, and finally bends rapidly earthward when the ray enters the region of low scale-height below the transition height. The differences in the behavior of the ray trajectories presented for the nighttime profile, depending on whether the ray crosses the equator above or below the transition height, produce the defocusing of the rays labeled a and b.

The defocusing phenomenon can be quantitatively analyzed if a relationship is found between the latitudes where the rays start and the latitudes where they should be intercepted by a satellite crossing the equatorial region at constant height. The result of such a calculation is shown in Figure 25 for the nighttime ionospheric model of Figure 24 and for two satellite heights, h_s = 450 and 700 km. Figure 25 shows that rays starting at a given input latitude (the independent variable)

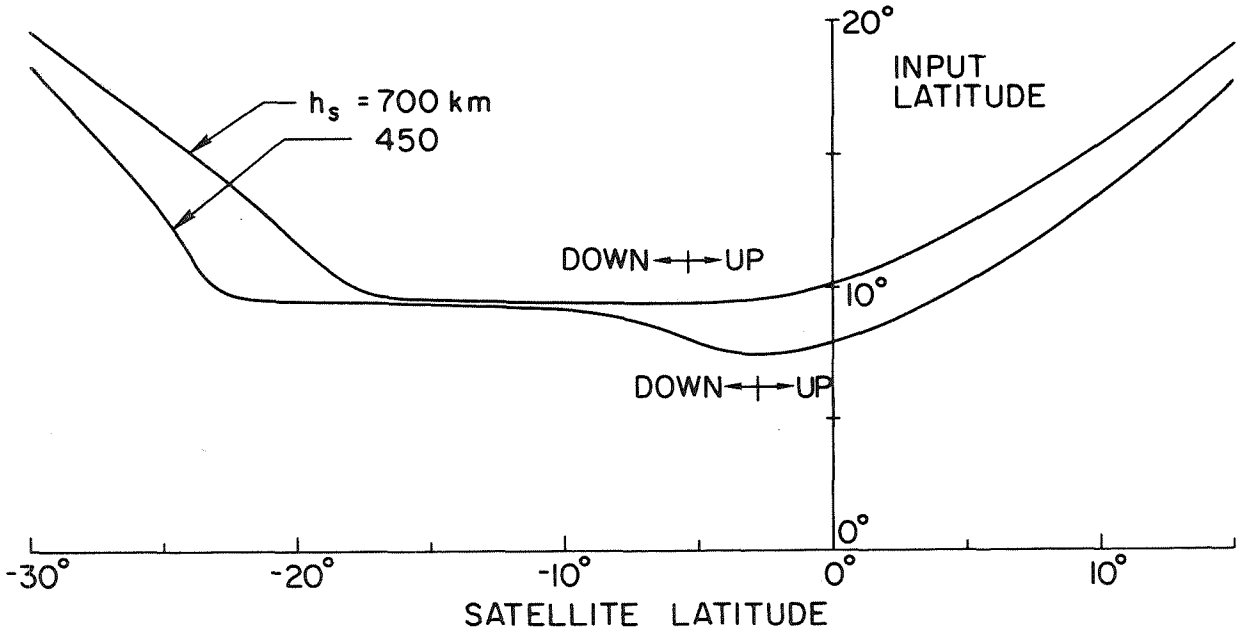

Figure 25. Correspondence between the latitudes where the rays leak from the earth's waveguide and the latitude where they will be detected by a satellite whose height is h_s. Arrows indicate the regions where upgoing (UP) and downgoing (DOWN) rays are received. The height at the input latitude is 120 km where the wave normals are assumed vertical. The ionospheric model is the nighttime profile shown in Figure 24. The assumed dipole geomagnetic field has an equatorial gyrofrequency of 870 kHz at the ground.

may obviously be detected by a satellite in two different ways: as upgoing or as downcoming waves. Arrows indicate the satellite latitudes for which the rays will be detected as upgoing (UP) or downcoming (DOWN) waves. For example, the curve for h_s = 450 km shows that rays whose input latitude is 8.5^o will intercept the satellite at 2^o latitude as upgoing waves and at -6.5^o latitude as downgoing waves. Little defocusing loss is predicted for these rays. Defocusing loss is apparent where the curves are flat, meaning that there is a very wide range of latitude where the satellite will be receiving energy that comes from a very narrow range of input latitudes. Observe, for example that rays starting between 9^o and 9.6^o are detected upwardly between 3^o and 4^o by a satellite at 450 km and that the corresponding power flux will be weaker in the southern hemisphere because the downcoming rays will be detected from -9^o to -22^o latitude.

The focusing gain is defined by Eq. (2.6) and Figure 9. The factor $(\Delta\phi_i/\Delta\phi_s)$ is readily determined from Figure 25, and β is a side product of the ray-tracing computer program. Hence, the focusing gain can be calculated as a function of the latitude of the satellite. This is shown in Figure 26 for ray inputs in the northern hemisphere and for two different satellite heights, h_s = 450 and 700 km (solid curves). The calculations predict that the drop in the signal will occur when the satellite is in the hemisphere conjugate to that of the transmitter, and that the signal will decrease abruptly in space, in good agreement with the measurements as shown by the dashed curves. The calculations also indicate that the signal should recover at a slower rate which, again, is usually observed.

In order to compare the calculated focusing gain with the observations

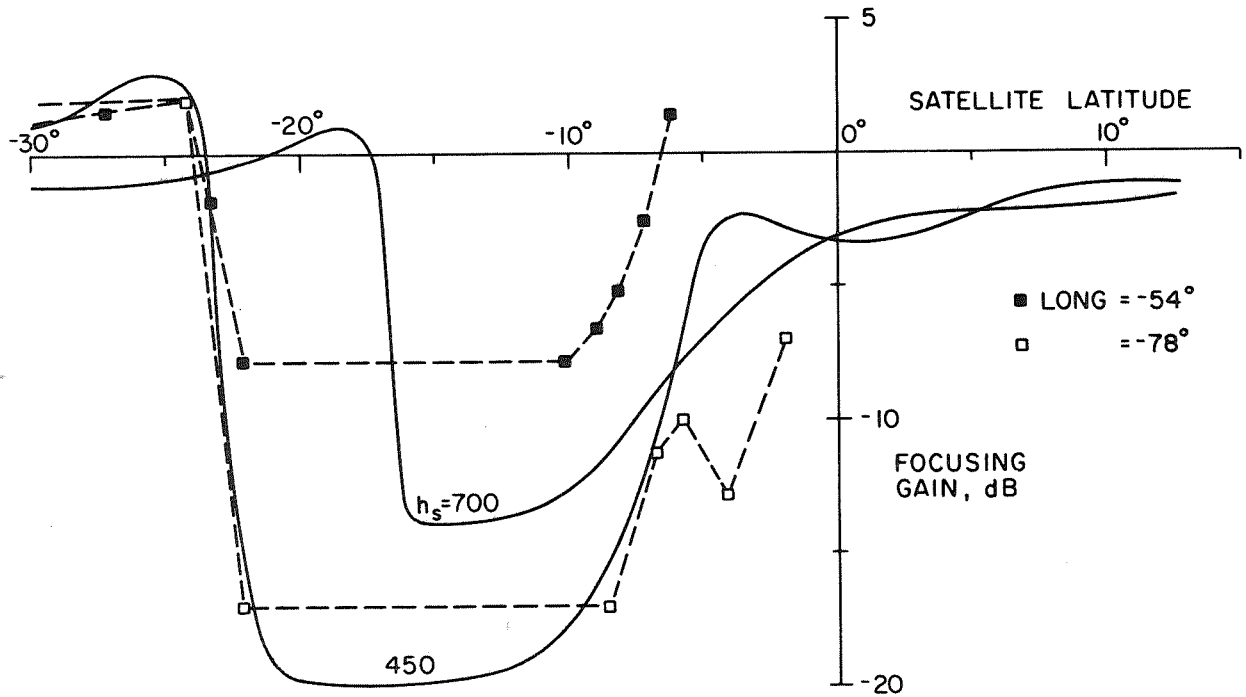

Figure 26. The continuous curves show the focusing gain as a function of the satellite latitude calculated for two different satellite heights, h_s = 450 and 700 km. The dashed curves represent the measurements shown in Figure 17 (OGO-4 height was 730 km at both equatorial crossings). For these experimental curves the relative starting signal level has been normalized to + 2db and the leading edge of the defocusing region has been placed at -24°.

it is necessary to normalize the amplitudes of the measurements made just before the equatorial defocusing. This has been done in Figure 26, by fixing the initial signal level at +2 db and placing the leading edge of the measured defocusing region at -24^{o}. The two consecutive measurements, separated by 25^{o} in longitude, present qualitative similarity but substantial differences in level. For example, Figure 17 shows that to the south of the defocusing region the upper record (longitude -54^{o}) presents smaller field levels compared with the bottom record (longitude -78^{o}). Because of this fact the noise level displayed by the records of Figure 17 inside the defocusing regions is represented in Figure 26 by flat lines 9 db apart, the higher line corresponding to the equatorial pass at the longitude -54^{o}. Figure 26 shows that the curve predicted for a satellite height of 450 km is the one that reasonably matches the observed defocusing for the pass of LONG = -78^{o}, although OGO-4 height was 730 km. It will be shown that this fact suggests a higher transition height for the ionosphere at -78^{o} longitude. This point will be discussed in the next section.

Nighttime ionospheric loss. Next, it is proposed to determine the role played by the lower ionosphere during the night. In order to estimate the leakage of the earth-ionosphere wave guide at different magnetic latitudes the following procedure is taken. The leakage of the dominant wave guide mode $n = 1$ is produced by waves whose angle of incidence in the lower ionosphere is $\sim 80^{o}$ [Wait, 1962]. The full wave computer program is then used in order to determine the transmission loss as a function of the latitude for a constant 80^{o} angle of incidence. The nighttime electron density (model b) and collision-frequency profiles were taken from Deeks [1966a] (see Figure 5). The result is shown in

Figure 27 where the transmission loss is plotted for different input latitudes and for waves traveling southward from NAA. It shows that the transmission coefficient is maximum at $\sim 14^{o}$ latitude, experiences at sharp decay at latitudes below 10^{o} and falls to zero at -6^{o} latitude. In the southern hemisphere the transmission coefficient recovers slowly, reaching significant values again only for latitudes below -45^{o}. These abnormally low values for the transmission coefficient come from the fact that at ionospheric heights where the wave normals are changing direction from -80^{o} to almost vertical, the wave normal crosses a region of high collision frequency while making an angle of nearly 90^{o} with the earth's magnetic field. Figure 27 is in good qualitative agreement with a similar study made by Pitteway and Jespersen [1966] for a different low ionosphere. Figure 27 leads to three conclusions:

1. The sharp decay of the transmission coefficient below 10^{o} does not interfere with the equatorial defocusing, because the satellite height is such that it will only receive rays which start above $\sim 9^{o}$ latitude (see Figure 25).
2. Between 0^{o} and -20^{o} latitude the transmission coefficient is so small that signals coming from below cannot be detected in the defocusing region of Figure 26.
3. The region of high transmission coefficient for whistlers excited from one side of the equator coincides with the low transmission coefficient region for whistlers excited in the opposite hemisphere and vice-versa.

Conclusions (1) and (2) substantiate the results previously provided by the ray-tracing technique, i.e., a region of defocusing for waves starting below the ionosphere and coming from one side of the equator should be observed. Conclusion (3) notes that the equatorial erosion cannot be observed during the night because the defocusing region for

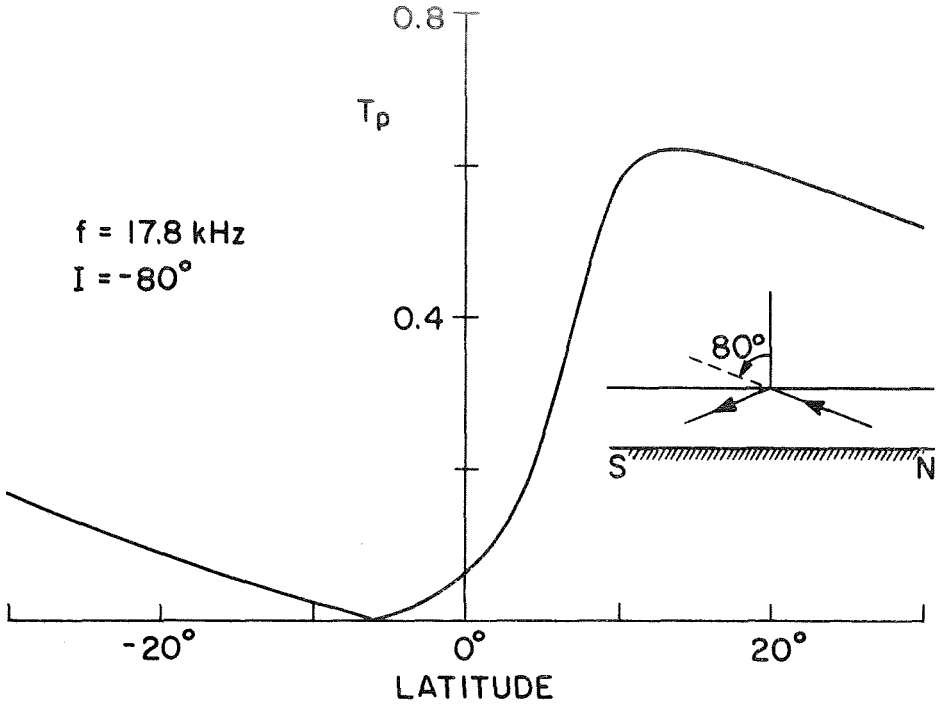

Figure 27. Lower-ionosphere transmission coefficient for penetrating mode waves traveling southward. The propagation is assumed to be in the magnetic meridian and the angle of incidence is -80° as indicated in the sketch by the curve.

whistlers generated in one hemisphere is filled with upgoing whistlers from the other hemisphere and vice-versa. Only a short dispersion characteristic for whistlers inside the defocusing region corresponding to upgoing whistlers should be observed; this phenomenon has been observed.

D. FACTORS AFFECTING THE EQUATORIAL DEFOCUSING

As we pointed out previously the equatorial defocusing is directly related to the change of the electron-density scale-height at the

transition height. Between the peak of the F region and the $[O^+ - H^+]$ transition height the vertical density gradient is usually high because the electron scale-height is almost exclusively given by the scale-height of O^+. As a consequence the ray trajectories below the transition height remain reasonably unchanged for different ionizations. For example, the nighttime and the daytime ray trajectories shown in Figure 24 are exactly the same below the nighttime transition height although the two ionospheric profiles present substantially different electron-density levels.

Above the transition height the defocusing is controlled by the H^+ scale-height. A smaller H^+ scale-height produces a smaller defocusing loss. Another very important factor is the smoothness of the transition from the O^+ dominated region to the H^+ dominated region. If enough helium is present the transition region is smoothed out because the He^+ scale-height is only 4 times greater than the O^+ scale-height. A smooth transition profile around the transition height produces a smaller defocusing loss. Hence, a strong equatorial defocusing is an indication that the He^+ concentration around the transition height is necessarily very small.

In order to give a numerical treatment to the above discussion we shall consider the three different ionospheric models A, B, and C shown in Figure 28. The ionospheric models have been calculated assuming a diffusive equilibrium distribution [Angerami and Thomas, 1964]. Profile A is the nighttime model previously shown in Figure 24. This model has an H^+ scale-height of 1600 km (i.e., a neutral H scale-height of 800 km). Profile C has an H^+ scale-height of 1120 km, namely 70% of the H^+ scale-height presented by profile A. Profile B is obtained

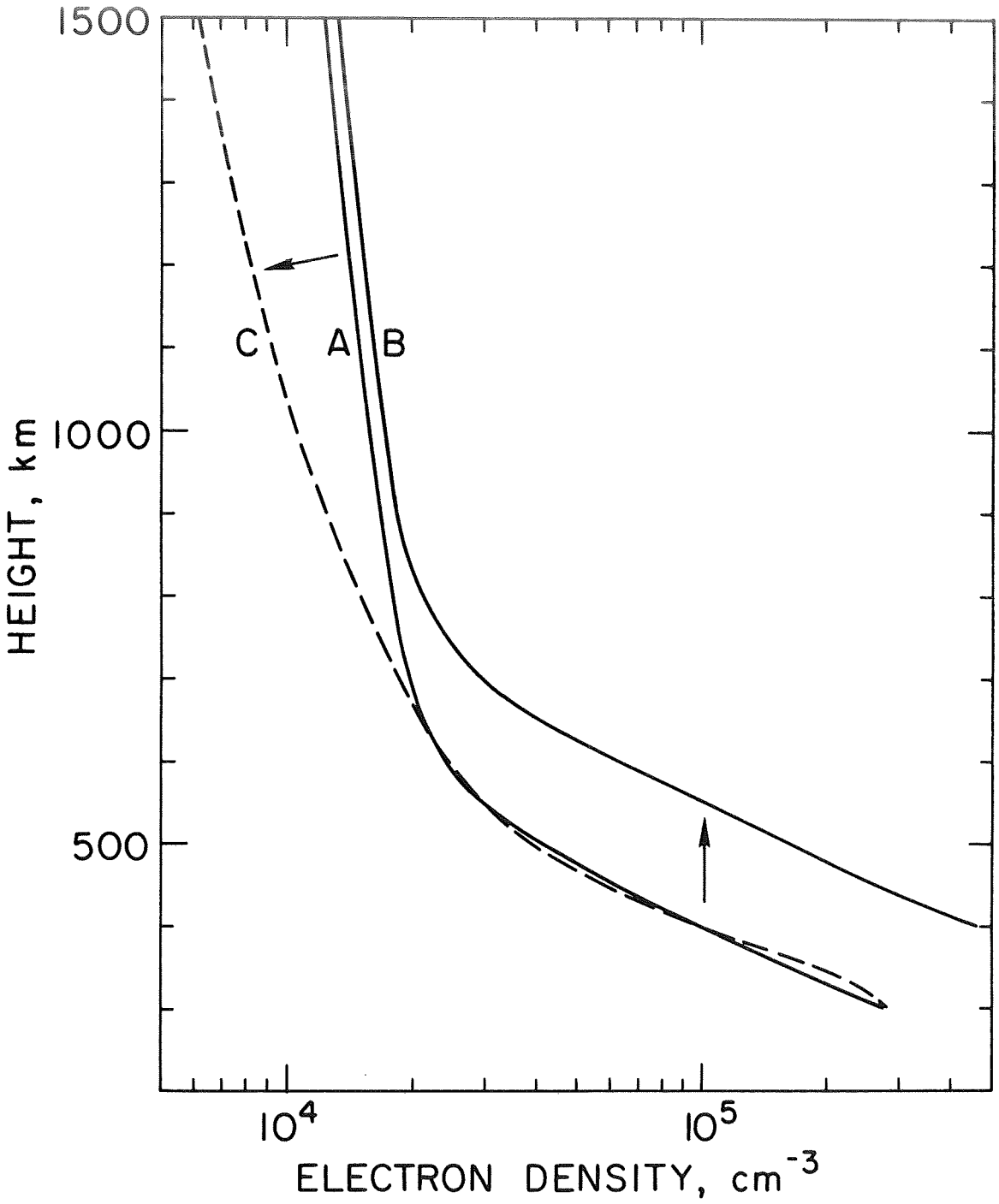

Figure 28. Three ionospheric models A, B, and C. Model A is the nighttime model of Figure 24. Model B is obtained from A by increasing the transition height. Model C has a hydrogen scale-height 70% of the hydrogen scale-height of Model A.

from A, essentially increasing the transition height by about 150 km. Figure 29 is the result of several ray-tracing computations showing the satellite latitude where the rays will be detected as a function of the latitudes where they start. Curves for the ionospheric models B and C are shown where the satellite height has been assumed equal to 700 km. These results can be compared with the results for profile A shown in Figure 25. Figure 29 indicates that the ionospheric model C gives no substantial defocusing (observe the derivative $d\phi_s/d\phi_i$). Calculations show that the maximum defocusing for this model is around 5 db for a satellite height of 700 km. In contrast, profile B produces a strong defocusing as we should expect because the corresponding electron density distribution is essentially the same as profile A but vertically shifted. Observe that the B curve in Figure 29 resembles the curve corresponding to h_s = 450 km in Figure 25. Figure 30 gives the focusing gain for this ionospheric model B as a function of the satellite latitude for h_s = 700 km. Notice that the calculated defocusing region has a length very similar to the one presented by the curve for h_s = 450 km in Figure 26. This indicates that we can effectively modify the ionospheric model in order to obtain a prescribed result. Another feature introduced by profile B relative to profile A is a northward shifting of $\sim 5^o$ in the position of the defocusing region and a fraction of db in loss (compare with Figure 26). In Figure 30 we also show the satellite measurements for the equatorial pass corresponding to LONG = -78^o. A very good agreement is now obtained.

The transition height for model B is 750 km, a value that suits the extrapolation of the midnight transition height curves given by Prasad [1968] which were based on the analysis of frequency spectrum of

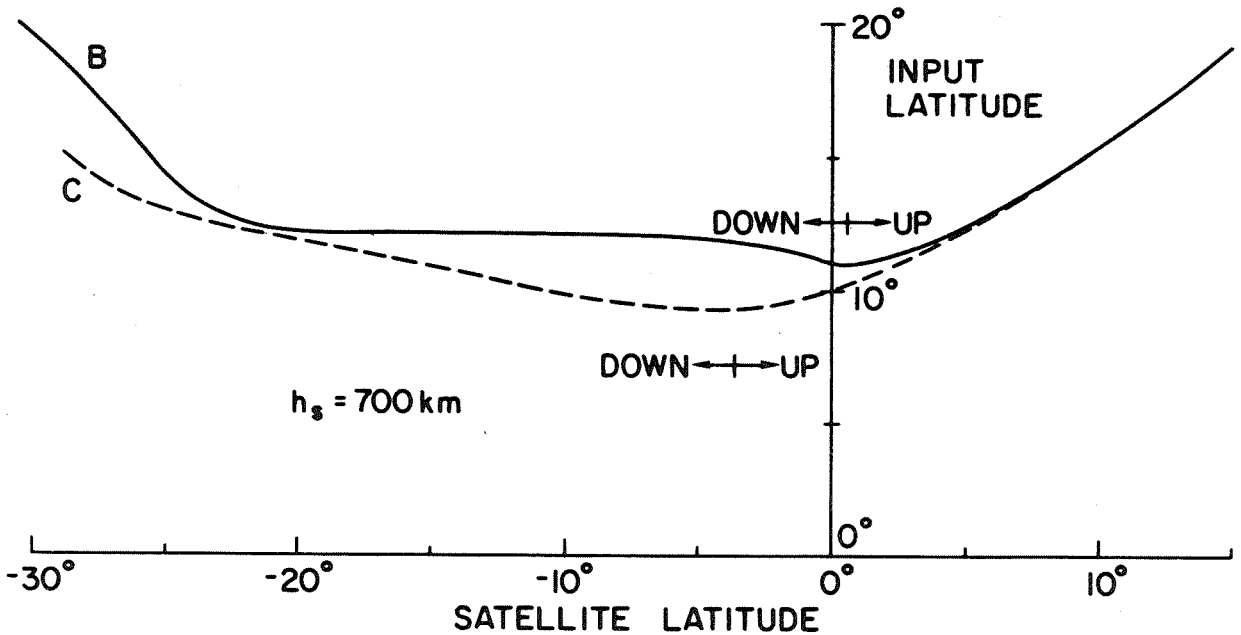

Figure 29. Correspondence between the latitudes where the rays leak from the earth's waveguide and the latitude where they will be detected by a satellite at 700 km for the two ionospheric models B and C. Compare with the curves derived for Model A in Figure 25.

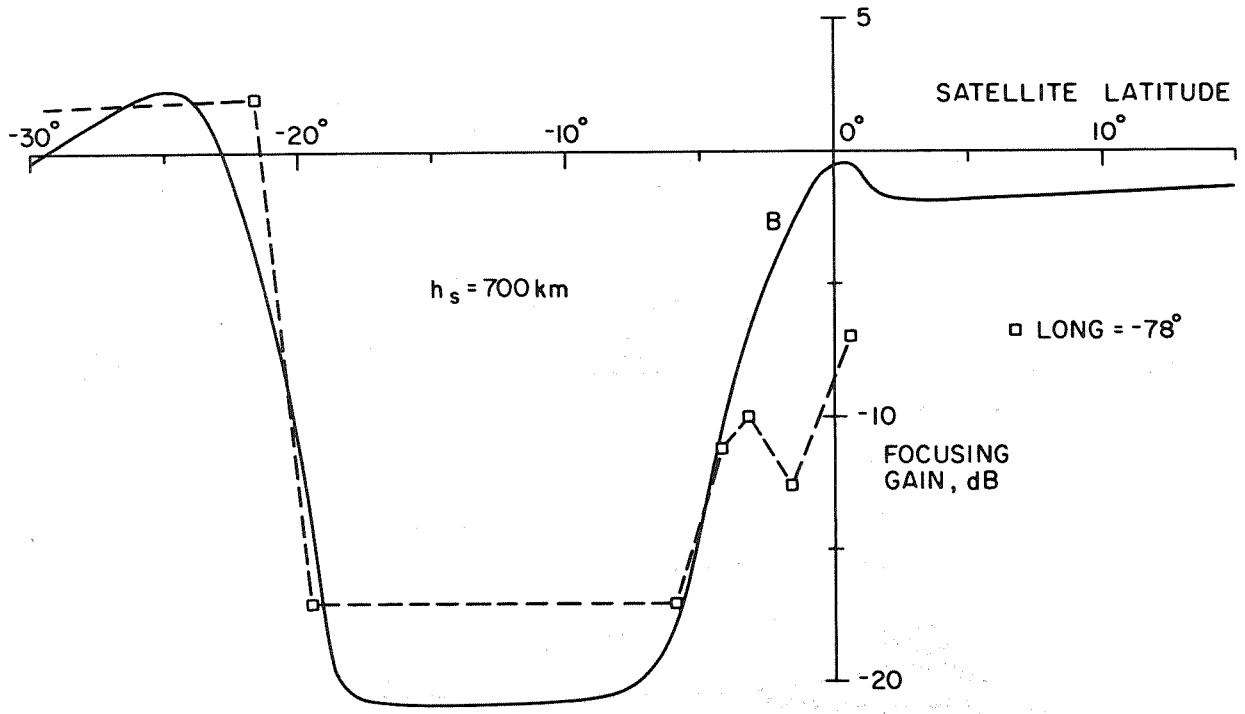

Figure 30. The continuous curves show the focusing gain as a function of the satellite latitude for ionospheric model B. The dashed curve represents one of the measurements shown in Figure 17. For the experimental curve the starting signal level has been normalized to +2db and the leading edge of the defocusing region has been place at -24^{o}.

radar backscatter signals from the ionosphere.

A discrepancy still remains, namely that the place of the calculated defocusing region is shifted about 10^{o} southward relative to the measured defocusing region of Figure 17. This point will be discussed in the next section.

E. SEASONAL VARIATION OF THE EQUATORIAL DEFOCUSING

Measurements of the equatorial defocusing between November 1967 and July 1968 suggest a seasonal variation in the magnetic latitudes where the equatorial defocusing takes place. This is shown in Figure 31 where the defocusing region is indicated by the position of vertical bars along some satellite passes. They show that the defocusing region for transmitters located in the northern hemisphere occurs just below the magnetic equator (as predicted) for months in which the sun's declination is negative. For months of positive declination of the sun (northern hemisphere summer) the defocusing region seems to move northward. A detailed study of this northward shift is difficult because the passes shown in Figure 31 have occurred at different local times as illustrated in the same figure by the numbers below each date. Therefore it is speculative whether the northward shift presented in Figure 31 is caused only by a seasonal variation in the ionosphere or whether the influence of local time may be a cause. Nevertheless, based only on the propagation properties of the waves, it is suggested that the northward shift of the defocusing region during the northern hemisphere solstice is caused by horizontal gradients of electron density near the magnetic equator. The direction of the latitudinal gradient for obtaining this effect should be northward, in accordance with electron density measurements made by

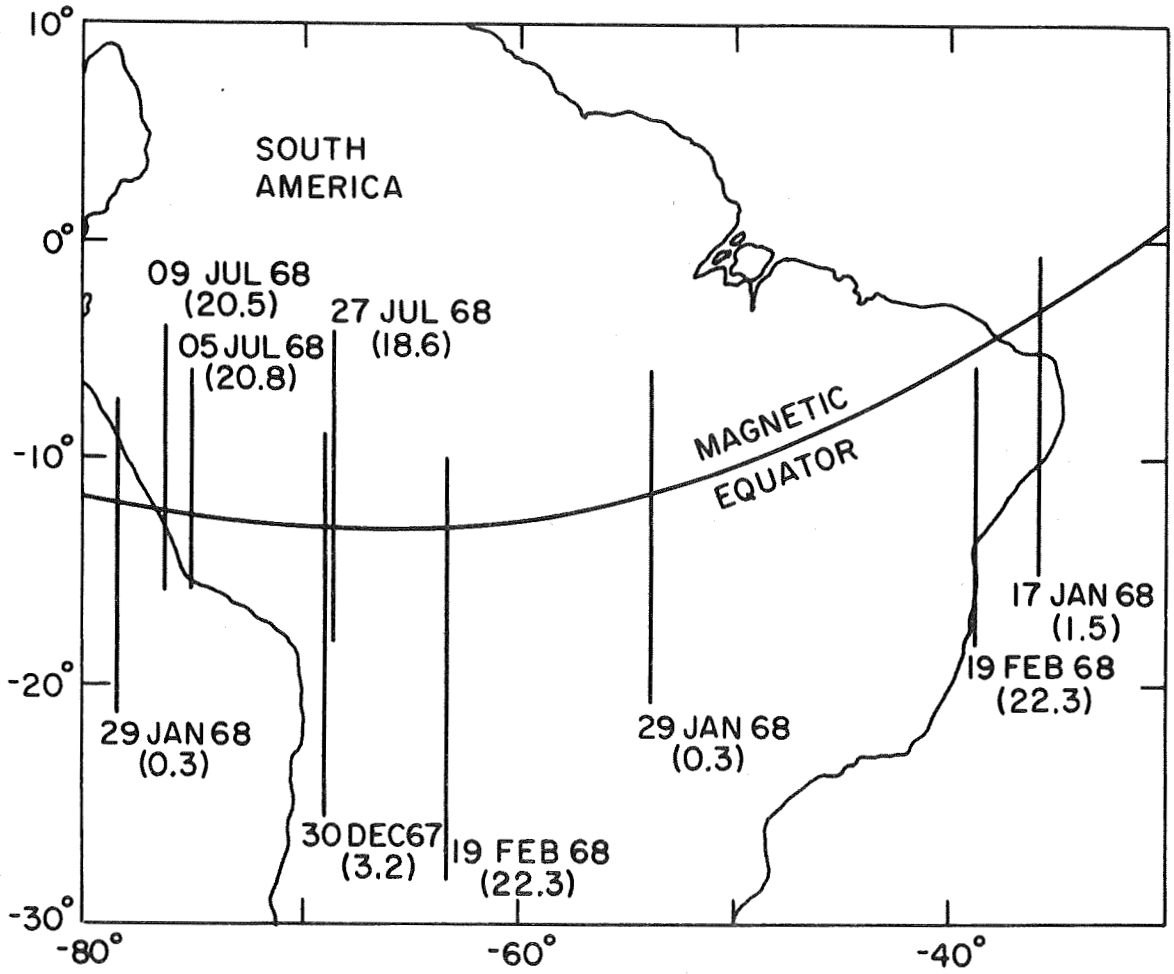

Figure 31. Position of the defocusing region relative to the magnetic equator. The figure suggests a northward movement of the defocusing region in the northern hemisphere summer months. The number below each date is the local time at the crossing of the equator.

Reddy et al. [1967]. This problem can be analyzed when a more complete seasonal behavior of the equatorial defocusing is known.

F. CONCLUSIONS

In this chapter we have presented the equatorial erosion and the equatorial defocusing of VLF waves propagating at low magnetic latitudes. It has been shown that the equatorial erosion is caused by ionospheric losses (absorption plus reflection) in the D region. These losses increase for lower latitudes and may cause the complete disappearance of all VLF waves from the receiver of a low altitude satellite. During the night absorption is less important but nevetheless a very pronounced drop in the signals of VLF transmitters has been observed. We showed that this new phenomenon is caused by ionospheric defocusing of VLF rays near the magnetic equator. This defocusing is related to the change of the vertical gradient of the electron-density distribution that takes place around the transition height. A full-wave treatment has been applied to the propagation through the lower nighttime ionosphere. This study confirmed the defocusing interpretation by showing that upgoing rays were prevented from reaching the defocusing region by excessive ionospheric loss in the lower ionosphere. Finally we showed that the ionospheric model can be modified in order to obtain a prescribed equatorial defocusing pattern. Given the satellite height we can approximately state that:

1. the amount of the defocusing loss can only be achieved with a hydrogen scale-height greater than a specified value;
2. the width of the defocusing region determines the minimum height of the transition region of the ionosphere;
3. the position of the defocusing region relative to the magnetic

equator will be a measure of the horizontal gradient in the ionosphere.

Although these three steps are not completely independent, they change the equatorial defocusing in the way indicated above.

The above process of matching a measured defocusing loss by suitable changes in a basic ionospheric distribution represents a potential diagnostic tool for obtaining the $[O^+ - H^+]$ transition height and the hydrogen temperature in the equatorial ionosphere. As pointed out previously the defocusing phenomenon is highly sensitive to the height of the $[O^+ - H^+]$ transition and hydrogen temperature just above that height. On the other hand the phenomenon is relatively unaffected by different electron distributions below the transition height (compare for example the upgoing sections of the ray trajectories for nighttime and daytime profiles of Figure 24). Therefore, in order to fit a specified defocusing measurement the most important parameters are the transition height and hydrogen temperature, regardless of possible discrepancies between the assumed profile and the actual ionospheric profile. Further development of this propagation method could provide indirect measurements whose accuracies might compete with presently available processes of measuring transition height and temperature. Obviously the suggested method can only be applied at the magnetic equator and during nighttime because there is no significant defocusing during the day. However, the process would provide measurements at all longitudes and the cost of analyzing the data is relatively low.

IV. OGO-4 AMPLITUDE MEASUREMENTS OF SIGNALS GENERATED BY GROUND VLF TRANSMITTERS

In this chapter we discuss the general features presented by the measurements of amplitude of VLF signals, generated by ground-based transmitters, as observed during the polar revolutions of OGO 4 around the earth. Two aspects of these measurements have already been considered, corresponding to reception of waves in the nearby ionosphere of the transmitter (Chapter 2) and equatorial phenomena (Chapter 3). The discussion of the measurements given here is intended to be more specific than the introductory considerations of Chapter 1, Section D. It will be followed by a detailed study of the controlling parameters affecting the waves that propagate from the hemisphere of origin to the conjugate hemisphere. As will be shown, the theory of wave propagation derived from that study is one of the most important results of this research.

A. NIGHTTIME MEASUREMENTS

Figure 32 shows nighttime measurements of the magnetic field of waves transmitted by the VLF station NAA at 17.8 kHz and recorded aboard OGO 4 by the phase tracking receiver. The corresponding position of the satellite is shown in Figure 33. Panels A-B, B-C, C-D, and E-F of Figure 32 correspond to the orbit segments shown in Figure 33. The panels of Figure 32 show the amplitude of the magnetic field in dbγ as a function of time and L value of the satellite. Between A and D the satellite moves approximately from one magnetic pole to the other (from L = 33 at 0330 UT to L = 38 at 0420 UT) in a half orbit period. Panel E-F corresponds to measurements taken 50 minutes later and is displayed here in order to show the repeatability of the main features

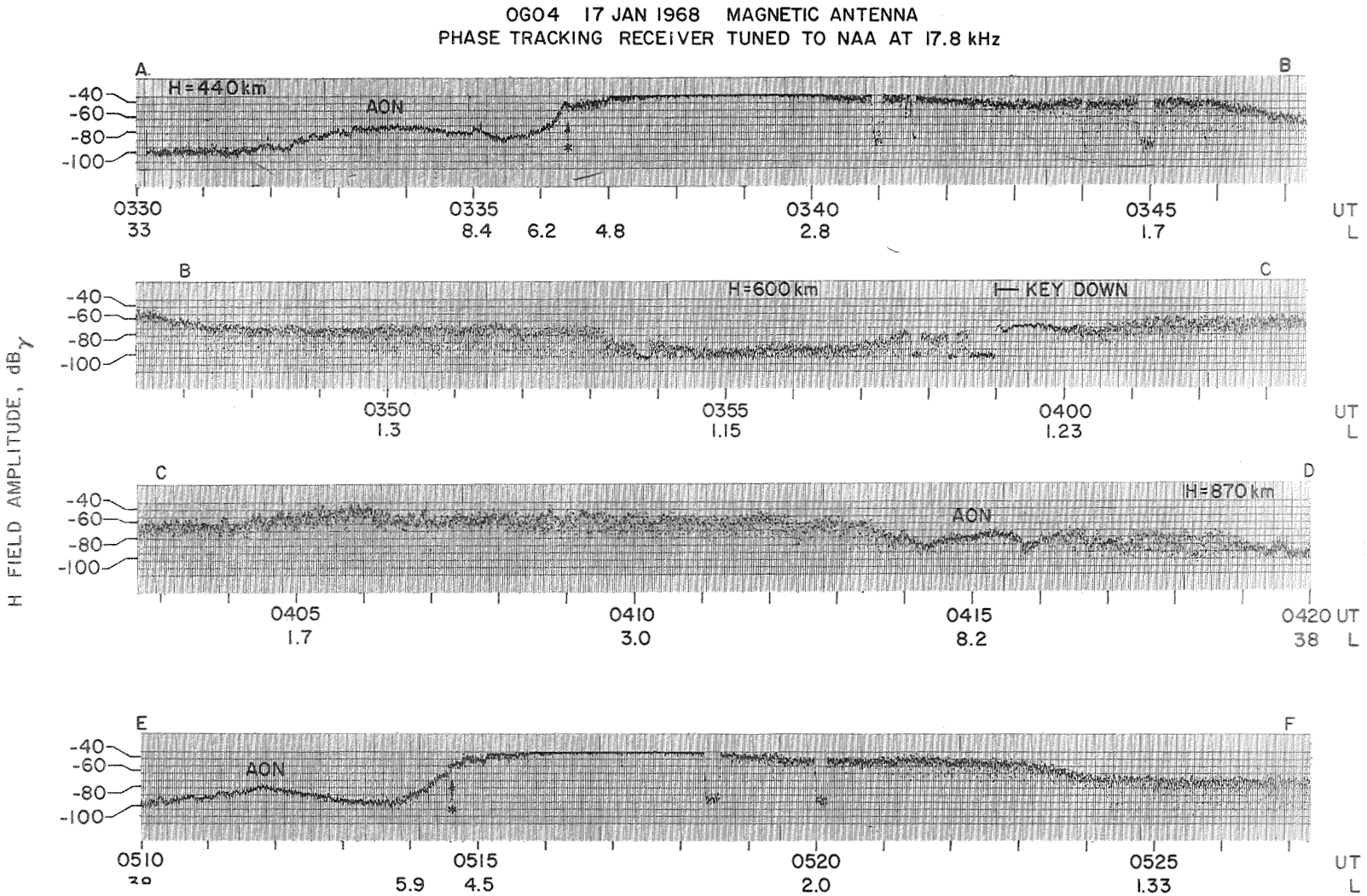

Figure 32. OGO-4 amplitude measurements of NAA signals at 17.8 kHz. Panels A-B, B-C, and C-D are sequential pieces of a continuous strip-chart, while E-F corresponds to measurements taken 50 minutes later and recorded in the same strip-chart. The corresponding satellite trajectories are shown in Figure 33.

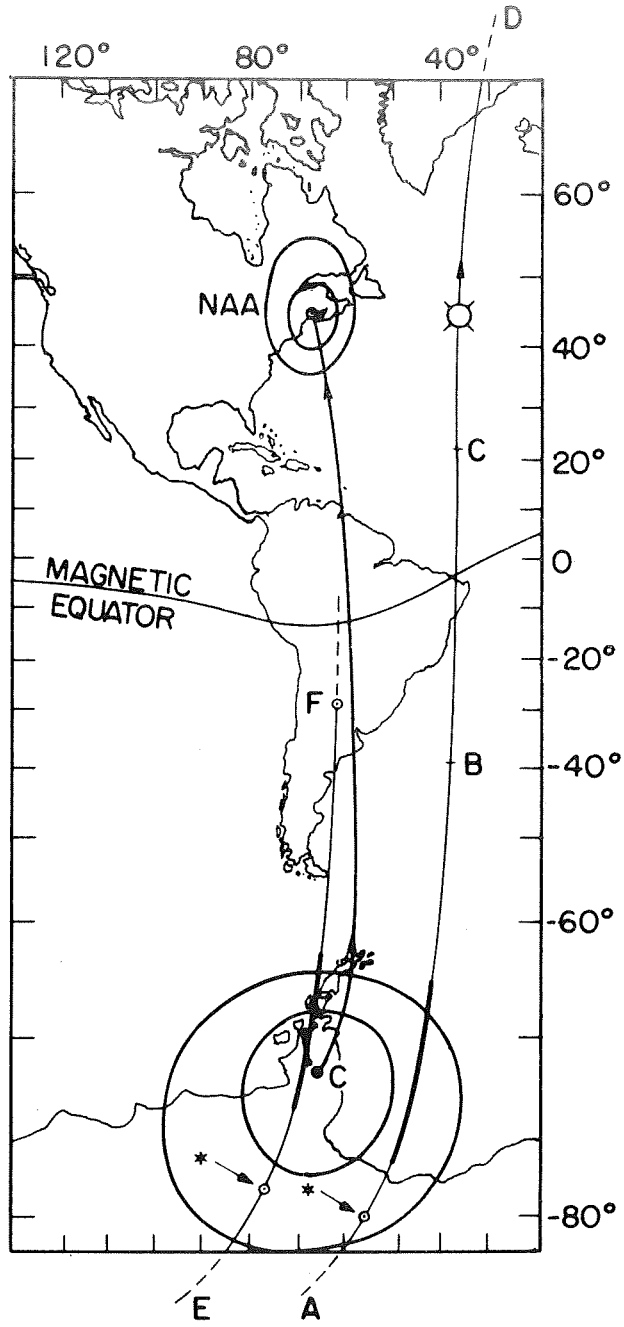

Figure 33. OGO-4 trajectories for Figure 32. Point C in the southern hemisphere is the magnetic conjugate of NAA. The two curves surrounding the transmitter are 10^{o}, 20^{o} wide in latitude and longitude, respectively. The corresponding conjugate regions are also drawn in the southern hemisphere.

recorded in A-B. The records of Figure 32 present properties that are typical for amplitude measurements taken when both transmitter and satellite are on the nightside of the earth. The main features displayed in the records of Figure 32 are discussed below.

1. Enhancement of the Signals in the Conjugate Region of the Transmitter

Panel A-B shows that the signals from NAA are very strong in the conjugate region of this station. The conjugate point for NAA and the conjugate locii for two curves surrounding the transmitter are shown in Figure 33. The regions where the signals are so strong that they saturate the receiver (see A-B or E-F) are shown in Figure 33 with a thicker line along the orbit in the conjugate region of NAA. Such high signal levels (above -30 dbγ) are usually measured when the satellite is in the neighborhood of the NAA transmitter. Therefore the measurements show that the fields in the F region near the transmitter are mapped into the southern conjugate ionosphere with negligible loss. In fact on some occasions an enhancement of a few db has been measured in the conjugate region.

2. High-Latitude "Erosion" in the Conjugate Hemisphere

Arrows indicate in panels A-B and E-F that near L = 5 there is a cutoff in the intensity of the signals from NAA. The corresponding satellite positions are also marked by arrows in Figure 33. Usually the magnetic field decreases by $\sim$ 70 db in a distance of 1^{o} to 4^{o} and the signal is generally not observed again above the cutoff magnetic latitude. This phenomenon has been observed previously aboard the OGO-2 satellite [Heyborne, 1966] and must not be confused with a high-latitude cutoff observed in the hemisphere of the transmitter recently reported by

Heyborne et al. [1969] (see paragraph (5) below).

The high-latitude cutoff in the conjugate hemisphere of NAA is in fact a particular case of a more general phenomenon detected in every OGO-4 pass, namely a high-latitude erosion of downcoming whistlers. The high-latitude erosion of downcoming whistlers and the cutoff in the intensity of the NAA signal are shown simultaneously in the OGO-4 spectrogram of Figure 34. Frequency ranging from 0 to 12.5 kHz is shown as a function of time and L value together with the frequencies of the voltage-controlled oscillator (VCO) modulated by the output of the stepping receiver No. 3 (upper trace). Observe that there is a complete absence of whistlers closer to the magnetic pole and that as the satellite travels equatorward the lowest frequencies of the downcoming whistlers appear first and the higher frequencies appear later. During this time signals are not received in Band 3 and only when the spectrum 0 - 12.5 kHz is completely filled with downcoming whistlers does the NAA signal rise out of the noise, as seen by the VCO. The high-latitude cutoff in the occurrence of whistlers has been reported by Carpenter et al. [1968] from Alouette 1 and 2 observations. There are other features in Figure 34 that will be discussed later.

3. Equatorial Defocusing

The signal levels from mid-latitude VLF transmitters decrease abruptly near the magnetic equator as shown in panel B-C of Figure 32. It has been shown in Chapter 3 that this phenomenon is caused by ionospheric defocusing related to the change in ionization gradient that occurs around the $[O^+ - H^+]$ transition height.

4. Enhancement of the Signals in the Hemisphere of the Transmitter

Panel C-D of Figure 32 presents measurements made in the northern

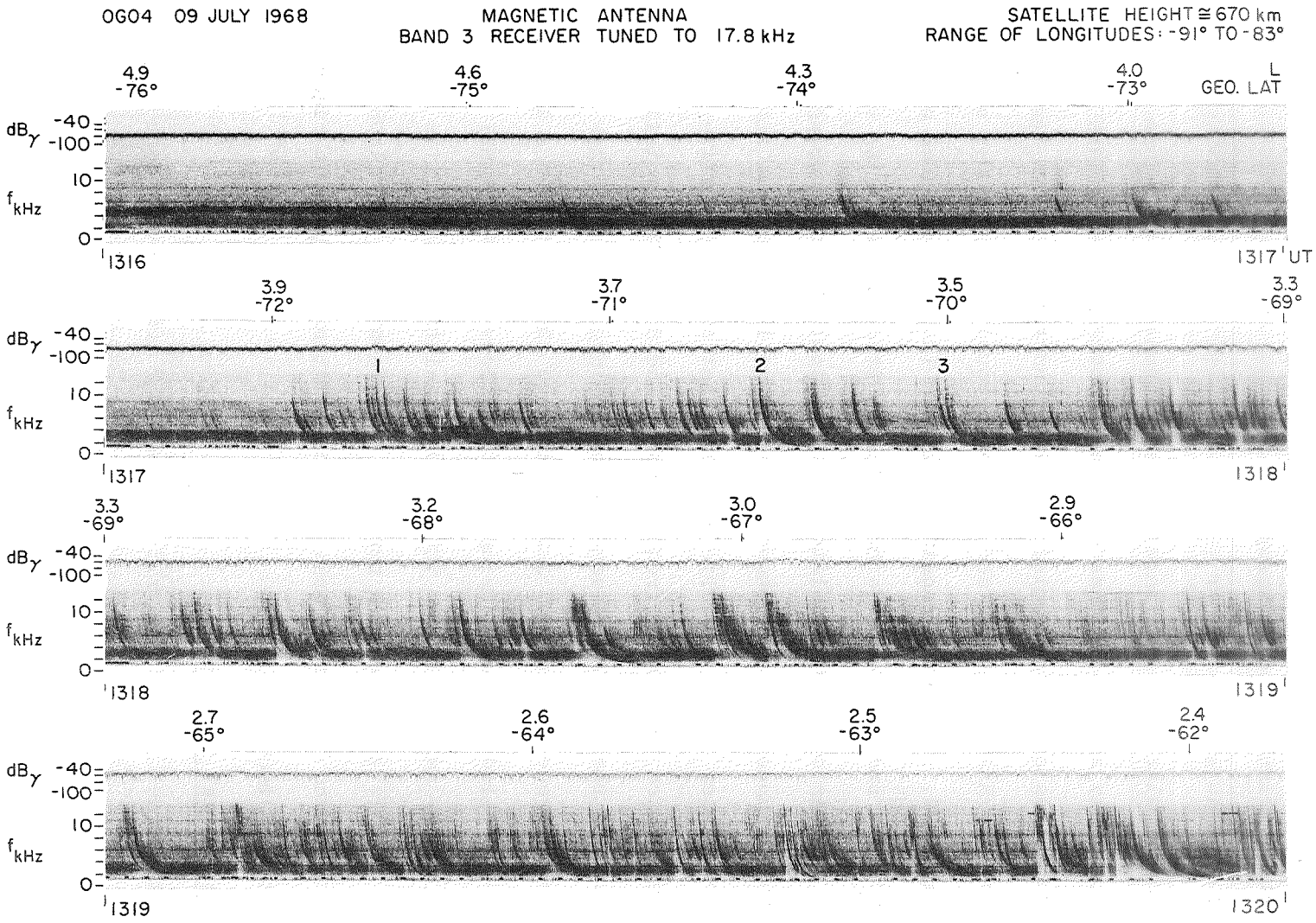

Figure 34. OGO-4 record displaying the high-latitude "erosion" phenomenon. A frequency-time spectrum from 0 to 12.5 kHz and the amplitude of the stepping receiver #3 tuned to 17.8 kHz as seen by the VCO (upper trace) are shown.

hemisphere. These signals reach the satellite from below, after traveling in the ground-ionosphere waveguide from the transmitter to the foot of the ray trajectory connecting the low ionosphere to the satellite. The signal is maximum when the satellite is nearly east of the transmitter.

5. Rings of Noise in the Auroral Region

In every revolution of OGO 4 the auroral oval noise (AON) is detected in the 50 Hz bandwidth of the phase tracking receiver when the satellite crosses the polar regions. The same ring of noise is crossed twice at each high-latitude pass. The AON measured in the conjugate hemisphere of NAA (panels A-B or E-F) does not interfere with the amplitude measurement of NAA signals. This is due to the occurrence of AON above the latitudes where a complete erosion of the NAA signal has already taken place in the conjugate hemisphere. On the contrary, the AON measured in the transmitter hemisphere (panel C-D) seems to be related to a high attenuation in the upgoing waves. In this case the NAA signal may disappear below the noise level but it returns when the satellite is over the polar region. This phenomenon has been reported by Heyborne et al. [1969].

B. DAYTIME MEASUREMENTS

The magnetic field of signals transmitted by mid-latitude VLF stations and received aboard OGO 4 on the dayside presents the same nighttime features discussed above with two main exceptions: signal level and equatorial behavior. First, the signal levels are of the order of 30 db weaker than the nighttime levels (see, for example, Figure 2 in Chapter 1). Second, propagation near the equator is not dominated by defocusing as on the nightside but rather by absorption in the lower ionosphere as

discussed in Chapter 3. For a situation like the one exemplified in Figure 33 where both satellite and transmitter are on the nightside of the earth the signal levels for the other half dayside orbit are very small. For example, the signals from a powerful 1 Megawatt transmitter like NAA are barely detectable. A better situation occurs when satellite and transmitter are on the dayside of the earth. In this case intermerdiate signal levels are measured on the dayside because of transmitter proximity. Intermediate levels are also found on the nightside caused by a combination of increased earth waveguide attenuation followed by high transmission coefficients in the nightside ionosphere. With the exception of the conjugate polar region, it is then possible to observe complete world coverage of VLF reception aboard OGO 4 for a station such as NAA. One example of world coverage with NAA is given in Figures 35a, b, c. These figures show about 175 minutes of stored data corresponding to almost two OGO-4 revolutions on 19 November 1967 as indicated by the ground projection of the satellite trajectory in Figure 36. The stepping receivers B1, B2, and B3 were operating in the sweeping mode and the phase tracking receiver (P and A) was tuned to 17.8 kHz. B1, B2, and B3 present the characteristics already discussed in Chapter 1, Section D, therefore we concentrate here on the features displayed by amplitude A of NAA. The satellite orbit was nearly in the dawn-dusk meridian: It was early evening at the equatorial crossings near Australia (local time $\sim$ 19.3) and early morning at the equatorial crossings over South America (local time $\sim$ 7.3). This fact yields interesting properties related to the trajectory of the waves received by OGO 4 and the corresponding D region absorption taking place just after the waves entered the ionosphere. For example, Figures 35a and 35c show that reasonable

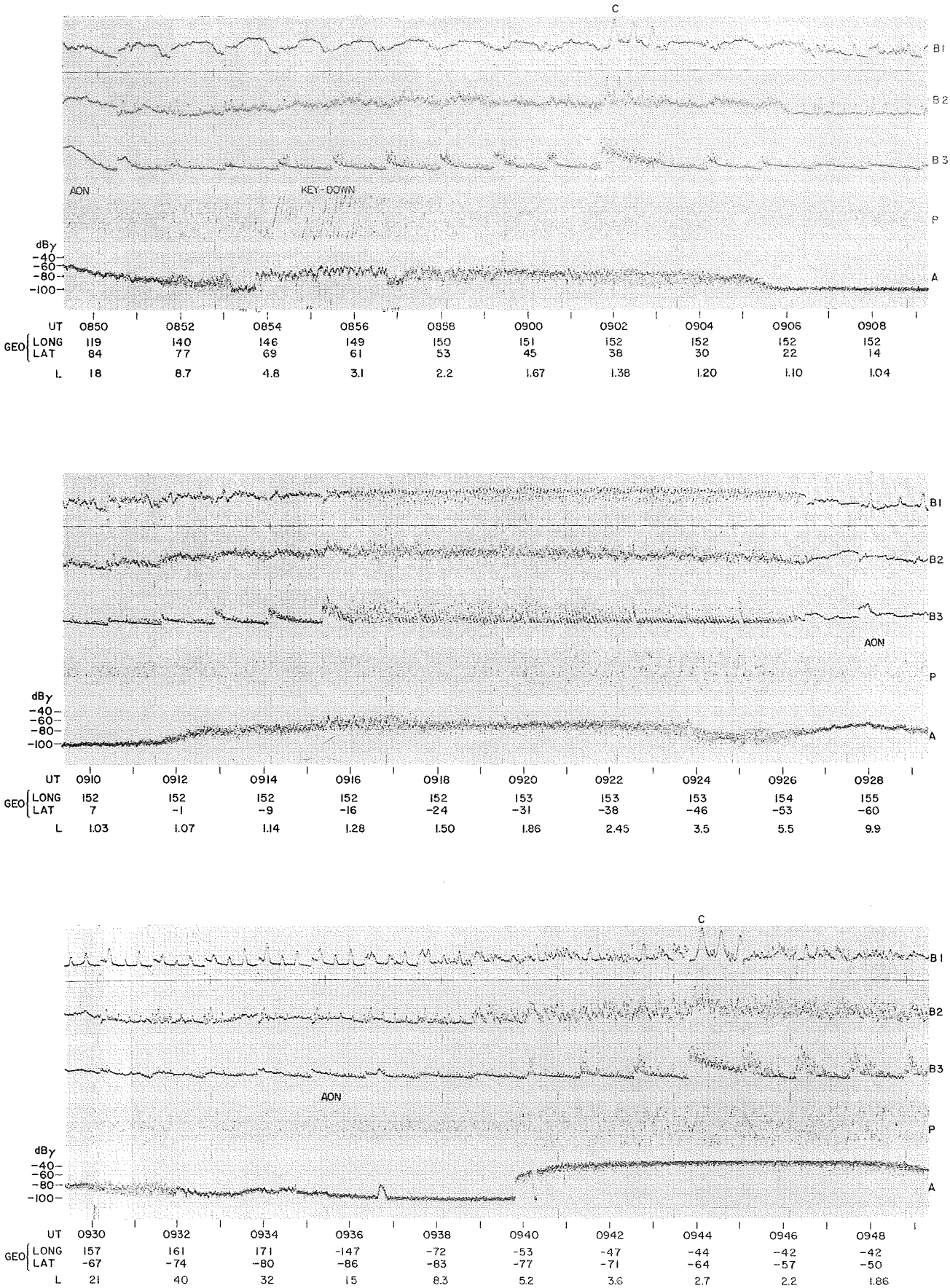

Figure 35a. OGO-4 strip-chart recorded on 19 November 1967. B1, B2, B3, P and A are, respectively, the amplitudes of the stepping receivers operating in sweep mode and phase and amplitude of the phase tracking receiver, tuned to NAA at 17.8 kHz. There is an interruption in the 73.6 sec sweep between 0916 and 0926 UT commanded by the telemetry station at Orroral, Australia.

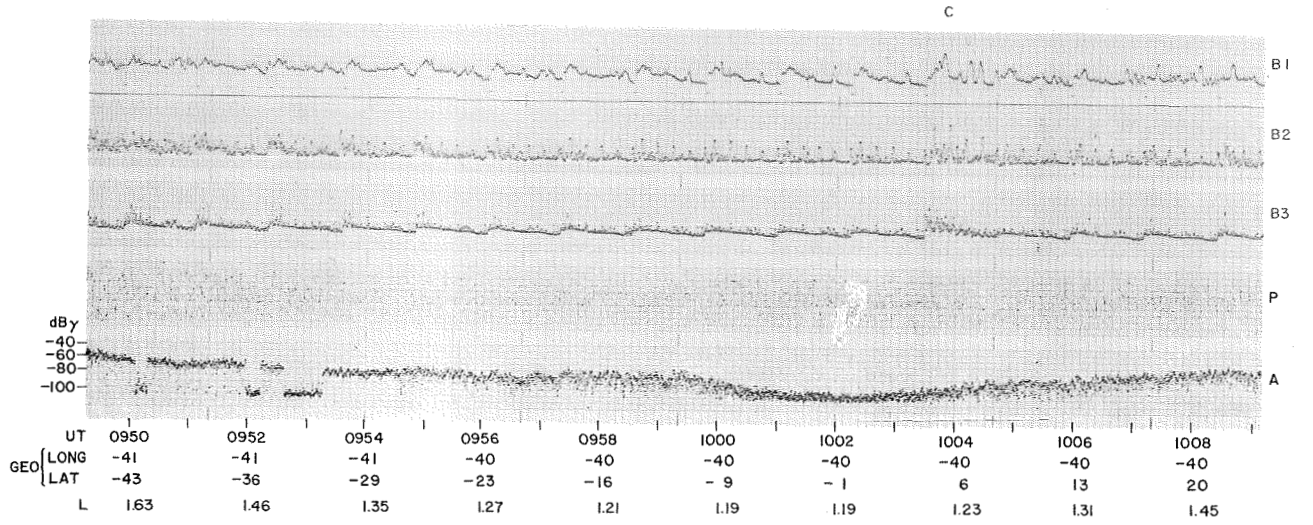

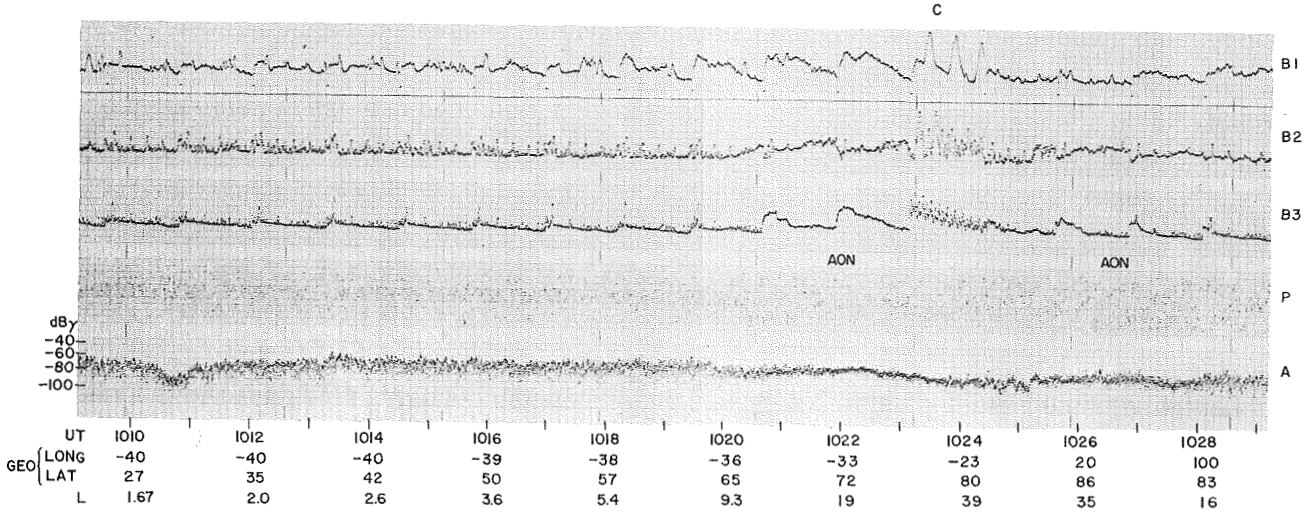

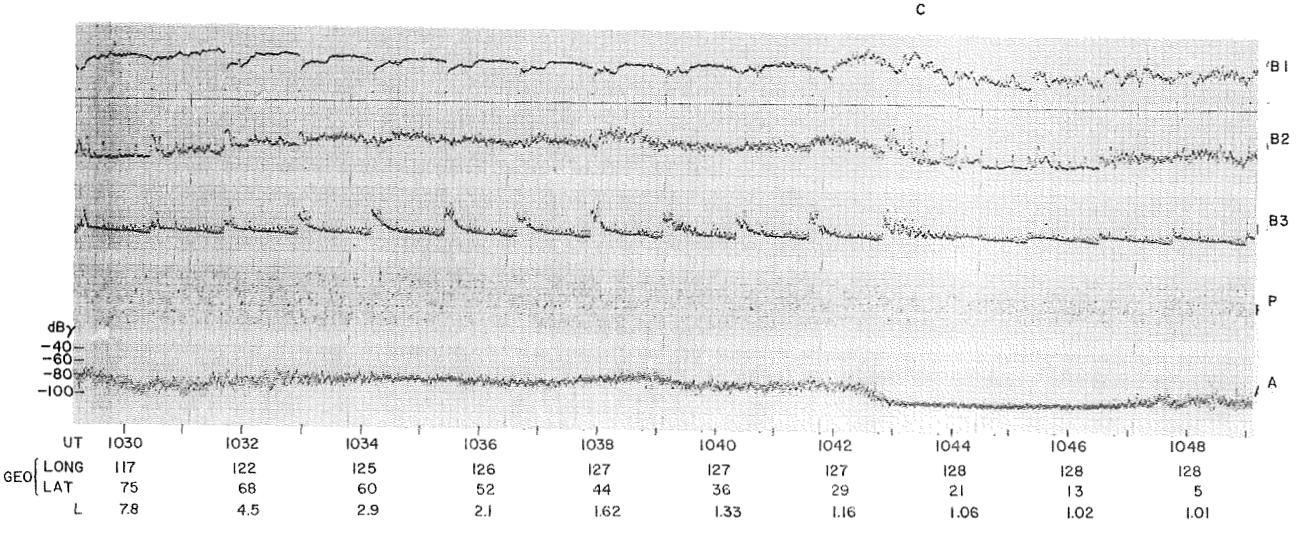

Figure 35b. Continuation of the strip-chart shown in Figure 35a.

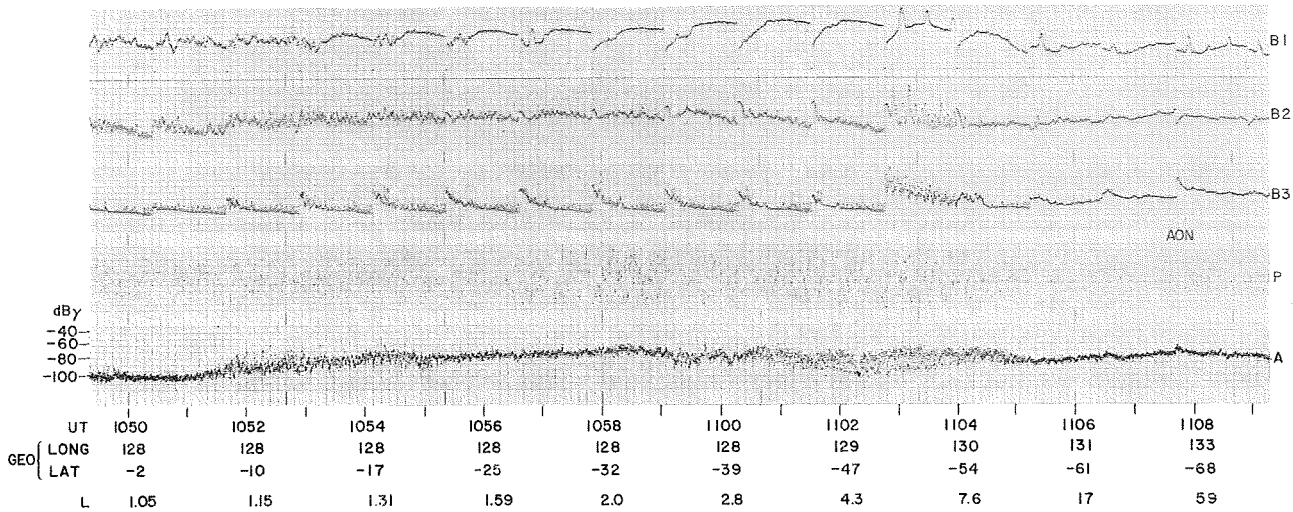

UT	1050	1052	1054	1056	1058	1100	1102	1104	1106	1108
GEO LONG	128	128	128	128	128	128	129	130	131	133
GEO LAT	-2	-10	-17	-25	-32	-39	-47	-54	-61	-68
L	1.05	1.15	1.31	1.59	2.0	2.8	4.3	7.6	17	59

UT	1110	1112	1114	1116	1118	1120	1122	1124	1126	1128
GEO LONG	137	149	-158	-92	-76	-71	-68	-67	-66	-66
GEO LAT	-75	-81	-86	-83	-76	-70	-63	-56	-49	-42
L	∞	57	17	8.3	5.0	3.4	2.5	2.0	1.71	1.50

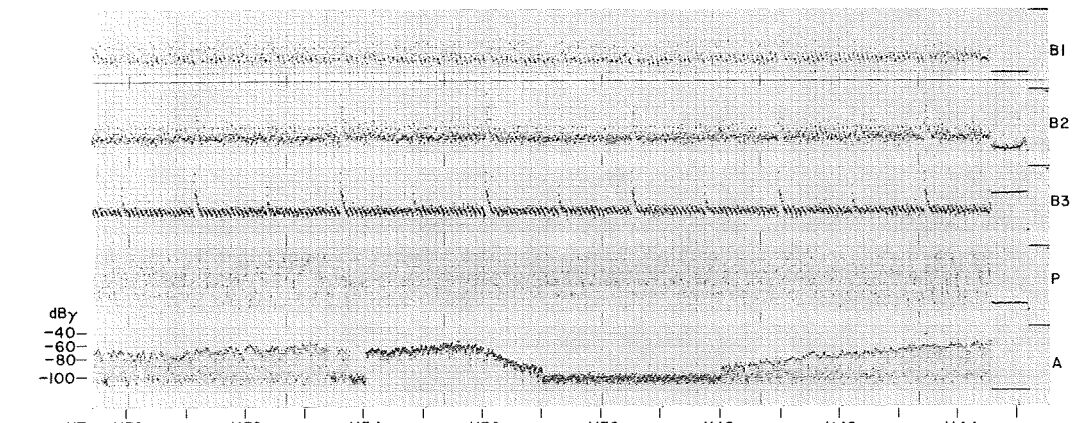

UT	1130	1132	1134	1136	1138	1140	1142	1144
GEO LONG	-65	-65	-65	-65	-65	-65	-65	-65
GEO LAT	-35	-29	-22	-15	-8	0	7	14
L	1.36	1.26	1.21	1.18	1.19	1.23	1.32	1.45

Figure 35c. Continuation of the strip-chart shown in Figure 35b. There is an interruption in the 73.6 sec sweep after 1125 UT commanded by the telemetry station at Santiago, Chile.

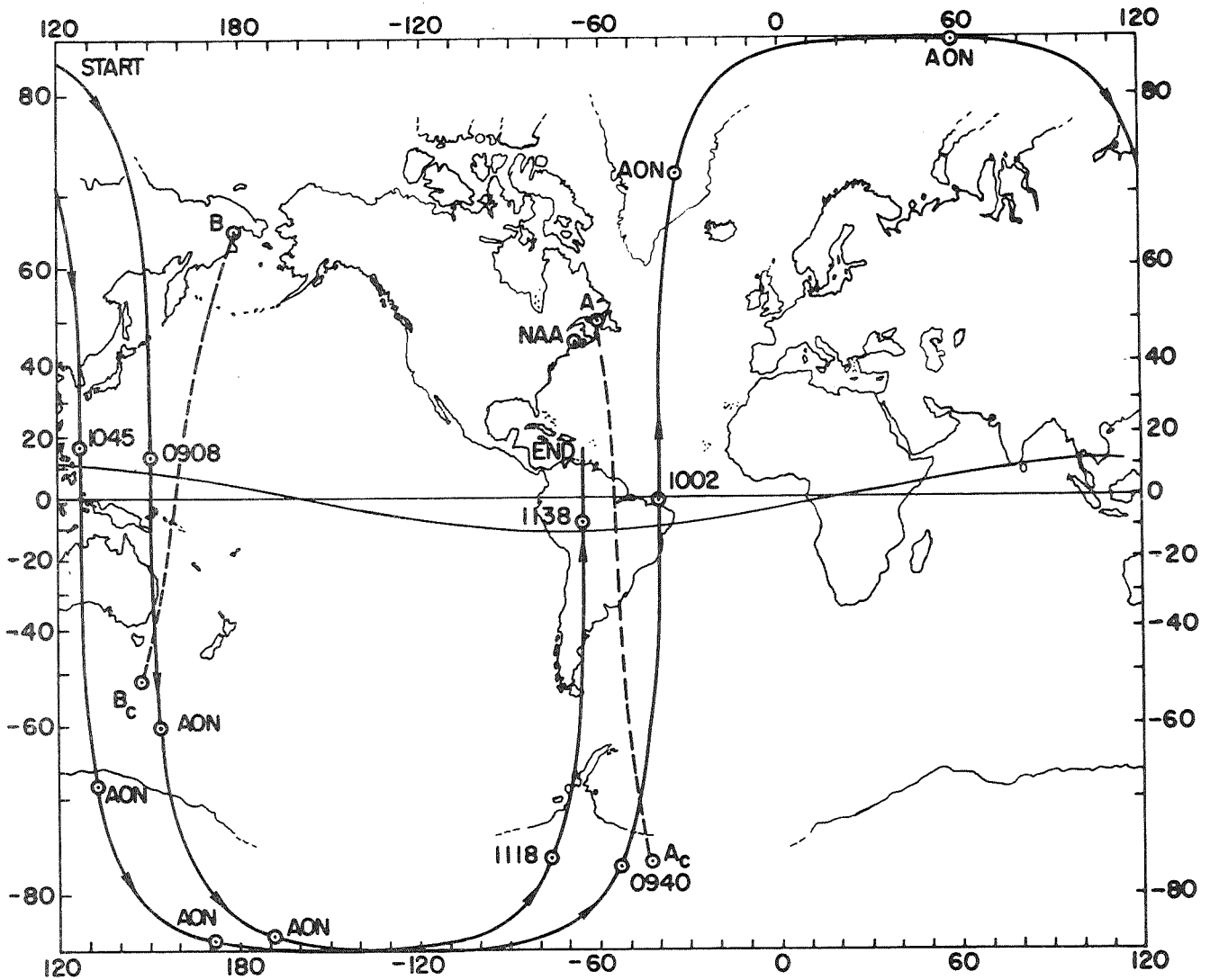

Figure 36. Ground projection of satellite trajectory for Figures 35a,b,c. A-Ac and B-Bc are two field line projections.

field levels are measured in the southern hemisphere, south of Australia, in the two consecutive revolutions, between 0912 and 0924 UT and between 1052 and 1105 UT. The zenith angle of the sun at 0925 UT and at 1105 UT was $\sim 88^{o}$ at the satellite trajectory, indicating daylight. However the signal was coming from above after traveling along a meridian whose conjugate region was in the nightside as shown by the field line projection $B\text{-}B_c$ in Figure 36. Therefore, the signals received in these southern regions (almost in the antipodal region of NAA) reach the satellite after traveling in the nightside ground-ionosphere wave guide from Cutler, Maine to west of Alaska, before being launched into the whistler medium around point B. This is not the only possible trajectory but it is the one that gives minimum total attenuation.

Figures 35a and 35c show also that the signal from NAA saturates the receiver during the two passes (between 0940 to 0948 UT and 1118 to 1124 UT) in the southern hemisphere over South America. Here again it was sunlight in the above southern regions but in both cases the satellite was receiving signals from a region near NAA where it was nighttime as shown in Figure 36 by the field line projection $A\text{-}A_c$. The zenith angle of the sun was 111^{o} at point A at 0945 UT and 101^{o} at the entry point (LAT = 50^{o}, LONG = -70^{o}) from where the satellite was receiving signals at 1120 UT.

The NAA signal is not received in the polar regions of the southern hemisphere as shown in Figure 35. We observe world coverage of NAA signals with this one exception.

C. SIGNALS IN THE CONJUGATE HEMISPHERE

From the properties discussed in the previous sections relative to

magnetic field measurements of VLF transmitters, we now concentrate on the features that occur in the conjugate hemisphere of the transmitter (panel A-B or E-F of Figure 32). It is proposed to interpret these measurements and to discuss their implications. To be more specific, the first step will be to deduce the properties the medium must present for the purpose of matching the requirements imposed by the measurements. Next, the deduced properties of the medium will be applied to the analysis of whistler propagation in the magnetosphere. It will be shown that a simple interpretation of the amplitude measurements in the conjugate hemisphere of the transmitter will predict concomitantly several features for the whistlers commonly received aboard the same satellite. This provides proof of the new theory of VLF propagation in the magnetosphere.

Theoretical discussion. The measurements of Figure 32 for the conjugate hemisphere of the transmitter put the following constraints on the ray-wave properties received aboard the satellite:

1. Possible Doppler shift must be confined to ±25 Hz because differences in amplitude have not been observed when the same VLF transmitter is tuned simultaneously by the stepping receiver No. 3 and the phase tracking receiver, whose bandwidths are ±250 and ±25 Hz respectively. For the orbital velocity of OGO 4 the above condition implies that the horizontal component of the refractive index at the satellite must be below 57.

2. The propagation cannot be along ducts of enhanced ionization because a cutoff should then occur for the duct whose minimum gyrofrequency is 2×17.8 kHz [Smith, 1961a]. Hence, the maximum latitude where the downcoming signal could be observed is $\sim 54^{\circ}$ ($L \cong 2.9$). The measurements indicate that the VLF signals are received aboard the satellite at much higher latitudes in the conjugate hemisphere.

3. Ray tracjectories in a latitudinally smooth ionosphere produce

downcoming waves in the conjugate hemisphere whose main characteristics are: very large angle between the wave normal and the earth's magnetic field (large refractive index) plus a maximum latitude range of about 48^{o}. This corresponds to the "walking-trace" mode of propagation discussed by Walter and Angerami [1969]. The measurements displayed in Figure 32 rule out the walking-trace mode, because of a latitude range of observations and a refractive index at the satellite necessarily smaller than about 57.

From the above discussion is is concluded that the waves probably cross the equator at a radius less than 2.9 earth radii. Hence, the upgoing rays starting from below the ionosphere at high latitudes must migrate to lower L-shells, cross the equator below 2.9 earth radii, and follow a descending path toward higher L values in the conjugate hemisphere. In order to achieve the above ray behavior it is necessary to deflect the upgoing wave normal toward the equator. This equatorward orientation of the wave normal is accomplished by introducing a negative latitudinal gradient of electron density in the ionosphere at mid-high latitudes. In fact, this kind of ionization gradient exists and has been detected systematically at the orbiting altitudes of satellites Tiros 7, Explorer 22, and Alouette 1, and Alouette 2 (see for example, Brace et al. [1967]; Reddy et al. [1967]). The effect of these horizontal gradients of ionization on the behavior of the wave normal has been discussed by Aubry [1967] for upgoing rays just after the waves entered the ionosphere.

In order to introduce the need for a latitudinal gradient of electron density the following study of wave-normal behavior is made. The differential equations governing the propagation of waves in a slowly varying two-dimensional ionosphere may be expressed by a closed set

$$\frac{dr}{dt}, \quad \frac{d\theta}{dt} \quad \text{and} \quad \frac{d\psi}{dt}$$

where r and θ are respectively the radius and the colatitude of the ray trajectory, and ψ is the angle between the wave normal and the earth's magnetic field. These equations describe the ray path of a wave packet in the magnetosphere as a function of time t, and can be numerically integrated by means of standard computer procedures. These equations have been written in this form by Walter [1969] who showed that when electrons only are considered the equation for ψ is

$$\frac{d\psi}{cdt} = -\frac{1}{\mu^2}\left\{\sin\delta\left[\frac{\partial\mu}{\partial X}\cdot\frac{\partial X}{\partial r}+\frac{\partial\mu}{\partial Y}\cdot\frac{\partial Y}{\partial r}\right]-\frac{\cos\delta}{r}\left[\frac{\partial\mu}{\partial X}\cdot\frac{\partial X}{\partial\theta}+\frac{\partial\mu}{\partial Y}\cdot\frac{\partial Y}{\partial\theta}\right]\right\} - \frac{3\sin\delta}{\mu r}\cdot\frac{(\cos^2\theta+1)}{(3\cos^2\theta+1)} \qquad (4.1)$$

where μ is the refractive index

$X = (f_N/f)^2$ and f_N is the local plasma frequency

$Y = f_H/f$ where f_H is the local gyrofrequency

f is the wave frequency

c is the velocity of light

and δ is the angle between the local vertical and the wave normal. The geometry is shown in Figure 37. For very-low-frequencies and when only the motion of electrons is taken into account the refractive index is approximately given by

$$\mu^2 \cong \frac{X}{(YC-1)} \qquad (4.2)$$

where $C = \cos\psi$ (see, for example, Helliwell [1965]).

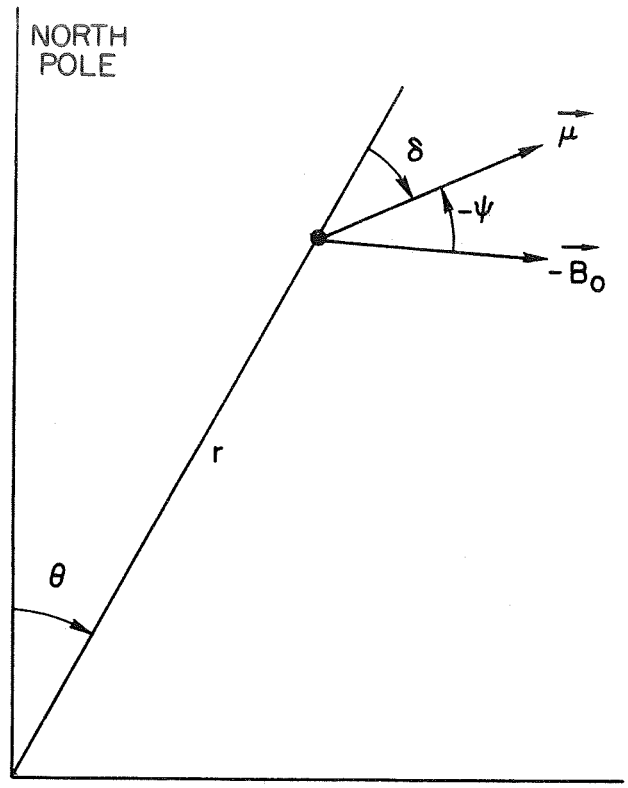

Figure 37. Geometry assumed for the two-dimensional ray equation, Eq. (4.1).

There are several approximations in Eq. (4.2), namely $X \gg 1$, Q.L. approximation [Ratcliffe, 1959], $\mu^2 \gg 1$, and finally

$$\frac{f_H}{f_N} \sin\psi \ll \sqrt{2} \ .$$

Of all the approximations the last one fails when ψ is near the resonance cone for a wide range of heights in the magnetosphere. The resonance cone is defined by the angle ψ for which $\mu^2 = \infty$. In general the Q.L. approximation is good for all magnetospheric conditions,

including ψ at the resonance cone. On the other hand we assume that the earth's magnetic field comes from a centered dipole, i.e.,

$$Y = Y_o \left(\frac{r_o}{r} \right)^3 \sqrt{1 + 3 \cos^2\theta} \tag{4.3}$$

where r_o is the earth's radius and Y_o corresponds to the equatorial gyrofrequency on the ground. Using Eq. (4.2) and Eq. (4.3) and noting that f_N^2 is proportional to the electron density N, Eq. (4.1) may be written as

$$2\mu \frac{d\psi}{cdt} = - \sin\delta \left\{ \frac{\partial}{\partial r} \log N + \frac{3}{r} (m_c + m_y) \right\} + \frac{\cos\delta}{r} \left\{ \frac{\partial}{\partial\theta} \log N + m_\theta \right\} \tag{4.4}$$

where the influence of the curvature of the earth's magnetic field is given by

$$m_c = \frac{2(1+\cos^2\theta)}{(1+3\cos^2\theta)} \tag{4.5}$$

and the influence of the magnetic field over the wave normal is dependent upon the angle ψ between the wave normal and the magnetic field, namely

$$m_y = \frac{YC}{YC-1} \tag{4.6}$$

$$m_\theta = \frac{3\sin\theta \cos\theta}{(1+3\cos^2\theta)} \cdot m_y \tag{4.7}$$

In Eq. (4.4) logN stands for the natural logarithm of N.

Assume for the moment that N does not vary in latitude and that N decreases with height as it does above the peak of the F region.

Therefore, Eq. (4.4) gives

$$2\mu \frac{d\psi}{cdt} = \sin\delta \left| \frac{\partial}{\partial r} \log N \right| + \frac{\cos\delta}{r} \cdot m_\theta - \frac{3\sin\delta}{r} (m_c + m_y) \qquad (4.8)$$

The first two terms in Eq. (4.8) provide positive values for the derivative of ψ (bending toward the equator) while the last term introduces negative values for $d\psi/dt$. The waves that emerge from the E region of the ionosphere have an almost vertical wave normal ($\delta = 0$), a result provided by the application of Snell's law to the lower ionosphere. Therefore, the only term that will produce some equatorward deflection at the starting heights will be m_θ. This effect will in turn cause δ to be different from zero and then the other terms in Eq. (4.8) become effective as the ray proceeds upward.

Observe that m_θ decreases as the ray approaches the equator and is much smaller than the other magnetic terms for (say) $\pm 10^o$ near the equator. At these latitudes critical conditions occur:

1. If in Eq. (4.8) the term involving the radial derivative of N is of the order of the term involving $(m_c + m_y)$ then the ray may cross the equator with not very large ψ and may continue traveling downward with reasonable angles ψ between the wave normal and the magnetic field.

2. If the term involving the radial derivative of N is smaller than the one involving $(m_c + m_y)$ a degeneration may happen namely that ψ increases negatively and the product YC may approach unity. This in turn increases the difference further between the terms in Eq. (4.8) until the wave normal is attached to the resonance cone with a very large refractive index. It can be shown that from this point on the ray will follow closely a line of force and will arrive at the conjugate hemisphere with very large refractive index [Walter and Angerami, 1969].

Now we ask what would be the scale height of the electron density that would overcome the above degenerating effect. Suppose the electron density is given by a hydrostatic-equilibrium distribution [Angerami and Thomas, 1964] and that at high altitudes only hydrogen ions and electrons exist. Then, the electron density is given by

$$N = N_r \exp \left\{ - \frac{r_r}{2H} \left(1 - \frac{r_r}{r} \right) \right\} \tag{4.9}$$

where N_r is the electron density taken at a reference radius r_r and H is the neutral scale height of hydrogen. If Eq. (4.9) is now substituted into Eq. (4.8) and the condition imposed that $\frac{d\Psi}{dt}$ is nearly zero around equatorial latitudes, we get

$$\begin{aligned} H &\cong 200 \text{ km at } r = 2 \text{ earth radii} \\ H &\cong 160 \text{ km at } r = 2.5 \text{ earth radii} \end{aligned} \tag{4.10}$$

The reference level has been assumed to correspond to a height of 400 km. The neutral scale-height values for hydrogen generally measured above 1000 km are of the order of or greater than 1000 km and therefore the values given by Eq. (4.10) are unrealistic. Therefore, certainly the term involving N in Eq. (4.8) will lose control of Ψ to the magnetic terms around the equator because the real scale height is certainly much greater than the values displayed in Eq. (4.10). Hence, it is conclusive that $\frac{d\Psi}{dt}$ will be negative in a region around the equator and this situation cannot be changed. Nevertheless Ψ can be conveniently shaped outside the equatorial region in such a way that the ray entering the equatorial region may cross it and emerge from the other

side before the degeneration takes place, i.e., before the wave normal gets attached to the resonance cone. The idea is then to introduce convenient gradients of ionization in order to get $\frac{d\psi}{dt} > 0$ at the L shells where presumably the ray trajectory will take place and outside the equatorial region. Equation (4.4) shows that a negative latitudinal gradient of electron density would work in the desired direction starting from the beginning of the ray path. Therefore, this gradient of electron density would bend the wave normal to positive values of ψ, the ray would migrate to lower L shells, and penetrate the degenerating region with positive ψ values. The ray may come from the degenerating region with negative ψ values (as it usually does) but for a symmetric magnetosphere $\frac{d\psi}{dt}$ will again be positive in the conjugate hemisphere and then reasonable values of ψ may be achieved in the downward ray flow. These ideas are expressed by the ray trajectories of Figure 38. In Figure 38 a ray-tracing computer program [Walter, 1969] has been used in order to obtain the behavior of 17.8 kHz rays that start at the same latitude for two different magnetospheres: one with no latitudinal variation of electron density ($N_\theta = 0$) and one presenting a latitudinal gradient of electrons toward the equator ($N_\theta \neq 0$). Both models of electron density are of the hydrostatic-equilibrium type and the details for the model having $N_\theta \neq 0$ will be given in Section D of this chapter. The wave normal to magnetic field angle ψ is negative for the $N_\theta = 0$ model, and the ray degenerates in the walking-trace mode of propagation presenting a refractive index of 1200 and a delay of 3.6 seconds at the arrival height of 500 km in the conjugate hemisphere. To the contrary, the ray that travels inside the medium presenting $N_\theta \neq 0$ has the wave normal rapidly bent toward the equator at low heights. The ray migrates

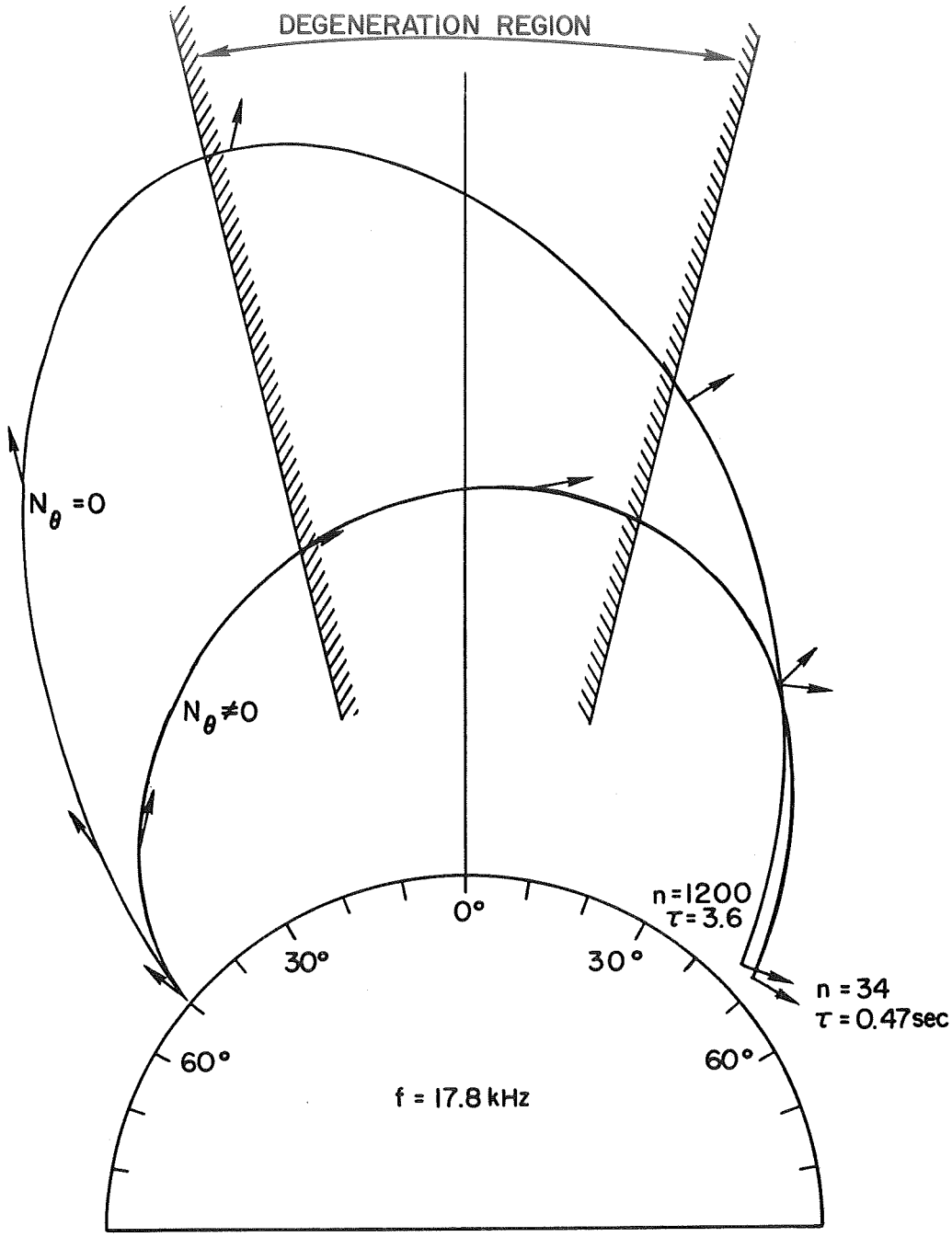

Figure 38. Ray trajectories in a latitudinally constant magnetosphere ($N_\theta = 0$) and in a magnetosphere presenting an increasing trend of ionization toward the equator ($N_\theta \neq 0$).

to lower L shells and is launched inside the degeneration region with positive ψ value. Inside the degeneration region $d\psi/dt$ becomes negative driving ψ to negative values. However, the gradient of electron density across the field lines restrains the negative variation of ψ and the ray arrives approximately at the conjugate point from where it started. The important fact is that although this ray arrives at 500 km with ψ of the order of 80^{o} the refractive index is relatively small ($\mu = 34$) and the delay is 0.47 second (a typical travel time for longitudinal propagation).

The satellite VLF reception at high latitudes in the conjugate hemisphere of the transmitter is interpreted as the result of effects upon the ray trajectories caused by electron density gradients across magnetic field lines in the ionosphere. A numerical study follows in order to analyze the predictions by a computer ray-tracing program when rays are allowed to travel in a realistic latitudinally variable magnetospheric model.

D. PROPAGATION IN A MODEL MAGNETOSPHERE

Electron density measurements in the upper ionosphere have shown that the ionization at a constant height is highly variable in latitude. More than that, topside sounders Alouette 1 and 2 have shown that the general latitudinal trend of ionization observed at a specific height is also observed at all heights above the F region and below the satellites. Nighttime features of the ionosphere include a flat profile of ionization around the equator, a peak at mid latitudes, a decrease toward high latitudes, a high-latitude trough and an irregular behavior at polar latitudes [Reddy et al, 1967]. A model magnetosphere will be

derived having the above features and satisfying the equations of diffusive equilibrium along the magnetic field lines. No claim will be made that the derived model has the actual properties of a global magnetosphere, but the model will carry the features generally found at nighttime below 2500 km.

First we start with a diffusive equilibrium model whose composition includes hydrogen and oxygen ions. For a constant temperature along the field line the electron density is (see Angerami and Thomas [1964])

$$N = N_r \sqrt{a_{O^+} + a_{H^+}} \tag{4.11}$$

where

$$a_{O^+} = \xi_{O^+} \cdot e^{-z/H_O} \tag{4.12}$$

$$a_{H^+} = \xi_{H^+} \cdot e^{-z/H_H} \tag{4.13}$$

and

$$z = r_r(1 - r_r/r) \tag{4.14}$$

N_r is the electron density at a reference level radius r_r; ξ_{O^+} and ξ_{H^+} are respectively the oxygen and the hydrogen ion percentages at r_r; r is the geocentric radius, and H_O and H_H are respectively the neutral scale heights of oxygen and hydrogen. The reference level is taken as 400 km, i.e.,

$$r_r = (400 + 6372) \text{ km} \tag{4.15}$$

The E, F regions of the ionosphere are simulated by a gaussian distribution that matches the ionization and the vertical gradients of

ionization of the above diffusive-equilibrium model at a height below 400 km and has a given value of electron density at 100 km. Therefore, a complete description of electron distribution above 100 km is derived. Very good agreement between calculated models and Alouette profile measurements is easily obtained by using the present technique.

Next, the derived model is modulated as a function of latitude, i.e.,

$$N_r = N_r(\theta_0) \tag{4.16}$$

$$H_H = 16\, H_O = H(\theta_0) \tag{4.17}$$

where θ_0 is the colatitude at ground level. The fact that the hydrogen scale height is 16 times greater than the oxygen scale height has been used. Observe that N_r and H depend on r and θ because the distribution is along the field lines:

$$\frac{1}{\sin^2\theta_0} = L_0 = \frac{r}{r_0} \cdot \frac{1}{\sin^2\theta} \tag{4.18}$$

This means given a point (r,θ) in the magnetosphere it is necessary to use the relation, Eq. (4.18), to obtain the colatitude θ_0 of the foot of the field line passing through (r,θ). Now N_r and H can be calculated. The geometry is shown in Figure 39. It is easily seen that

$$N = N(r,\theta_0) \tag{4.19}$$

$$\frac{\partial N}{\partial r} = \frac{\partial N(r,\theta_0)}{\partial r} - \frac{\partial N(r,\theta_0)}{\partial \theta_0} \cdot \frac{1}{2r(L_0-1)^{1/2}} \tag{4.20}$$

$$\frac{\partial N}{\partial \theta} = \frac{1}{(L_o-1)^{1/2}\tan\theta} \cdot \frac{\partial N(r,\theta_o)}{\partial \theta_o} \qquad (4.21)$$

so that a variable density across lines of force produces both radial and latitudinal derivatives in the diffusive equilibrium model.

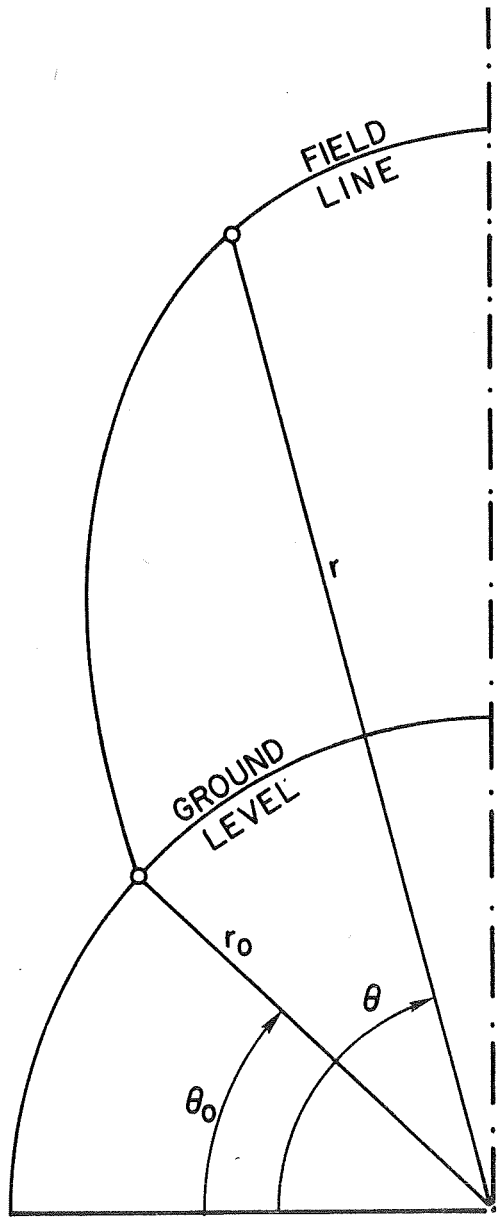

Figure 39. Geometry for developing the equations of ionization oriented along the field lines.

One of the models tested has the electron density distribution at 1000 km as shown in Figure 40. The basic electron-density profile for obtaining the latitudinal variation of Figure 40 is an equatorial model having an ionic composition given by

$$\xi_{O^+} = 0.96, \quad \xi_{H^+} = 0.04$$

at the base height of 400 km. The equatorial hydrogen scale height is $H_{eq} = 850$ km, corresponding approximately to a temperature of 1000 ^{o}K. This basic equatorial model simulates typical equatorial profiles taken at nighttime by Alouette 1. The equatorial model is modulated as a function of latitude presenting a gaussian overshoot of ionization at the invariant latitude $\phi_O = 40^{o}$, a decrease toward high latitude, a gaussian trough at $\phi_O = 60^{o}$ and an increase of density above 60^{o}, as shown in Figure 40. The ratio between the densities at 40^{o} and at 60^{o} in Figure 40 agrees with nighttime Alouette measurements and with curves given by Brace et al. [1967]. The latitudinal modulations imposed on N_r and H are equal in the present magnetospheric model. This model produces at high altitudes the equatorial profile of Figure 41. The small values of electron density produced by the model above $L_O = 2.5$ are represented by the dashed portion of Figure 41 because they are not relevant in the following discussion.

Figure 42a shows a ray trajectory followed by waves of 17.8 kHz in the magnetospheric model and Figure 42b shows the corresponding behavior of the wave-normal angle ψ as a function of latitude. The figures show an approximately symmetric ray path that crosses the equator at $L_O = 2.2$, coming from (and proceeding to) $L_O \cong 3.6$ at 120 km. Figures

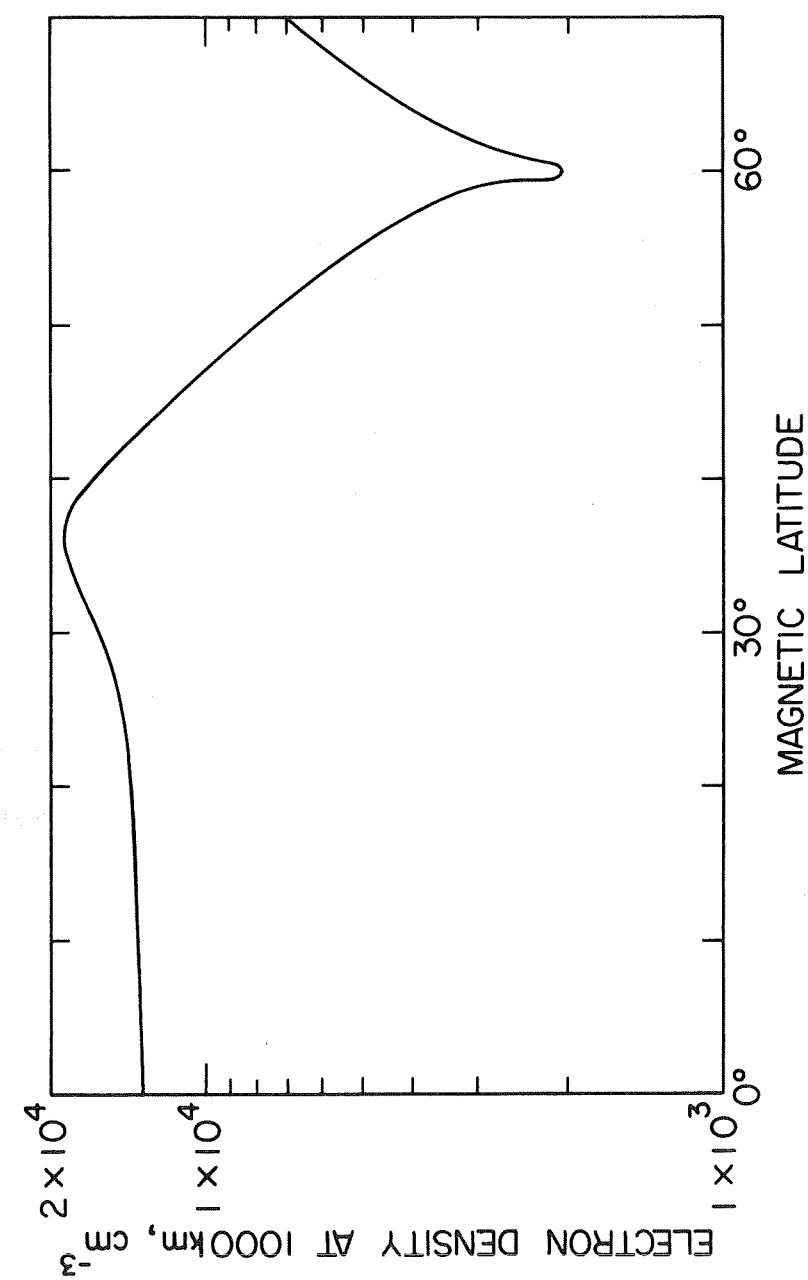

Figure 40. Electron density at 1000 km as a function of latitude for the model magnetosphere.

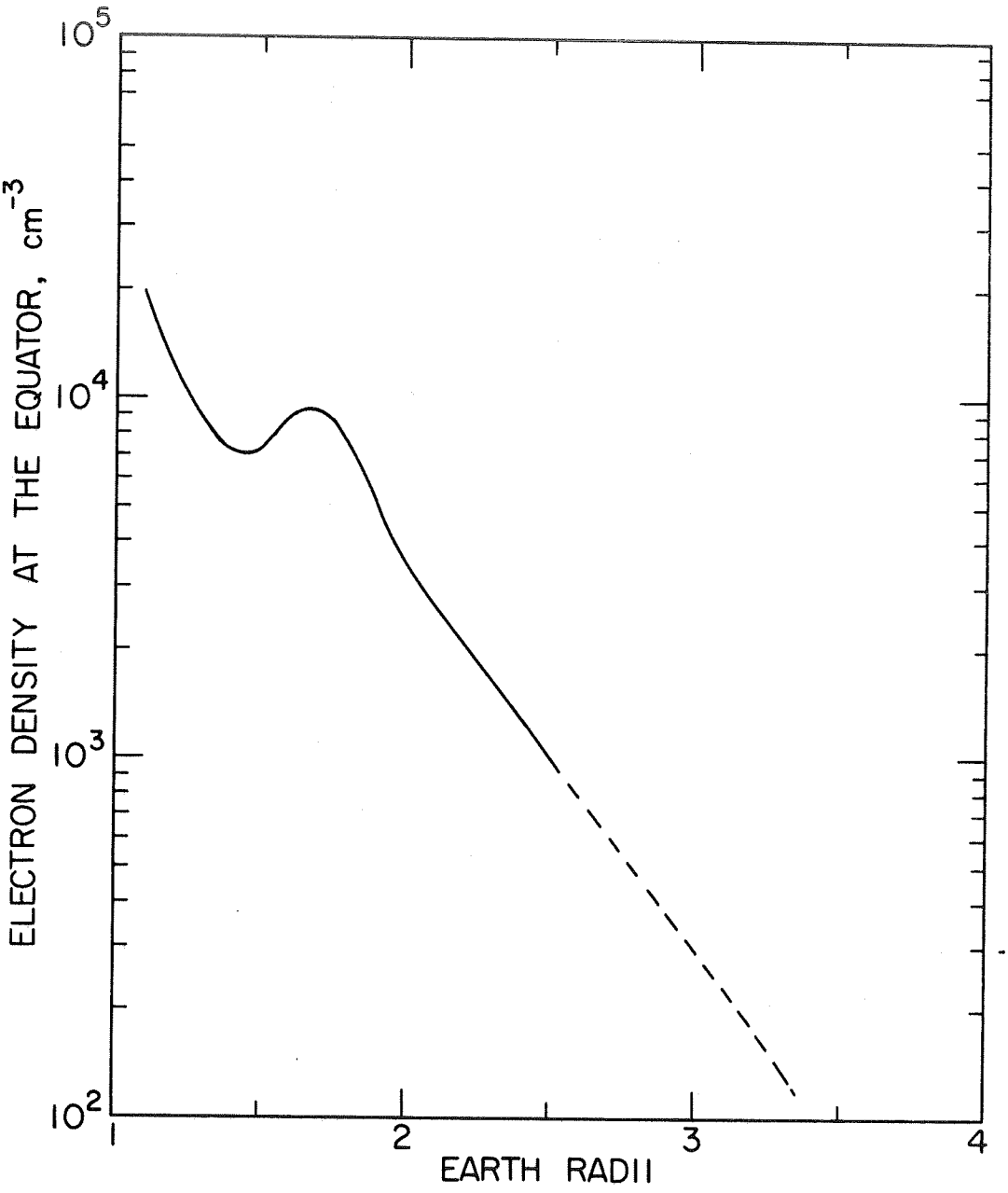

Figure 41. The equatorial ionization profile of the assumed magnetospheric model.

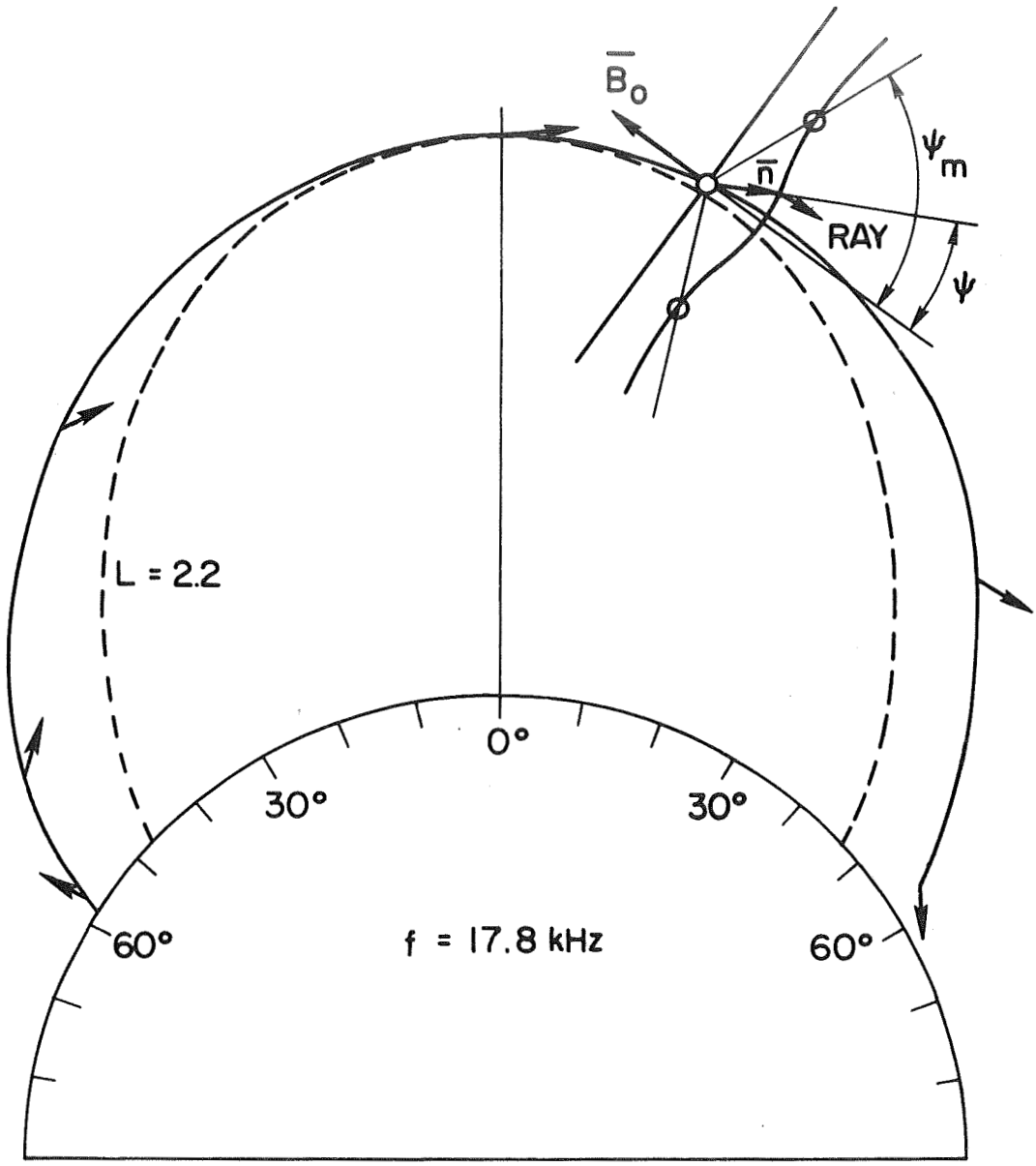

Figure 42a. Ray-trajectory for 17.8 kHz waves that start with vertical wave-normal at 120 km height and at 58^{o} latitude. The magnetospheric model includes the electron distribution of Figures 40 and 41 and a centered dipole for the geomagnetic field whose gyrofrequency at the equator is 870 kHz on the ground level.

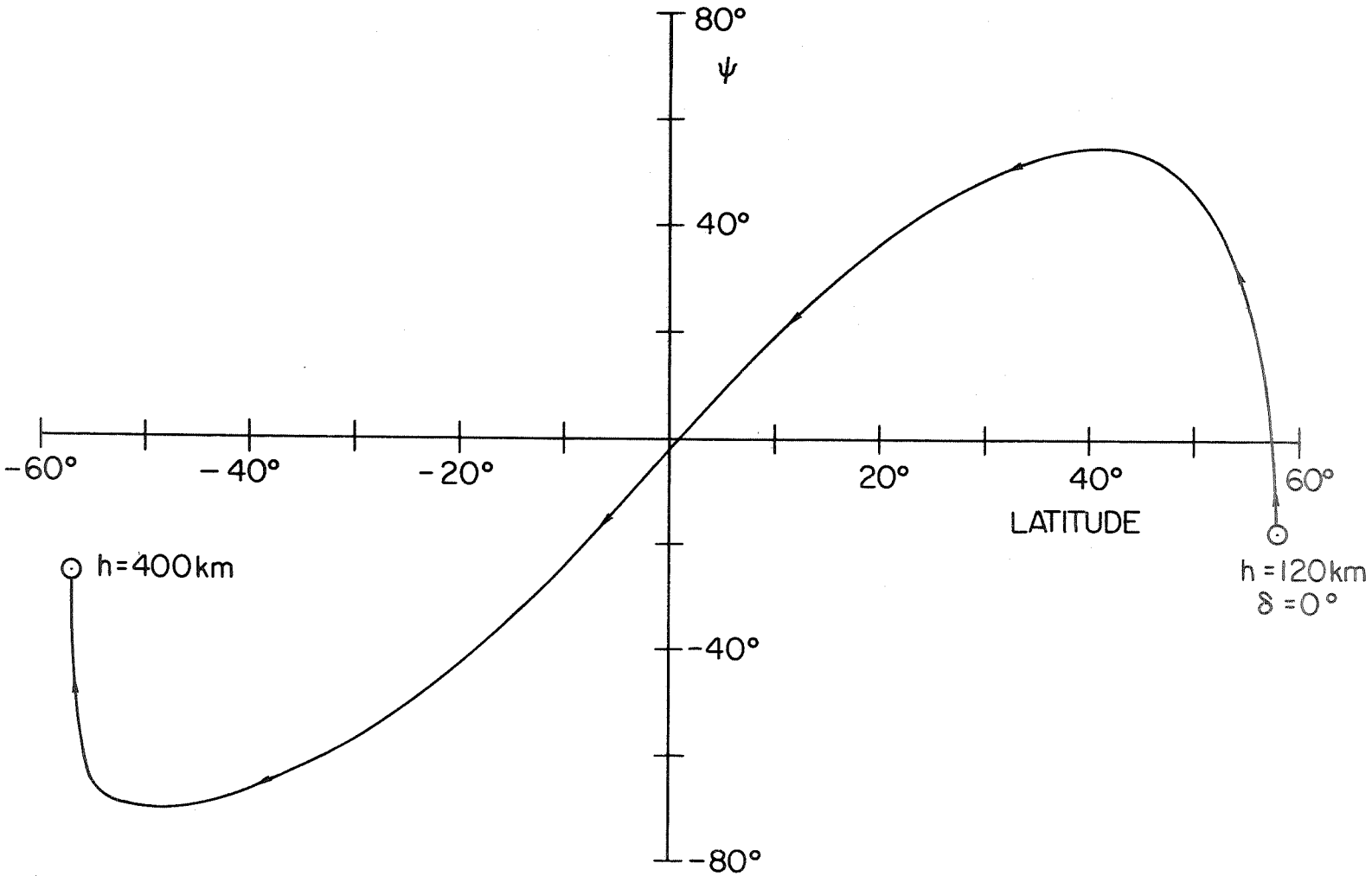

Figure 42b. Latitudinal behavior of the angle ψ between the geomagnetic field and the wave-normal of the 17.8 kHz wave corresponding to the ray path of Figure 42a.

42a,b reproduce all the requirements imposed by the measurements whose properties have been deduced in the last section. Observe, for example $d\psi/dt$ in Figure 42b and the wave normal progression in Figure 42a represented by the direction of arrows placed at some points of the ray trajectory (they follow the pattern predicted previously). Figure 42a also shows the refractive index surface and the geometrical relationship between the refractive index μ and the direction of the ray at an arbitrary point of the ray path in the conjugate hemisphere. This geometrical relationship emphasizes the mechanism by which the ray returns to higher L shells. The refractive index surface of Figure 42a illustrates another very important point, namely that the difference between the walking-trace behavior and "small-dispersion" behavior is characterized by gradients that permit or do not permit the angle $|\psi|$ to become greater than $|\psi_m|$. The angle ψ_m is determined by the angle ψ for which the component of the refractive index vector along the magnetic field is minimum, i.e.,

$$\frac{\partial}{\partial\psi}(\mu\cos\psi) = 0 \qquad (4.22)$$

For the density gradients generally found (N decreases with height) the angles $\pm\psi_m$ separate three distinct regions of ray behavior:

1. If ψ becomes greater than ψ_m at any point of the ray path then ψ will continue to increase toward the resonance cone from this point on. The ray may or may not return to ground. This situation would occur for extremely large latitudinal gradients: the upgoing wave normal would bend rapidly toward the equator, ψ would become greater than ψ_m, and from this point on the ray would travel to high L values with the wave normal attached to the resonance cone. It can be shown that the wave will then suffer a defocusing effect above the height

where the frequency of the wave is greater than half the gyrofrequency. The ray may return to ground if $\psi > \psi_m$ occurs in the downcoming section of the ray path.

2. For $|\psi| < |\psi_m|$ during the whole ray path the downcoming ray may reach theoretically any latitude in the conjugate region. The delay time for the entire path is comparable to calculated delays supposing longitudinal propagation. We define this as the pro-longitudinal mode of propagation (PL-mode) because wave normals inside the cone defined by $|\psi| = |\psi_m|$ produce ray trajectories and/or travel times that are similar to characteristics given by purely longitudinal propagation.

3. If $-\psi$ becomes greater than $-\psi_m$ at any point of the ray path then, again, $-\psi$ will rapidly increase toward the resonance cone and the ray will present the properties of the walking-trace mode of propagation: very large delay time and very large refractive index in a restricted region of observation at mid latitudes (see Walter and Angerami [1969]).

If started with a smooth magnetosphere where gradients of electron density are progressively introduced in the usually observed directions, the walking-trace mode of propagation will be excited first. Above a certain level of gradients, the PL-mode is introduced and it may be observed for a wide range of conditions. Finally for extremely large gradients, which are probably unrealistic for the real magnetosphere, the mode discussed in 1 ($\psi > \psi_m$) will then be excited. The term "gradient" is used here in a broad sense because the gradients of electron density may be completely different at different points of the magnetosphere resulting in complex conditions for exciting the above modes of propagation. In fact some modes of propagation may coexist in a model magnetosphere, depending on the place and the intensity of the electron-density gradients, as well as on the frequency, initial angle between the wave normal and the vertical, and the latitude where the waves start.

We return now to the numerical study of the model magnetosphere which produced the ray behavior of Figures 42a,b. For waves of 17.8 kHz starting at any northern latitude, Figure 43 gives the corresponding arrival latitude at 500 km in the southern hemisphere (left side of Figure 43) as well as the related travel time for these rays (right side of Figure 43). The maximum input latitude of Figure 43 is slightly smaller than 60^{o} which corresponds to the position of the high-latitude trough of Figure 40. Waves starting above 60^{o} are disregarded because they will encounter electron-density gradients which support the walking-trace mode of propagation beginning at low altitudes. Consequently these rays travel to very high altitudes with the wave normal at the resonance cone and therefore with very large refractive index. This implies an enhancement of collisional absorption. The result is that the integrated absorption over a long path is extremely high and these rays are in fact absorbed by the medium.

For input latitudes between 0^{o} and 35^{o} Figure 43 shows that the travel time and the arrival latitude at the conjugate hemisphere are both monotonically increasing functions. The flat region for the arrival latitude that occurs around 10^{o} of input latitude denotes a defocusing region and has been fully discussed in Chapter 4.

For input latitudes between $\sim 35^{o}$ and $\sim 45^{o}$, the peak of ionization that occurs along the mid-latitude field lines performs like a very wide duct. Depending on the latitude of excitation the upgoing rays will meet gradients at the top of the path which correspond to the center or to the sides of the duct. The result is the wiggly behavior of the latitude where the rays will be observed for input latitudes varying from 35^{o} to $\sim 45^{o}$.

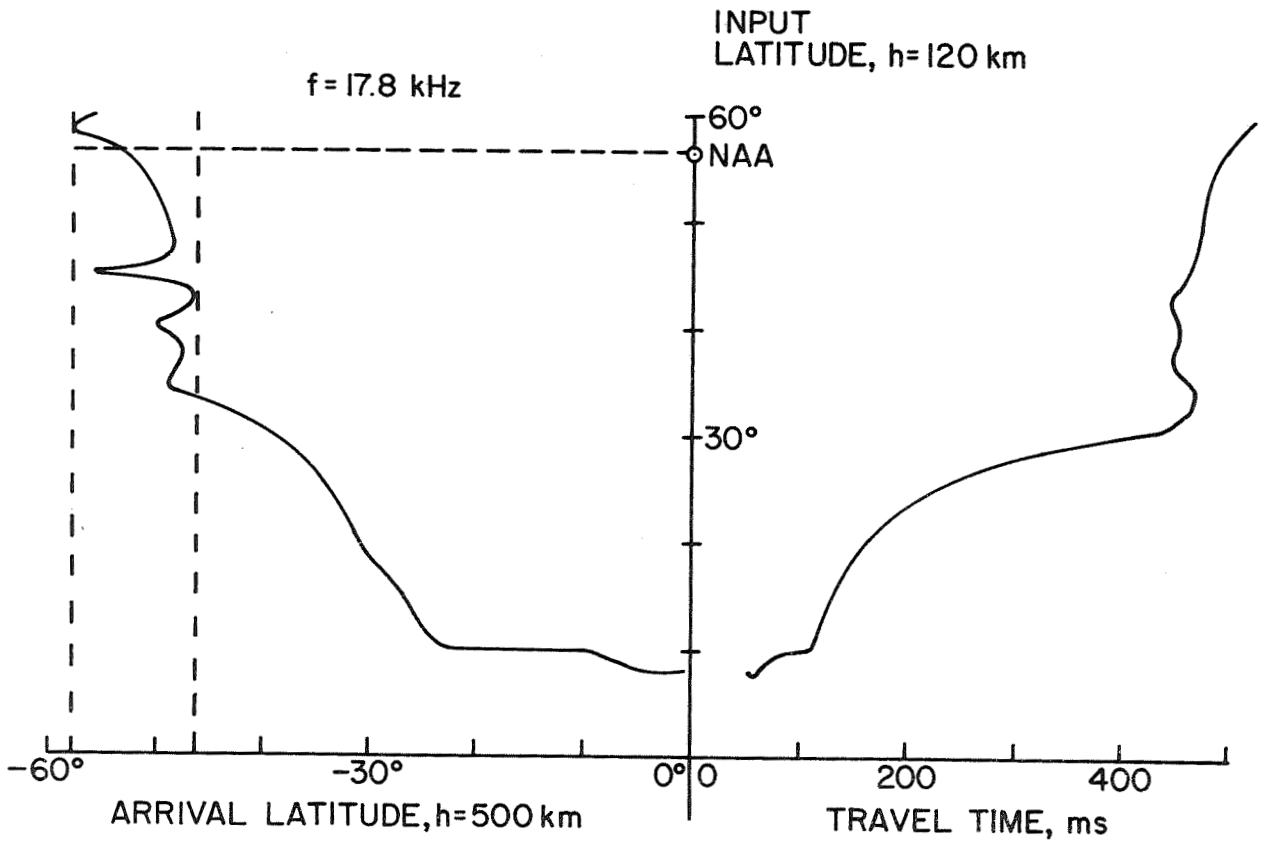

Figure 43. Arrival latitude and corresponding travel times for waves of 17.8 kHz as a function of the input latitude in the northern hemisphere.

For input latitudes between $\sim 45^{o}$ and 60^{o} the negative latitudinal gradient of electron density displayed in Figure 40 performs in the way previously deduced and provides rays that reach higher L values for increasing values of input latitude until a cutoff occurs at L = 4.0 after which the arrival latitude decreases again. That cutoff, in this particular case, is caused by the steep gradient of electron density at the plasmapause. Figure 44 shows the details of the last portion of the ray trajectory which produces the above cutoff for the downcoming waves of NAA in the southern hemisphere. Arrows indicate the directions of the wave normal pushing the ray toward the plasmapause shell at $L_o = 4$. After reaching the plasmapause the ray deviates inward to lower L values because of the elevated local gradients of electron density (ψ becomes positive). Rays starting in the northern hemisphere at latitudes higher than the input latitude of the above cutoff ray change the sign of ψ from negative to positive at higher altitudes at $L_o \leq 4$ and arrive at the receiving height of 500 km at lower latitudes as displayed in Figure 43. Clearly the mechanism of cutoff is related to the position where ψ passes through zero which in turn is related to the gradients of ionization met by the ray during its progression. Therefore the high latitude cutoff in the hemisphere conjugate to the transmitter may occur at the plasmapause, as in the present magnetospheric model, but it may also be caused by the existing gradients inside the plasmasphere in which case no connection would exist between the cutoff latitude and the plasmapause position. This point will be pursued further in the analysis of whistlers received at the downcoming end of the trajectory (Chapter 5). Figure 43 displays all the features of nighttime satellite measurements we were looking for, namely:

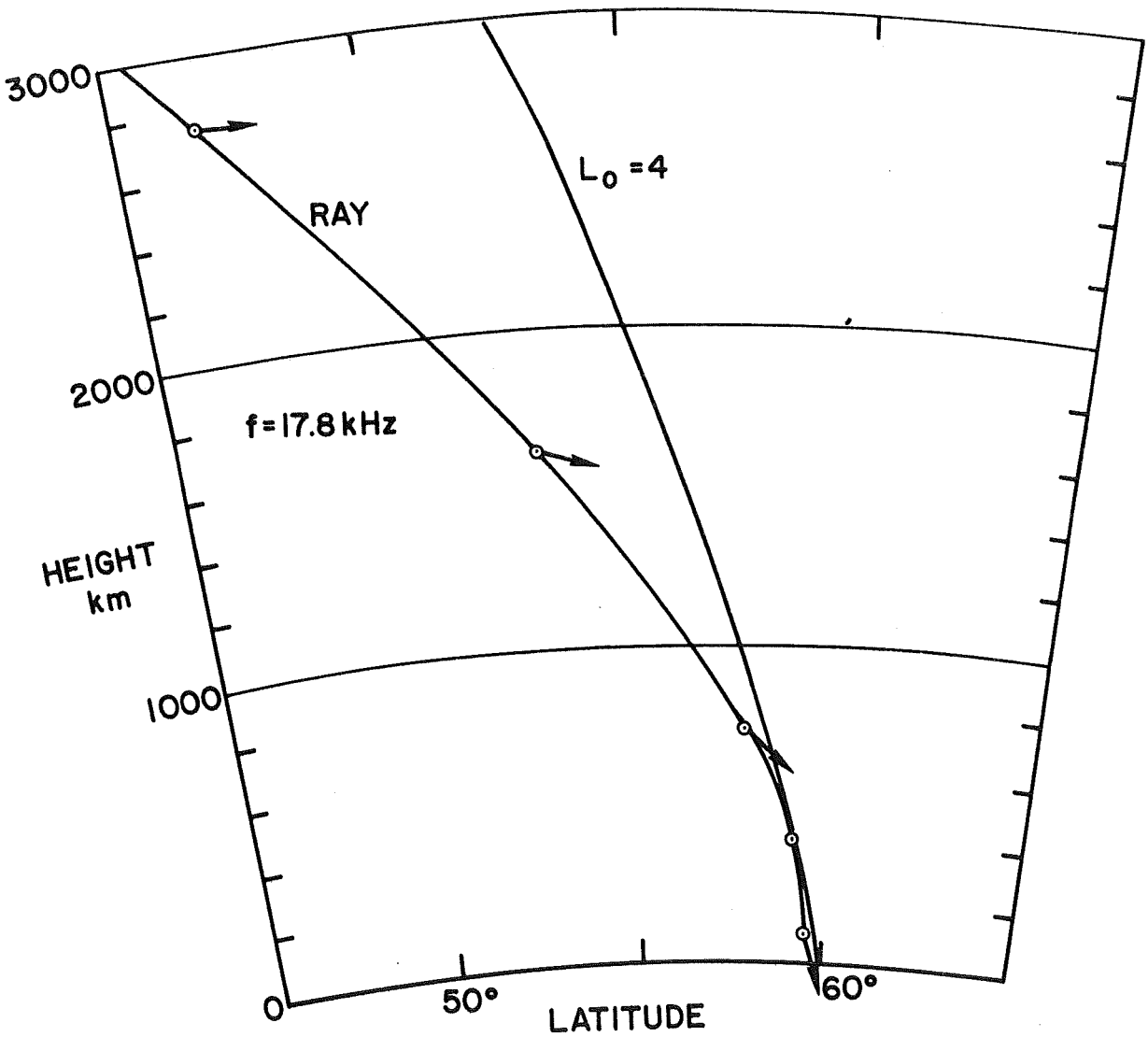

Figure 44. Details of the last descending part of the ray that produces the high-latitude cutoff of NAA waves. At $L_o = 4$ there is a steep gradient of ionization corresponding to the plasmapause boundary.

1. equatorial defocusing.

2. enhancement of the signal in the conjugate region: Figure 43 shows the southern ionosphere corresponding to the conjugate region of NAA, mapped by rays coming from the neighborhood of the transmitter in the northern ionosphere. Therefore, as saturation normally occurs in a region surrounding NAA we should also observe saturation in the conjugate region.

3. high latitude cutoff in the conjugate region.

E. CONCLUSIONS

In the present work emphasis has been placed upon the importance of the latitudinal gradients of electron density for the propagation of VLF waves in the magnetosphere. In fact a new theory of VLF propagation (the PL-mode) has been derived from the discussion. Propagation in a model magnetosphere including latitudinal gradients of ionization justifies all the features presented by typical OGO-4 records of magnetic field amplitude from signals generated on the ground by VLF transmitters during nighttime. For daytime the trend of increasing ionization toward low latitudes is maintained (see Brace et al., [1967]; Reddy et al., [1967]) and therefore the same kind of propagation is expected to dominate in the magnetosphere.

Several new phenomena related to the PL-mode of propagation will be discussed in Chapter 5.

V. THE PRO-LONGITUDINAL MODE OF WHISTLER PROPAGATION

A. INTRODUCTION

Having examined the principal propagation effects of cross-field gradients of electron density, on whistler mode waves of 17.8 kHz, it is proposed to examine the effects these gradients may have in other parts of the whistler spectrum. It will be seen that the PL-mode, characterized by propagation with the wave normal inside the cone $\pm\psi_m$ around the geomagnetic field, is a stable mode of propagation in the sense that it can be excited for a broad variety of magnetospheric models and wave frequencies. It is believed that the following discussion, necessarily short, is the beginning of much future work in whistler research because the PL-mode seems to be the most naturally occurring mode of propagation in the magnetosphere. For example, the PL-mode will supply the dispersion interpretation of whistlers that are received almost continuously by low-altitude polar orbiting satellites. The PL-mode also provides a possible interpretation for certain whistlers received on the ground.

In the following discussion we will present some properties of the PL-mode of whistler propgation based on the model magnetosphere that has been employed in the previous section. It is understood that some of the propagation features provided by that model are not necessarily of general character, but may be a feature supplied by the particular model magnetosphere. Again, only the effects of electrons is considered.

B. HIGH-LATITUDE CUTOFF IN THE OCCURRENCE OF WHISTLERS

Figure 45 shows the mapping of the southern hemisphere ionosphere by whistler frequencies whose lightning sources originated in the northern

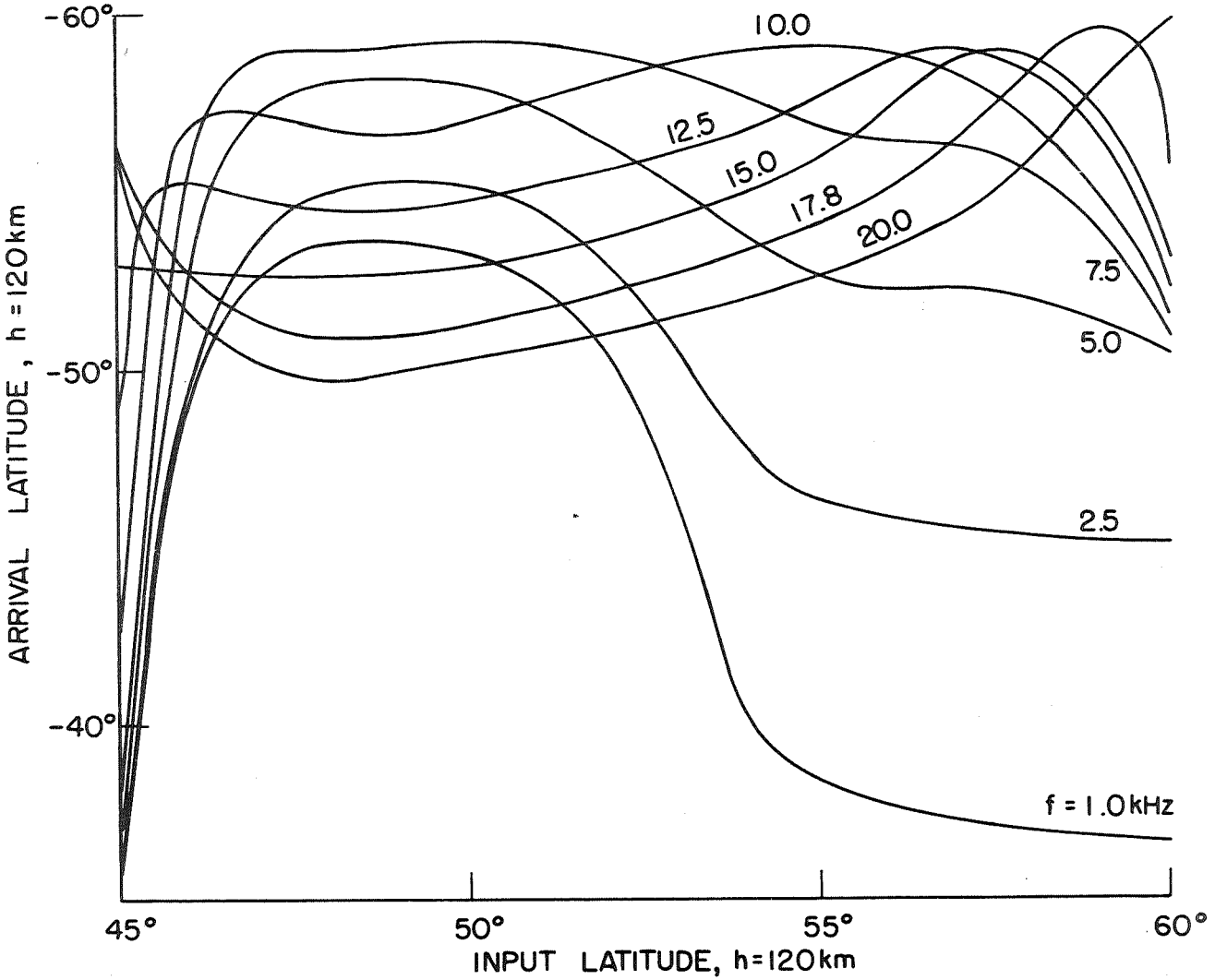

Figure 45. Arrival latitudes as a function of input latitudes in the northern hemisphere for waves from 1 to 20 kHz.

hemisphere. Arrival latitude of whistler waves at a receiving height of 120 km is plotted as a function of the input latitude for the range 45^{o} to 60^{o} in the northern hemisphere. The curves of Figure 45 are parametric in frequency and illustrate several features. A general feature of Figure 45 is that at a fixed frequency each single downcoming whistler received at a specified latitude usually comes from more than one point in the conjugate hemisphere. For example, a 500 km orbiting satellite at -50^{o} latitude would receive a 1 kHz downcoming wave that started in the northern hemisphere at 46.2^{o} and 51.8^{o} latitude (slightly different values are shown in Figure 45 where the receiving height is 120 km). Observe next how the curves change when the frequency increases consecutively from 1 to 20 kHz: the arrival latitude decreases when the input latitude varies from 50^{o} to 60^{o} at low frequencies and has a reversed behavior at higher frequencies. The dissimilarities in the ray paths presented at different frequencies are related to the frequency dependent integrated effect of magnetospheric gradients upon the wave normal during the ray progression. A mathematical treatment of ray behavior as a function of frequency and electron-density gradients is difficult and beyond the scope of the present work.

Figure 45 also displays a maximum latitude of observation for each frequency and therefore predicts a high-latitude cutoff in the occurrence of downcoming whistlers. For example, the highest latitudes where whistler waves of 1, 5, and 10 kHz could be observed would be respectively -53.6^{o}, -58.2^{o}, and -59.0^{o} for the particular model magnetosphere used. An important fact about the high-latitude cutoff is that the cutoff may be "natural," i.e., caused by the existing gradients inside the plasmasphere, or it may be caused by the high gradients at the plasmapause

which are associated here with the high-latitude trough of electron density at $L_0 = 4$. In Figure 45 only frequencies above $\sim$ 10 kHz present high-latitude cutoff caused by the steep plasmapause gradients. Below 10 kHz the rays display a "natural" cutoff. Figure 45 shows that in a satellite traveling poleward the low whistler frequencies should disappear first and just before the plasmapause crossing all high frequencies should also disappear. The above feature must be considered a property of the assumed magnetospheric model because, for example, for another model magnetosphere tested the behavior was reversed, i.e., lower frequencies were cut off at higher latitudes relative to the higher frequencies. Therefore we can conclude that the high-latitude cutoff is a phenomenon explained by the ray behavior in the actual magnetosphere (all tested models presented the cutoff feature) and that the latitudinal behavior of the cutoff frequency is dependent upon the gradients of the electron-density in the magnetosphere as well as upon the position and gradients at the plasmapause. This interpretation agrees with the measurements in the sense that the behavior of the cutoff frequency with latitude does not follow a unique pattern. However, an erosion that begins at high frequencies and progressively erodes all lower frequencies as OGO 4 moves poleward seems to be the most frequently occurring observation (see Figure 34).

For some tested magnetospheric models only the "natural" high-latitude cutoff occurs. Therefore, without further knowledge of the existing electron distribution in the magnetosphere, we cannot distinguish whether a given high-latitude cutoff observation is caused by the plasmapause gradients or, rather, caused by the smooth gradients inside the plasmasphere. This point requires further investigation.

C. WHISTLERS WITH LATITUDE-INDEPENDENT TIME-DELAY

Figure 46 shows the time spent by each whistler frequency energy to travel from the northern hemisphere to a receiving height of 500 km in the southern hemisphere as a function of the arrival latitude. Arrows in each curve show how the input latitude progresses between 45^{o} and 60^{o} in the northern hemisphere for each frequency. For example, the curve for 2.5 kHz shows an almost constant delay time between -45^{o} and the cutoff latitude -54.5^{o} when the input latitude varies from 45^{o} to 49^{o} (as seen in Figure 45) and shows slightly smaller delay times for input latitudes between 49^{o} and 60^{o}.

Figure 46 displays the outstanding phenomenon of an almost constant time delay for whistlers as a function of latitude as denoted by nearly horizontal curves. It shows also that for a certain range of latitudes it should be possible to observe two distinct whistler traces at high frequencies and that the traces should converge at low frequencies. Figure 47 shows the frequency-time spectrogram of this "gemini" (or "hook") whistler that should be received by a 500 km satellite at -52^{o} latitude.

The above double-trace "hook" whistler, whose distinct traces converge at low frequencies, was first reported by Gurnett et al., [1966]. The explanation of the "hook" whistler given by Shawhan [1966] assumes that for a given input latitude <u>two different</u> wave-normal directions may produce two distinct rays that would present a crossing point in the opposite hemisphere at the satellite. There are three strong objections to the above interpretation:

1. The explanation is based on the possibility of wave scattering in the E region of the ionosphere which is unlikely to occur

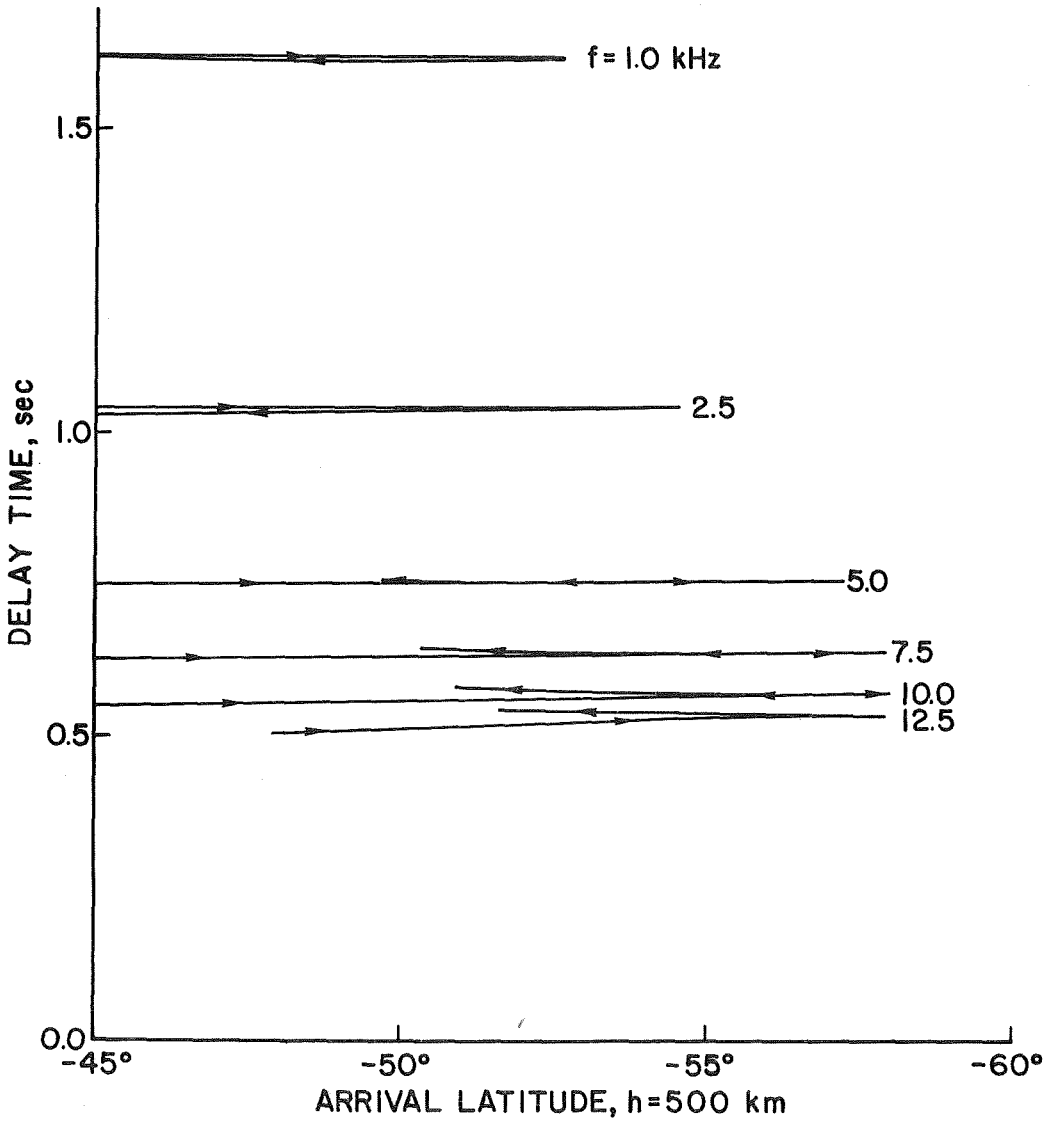

Figure 46. Travel times as a function of the receiving latitudes. Arrows in each curve show how the input latitude progresses between 45^{o} and 60^{o} in the northern hemisphere for each frequency.

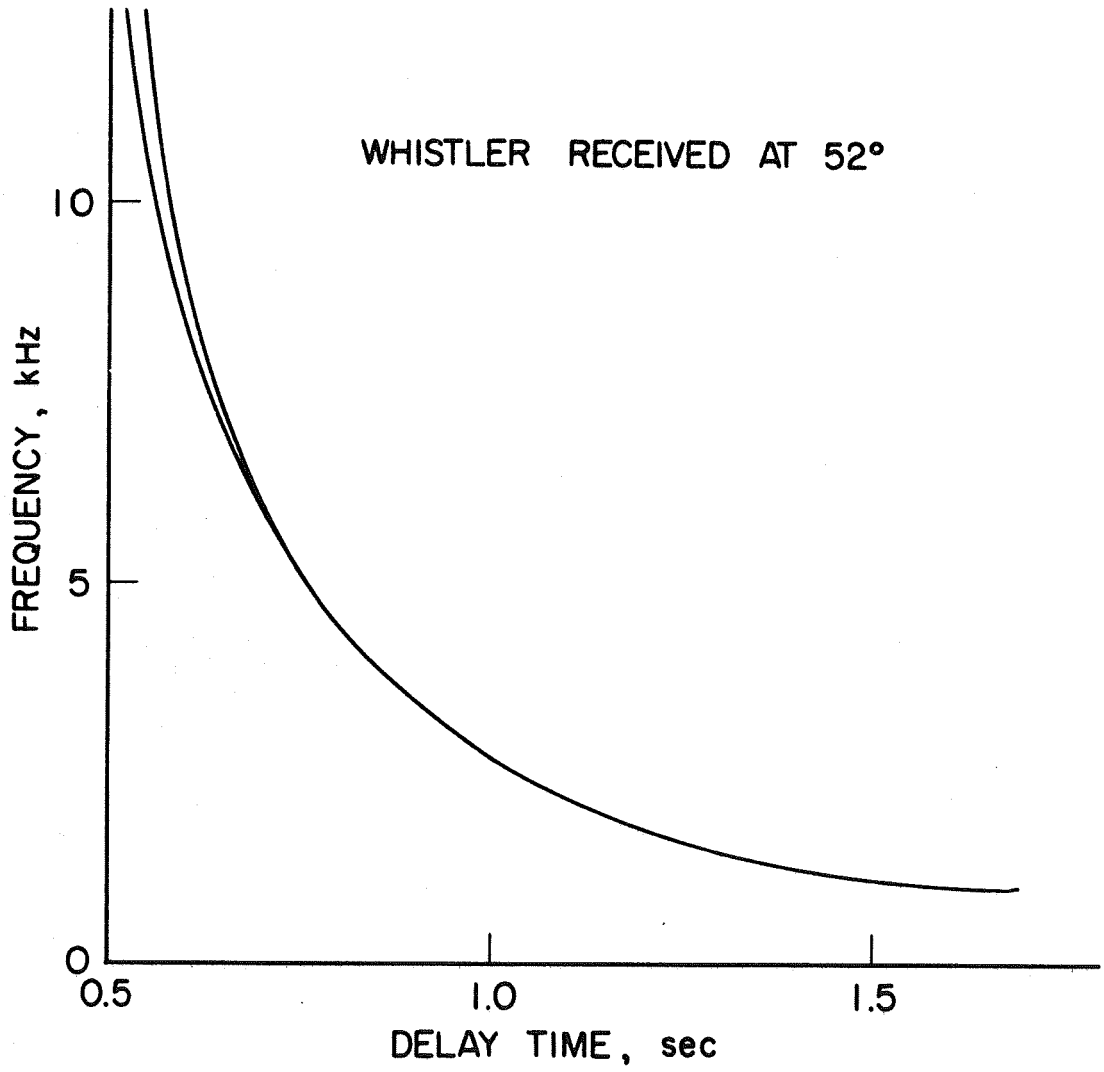

Figure 47. Predicted "hook" whistler to be received at 500 km height and at -52^{o} latitude.

for VLF waves. Furthermore, this interpretation would require E region scattering continuously for some thousand kilometers because hook whistlers are easily observed during 10 - 15 degrees of OGO-4 passes at mid latitudes.

2. The ray paths produced by the ray-tracing technique of the above report [Shawhan, 1966] predicted heights and latitudes of observations completely different from the measurements.

3. The PL-mode of propagation, based simply on realistic profiles of ionization, shows that the hook whistler is caused by reception at a single latitude of two wave packets coming from distinct entry points in the hemisphere of the source.

The high-latitude cutoff in the occurrence of whistlers, the latitudinally constant delay time for whistlers and the hook whistler are the most impressive results explained by the present simple theory of whistler propagation. All these features are exhibited in the frequency-time spectrograms of Figure 34 where constant delay time whistlers are seen followed by twin convergent traces, between $L \cong 2.4$ and $L \cong 3.9$. Figure 48 shows expanded pieces of the record displayed in Figure 34 around points 1, 2, and 3 in order to show the details of some hook whistlers of Figure 34.

The spectrograms of Figure 34 show a high latitude cutoff effect in a form of erosion with the disappearance of the high frequencies of whistlers starting at $L \cong 3.9$. This is followed by the gradual vanishing of lower whistler frequencies until $L \cong 4.8$ where no more downcoming whistler frequencies are received.

The predicted constant-delay time whistler seems to be a general feature of the actual magnetosphere because that property has been generated by several different magnetospheric models. On the other hand the two different delay times predicted for the high frequencies

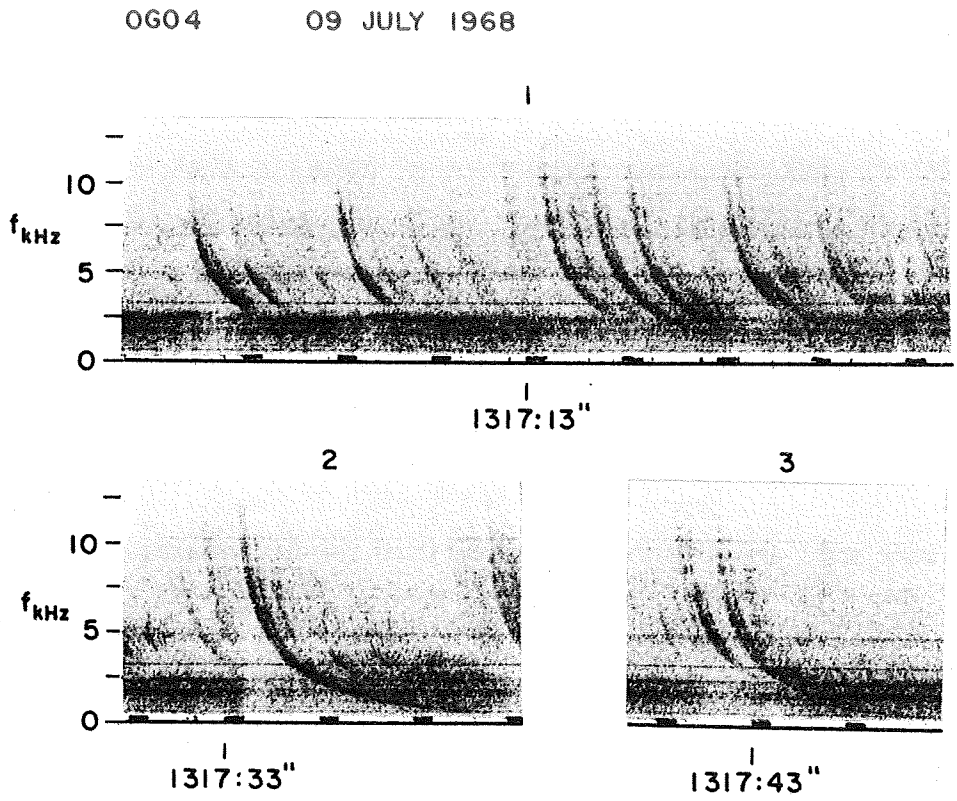

Pieces of the OGO-4 record displayed in Figure 34. The frequency-time spectrum from 0 to 12.5 kHz shows several hook whistlers.

of the "hook" whistler of Figure 47 may or may not be observed. For some magnetospheric models the differences in delay times are greater than the differences displayed in Figure 46, for other models the differences are negligible and therefore only one whistler trace should be observed. Nevertheless, the important property that has been generated by all magnetospheric models is that the signals received at a given latitude come, in general, from more than one latitude in the conjugate hemisphere, and that the delay times for the different trajectories are in general different.

The feature of a constant delay time as a function of the receiving latitude must be considered a result of the interrelated behavior between the ray group velocity and the length of the path at different arrival latitudes provided by electron-density gradients. Here again, the mathematical interpretation of the global properties of the rays is very difficult and is post-poned.

D. WHISTLERS RECEIVED ON THE GROUND

The PL-mode of whistler propagation also provides a possible interpretation of some whistlers received on the ground. The interpretation is based on the following study of wave-normal direction for the downcoming waves just above the E region of the ionosphere. Wave transmission through the lower ionosphere and excitation of propagating waves inside the ground-ionosphere space requires that the wave-normal direction of the downcoming ray lies within a "transmission cone." The transmission cone is the geometrical locus of the wave-normal direction having unity horizontal projection of the refractive index. Figure 49 shows the horizontal component μ_H of the refractive index at 120 km in the

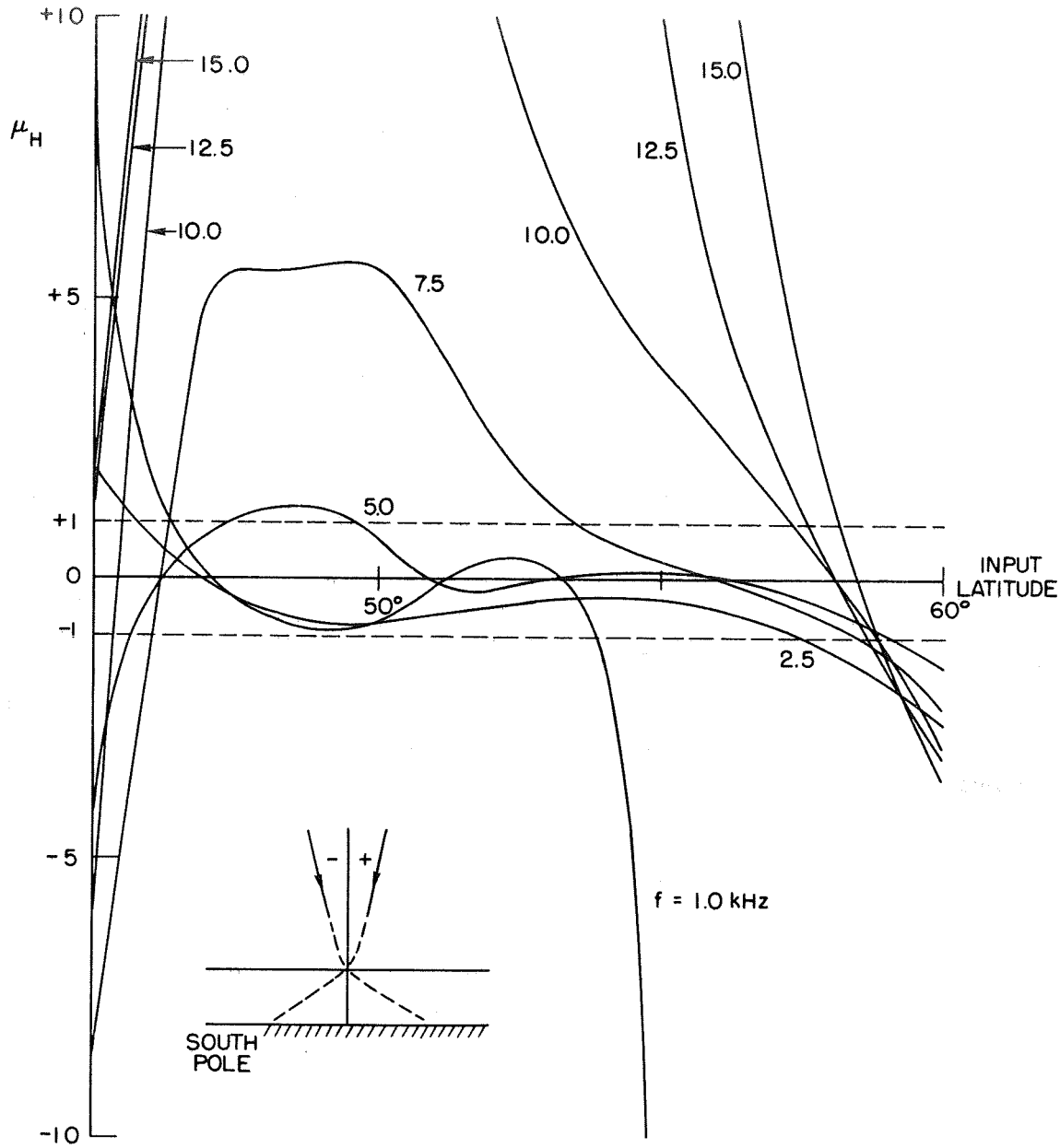

Figure 49. Horizontal component μ_H of the refractive index for downgoing waves in the southern hemisphere at 120 km height as a function of input latitude.

southern hemisphere as a function of the input latitude in the northern hemisphere. The curves are parametric in frequency. The sketch at the bottom of Figure 49 shows the adopted sign convection for μ_H: positive wave-normal angles may only produce waves traveling southward in the air below, while negative angles may only launch waves propagating toward the equator. Figure 49 shows that the PL-mode waves generated by the model magnetosphere arrive in the conjugate hemisphere with a wide range of wave-normal directions, depending on the input latitude. Also displayed is the important fact that μ_H crosses the line $\mu_H = 0$ one of more times for each frequency. Thus for a given whistler frequency, it is always possible to find a latitude for which an upgoing wave of that frequency will produce, in the conjugate hemisphere, a downcoming ray whose wave normal is vertical at 120 km. Figure 49 shows that the excitation of propagating waves below the ionosphere by whistler mode waves should be easier below 7.5 kHz because for these lower frequencies there is a wide range of input latitude which produces downcoming rays whose wave normals are inside the transmission cone $\mu_H = \pm 1$ at the receiving end of the trajectory in the conjugate hemisphere. At higher frequencies the range of input latitudes is smaller producing $\mu_H \leq |1|$ in the conjugate hemisphere (observe the curves for 10, 12.5, and 15 kHz).

Using the results of Figure 45 and Figure 49 it is possible to derive the range of arrival latitudes for which the downcoming whistler waves will present wave-normal directions within the transmission cone $\mu_H = \pm 1$ at 120 km. This is shown in Figure 50 by horizontal bars which indicate the range of latitudes where whistler frequencies of 1, 2.5, 5, 7.5, 10, 12.5, and 15 kHz would present $\mu_H \leq |1|$ in the conjugate

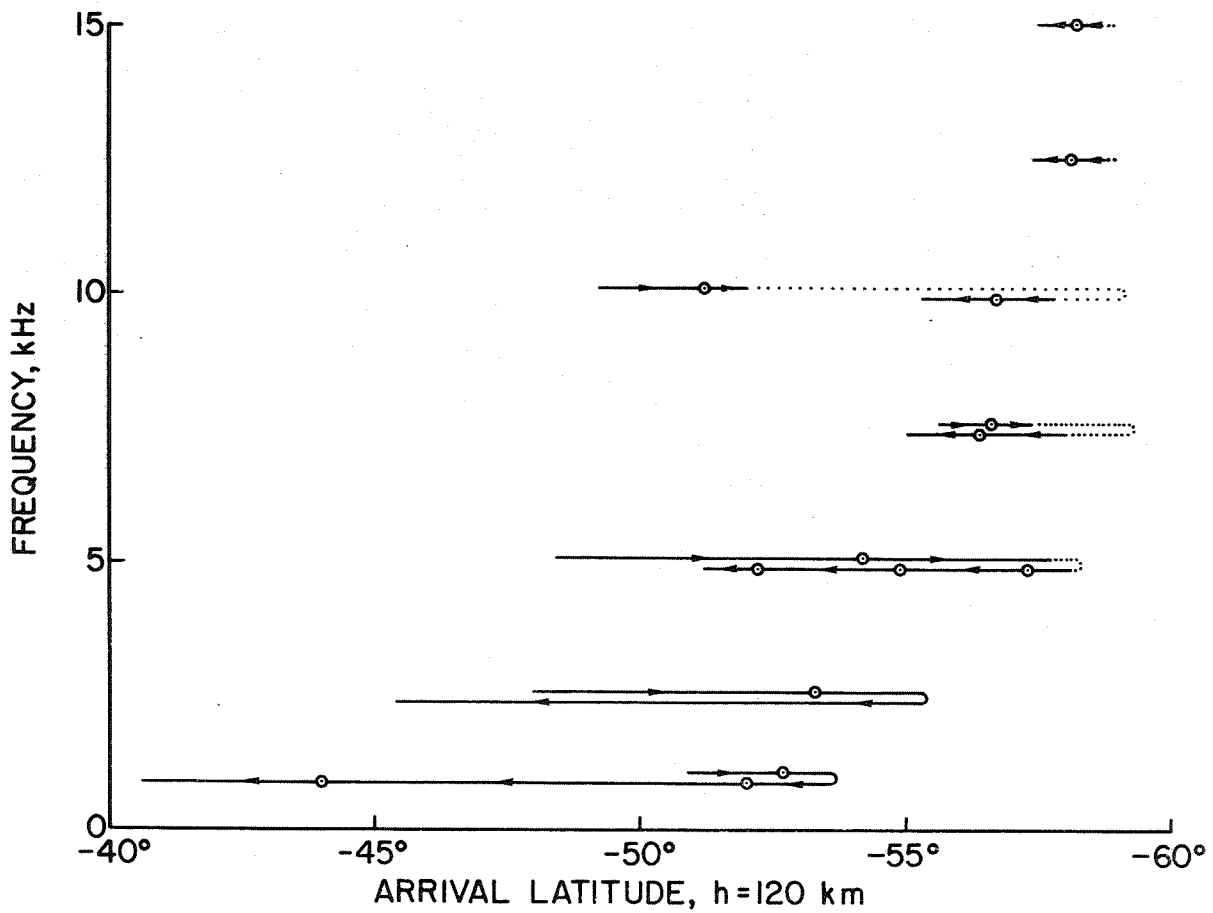

Figure 50. Range of latitudes where whistler frequencies of 1.0, 2.5, 5.0, 7.5, 10.0, 12.5 and 15.0 kHz present $|\mu_H| \leq 1$. Arrows indicate how the input latitude progresses in the northern hemisphere and small circles mark the latitudes where the downcoming wave-normals are vertical at 120 km.

hemisphere. The arrows in each curve of Figure 50 indicate how the input latitude progresses in the hemisphere of origin and small circles mark the latitudes where the downcoming wave normals are vertical at 120 km.

Figures 49 and 50 give the following new interpretation of whistlers received on the ground: the gradients of electron density and magnetic field in the actual magnetosphere bend the wave normal of the upgoing whistler waves toward the equator producing rays that cross the equator between $\sim 2.$ to 2.6 earth radii and arrive in the conjugate hemisphere with wave normals that are inside the transmission cone for a wide range of conditions. These figures also suggest that a high-frequency cutoff for the whistler received on the ground is caused by contraction of the range of input and output latitudes which provide $\mu_H \leq |1|$ in the E region at the receiving end of the trajectory. For example, if a lightning flash occurs at 50^{o}N, Figure 49 shows that the 12.5 kHz wave component should travel approximately 800 km northward before being launched in the whistler medium at the convenient latitude of $\sim 58^{o}$N which would provide $\mu_H \cong 0$ in the conjugate hemisphere. Therefore this 12.5 kHz whistler component would be much weaker than the ground received lower frequencies because of the following factors:

1. Great distance traveled with $1/r$ variation. For example a wave that travels 800 km before reaching the ionosphere is attenuated 20 db more than another wave that only travels 80 km until striking the bottom of the ionosphere.
2. Smaller transmission coefficient in the lower ionosphere caused by large angle between the vertical and the incident wave normal (about 82^{o}), (see, for example, Chapter 2).
3. Further defocusing of the rays at the receiving end of the

trajectory where the downcoming power flux contained in 1.5^{o} of latitude (see Figure 50) is dispersed in all directions inside the earth-ionosphere space.

Hence, a ground receiver should detect whistlers whose cutoff frequencies are related to the locations of the two ends of the ray trajectory in the magnetosphere in addition to the location where the corresponding lightning flash occurs.

As derived in Section C of this chapter, the PL-mode whistler resembles whistlers that follow the Eckersley dispersion-law (see Helliwell [1965], Chapter 3). For all magnetospheric models tested, no nose frequency has been generated by the PL-mode for whistler frequencies below 20 kHz. The absence of nose frequency comes from the fact that the PL-mode waves cross the equator at relatively low heights. This means the wave frequencies below 20 kHz are always much smaller than the minimum gyrofrequency along the ray trajectory. However, for the excitation of nose whistlers under conditions of PL propagation it is necessary that f be compariable to f_H at some region along the ray. Therefore, the PL-mode does not generate nose whistlers.

When detecting Eckersley-type whistlers on the ground (single whistler, long echo train of whistlers, or whistler followed by train of nose whistlers) the question will arise whether the whistler is ducted or is a PL whistler. No definite answer can be given at this time because no measurements have been planned for this purpose. One method of recognizing the PL-mode whistler would be by the use of a direction finder for whistler frequencies. If it is a PL-mode whistler, the direction of arrival for different frequencies will be different, as inferred from Figure 50.

E. CONCLUSIONS

Ray trajectories inside a "real" magnetosphere including a plasmapause boundary and electron density gradients, such as those measured by Brace et al. [1967] lead to the PL-mode of VLF propagation. The PL-mode is characterized by propagation with the wave normal inside a cone $\pm\psi_m$ relative to the earth's magnetic field. It has been shown that the PL-mode justifies at once several features regularly observed with the OGO-4 satellite. Because so many effects are connected by a common cause, namely the PL-mode of propagation, we conclude that the real magnetosphere cannot be very different in shape from the model magnetosphere used in the present study. These phenomena represent a potential tool for measuring electron density distributions in the magnetosphere based on whistlers observed with polar satellites. For example, for matching delay times, latitude of observations, and multiple traces of whistlers from low to high latitude measurements it would be necessary to use a ray-tracing computer program with a standard magnetosphere model which should be suitably changed at certain points in order to match all of the data. Although the technique of replacing existing magnetospheric models by more suitable models would be relatively complex the results should be quite worthwhile. The development of this technique of magnetospheric shaping based on whistler characteristics would mean that the thousands of whistlers that are observed at each satellite revolution could have important aeronomic applications.

Another important feature introduced by the PL-mode is a concentration of VLF energy between ~ 2.0 and 2.5 earth radii over the equator. This phenomenon is caused by the equatorward bending of the wave normals produced by the gradients of ionization. As a result all

the VLF waves launched in the magnetosphere from mid to high latitudes inside the plasmasphere cross the equator with very low divergence of power flow. This result may be extremely important in the study of wave-particle interactions in the magnetosphere.

A property also important for the study of wave-particle interactions is the relationship between the delay time and the wave-normal angle ψ presented by the PL-mode of propagation. Typically the PL-mode may present large angles between the wave normal of the waves and the geomagnetic field lines in the downcoming section of the ray-trajectory and may show at the same time a delay time typical of purely longitudinal propagation. Therefore the resulting low values of phase velocity projected along the field lines may be the cause of interaction between the waves and a stream of charged particles guided by the geomagnetic field. For example, emissions triggered by signals from the low-power transmitter of Omega (New York) have been observed by OGO 4 at $L \cong 4$ near Byrd Station. This result fits the present theory in the sense tha the PL-mode not only justifies the presence of Omega frequencies at high latitudes in the conjugate hemisphere but it also provides large wave-normal angles ψ at these latitudes. Furthermore, under certain circumstances the interacting waves could be observed on the ground if the gradients of ionization were such as to bend the wave normal toward the vertical in the last part of the downcoming trajectory. Clearly no speculation is involved here; these are results obtained by merely analyzing the ray behavior in the model magnetosphere assumed in this work.

Finally the PL-mode of propagation can explain the fact that whistler activity is low above $L \cong 3$ as observed by the OGO-3 satellite

(Bruce Edgar, private communication) while the whistler activity detected at high L shells (above L = 3) but aboard low altitude satellites (OGO 2, OGO 4) is very intense. This is exactly the main characteristic of the PL-mode, namely ray trajectories that cross the equator at low altitudes upcoming from high latitudes and downgoing to high latitudes in the conjugate hemisphere.

VI. AMPLITUDE FADING

A. INTRODUCTION

In this concluding chapter we discuss a class of amplitude fading that has been observed on OGO 1, OGO 2 and now on the OGO-4 satellite. The fading occurs for upgoing waves and is generally detected close to VLF transmitters located at mid latitudes. Heyborne [1966] reported this type of fading from observations with OGO 1 and OGO 2. He suggested several fading mechanisms but definitive interpretation has not been obtained. Here again the above fading phenomenon will be tentatively interpreted. These tentative interpretations of fading are not completely consistent but they may serve as a guide for further work. For example, we will prove that certain fading mechanisms are not adequate to explain specific features of fading observed on OGO 4. Although these proofs represent negative results they will be valuable when a better interpretation of the phenomenon is attempted.

B. AMPLITUDE FADING RELATED TO PLASMAPAUSE CROSSING

Figure 51 and Figure 52 show two OGO-4 spectrograms recorded approximately under the same conditions on two consecutive days, 20 and 21 September 1968. Each figure shows 4 minutes of a continuous record displayed here in 4 segments (one panel for each minute). The magnetic field amplitude in dbγ of NAA signals at 17.8 kHz as measured by the stepping receiver No. 3 and telemetered to ground via VCO is shown by the upper trace in each panel. Also shown is the broadband spectrum from 300 Hz to 12.5 kHz measured as a function of time (UT) and L value of the satellite. The corresponding ground projections of the two OGO-4 trajectories are shown in Figure 53. NAA was operating in the FSK

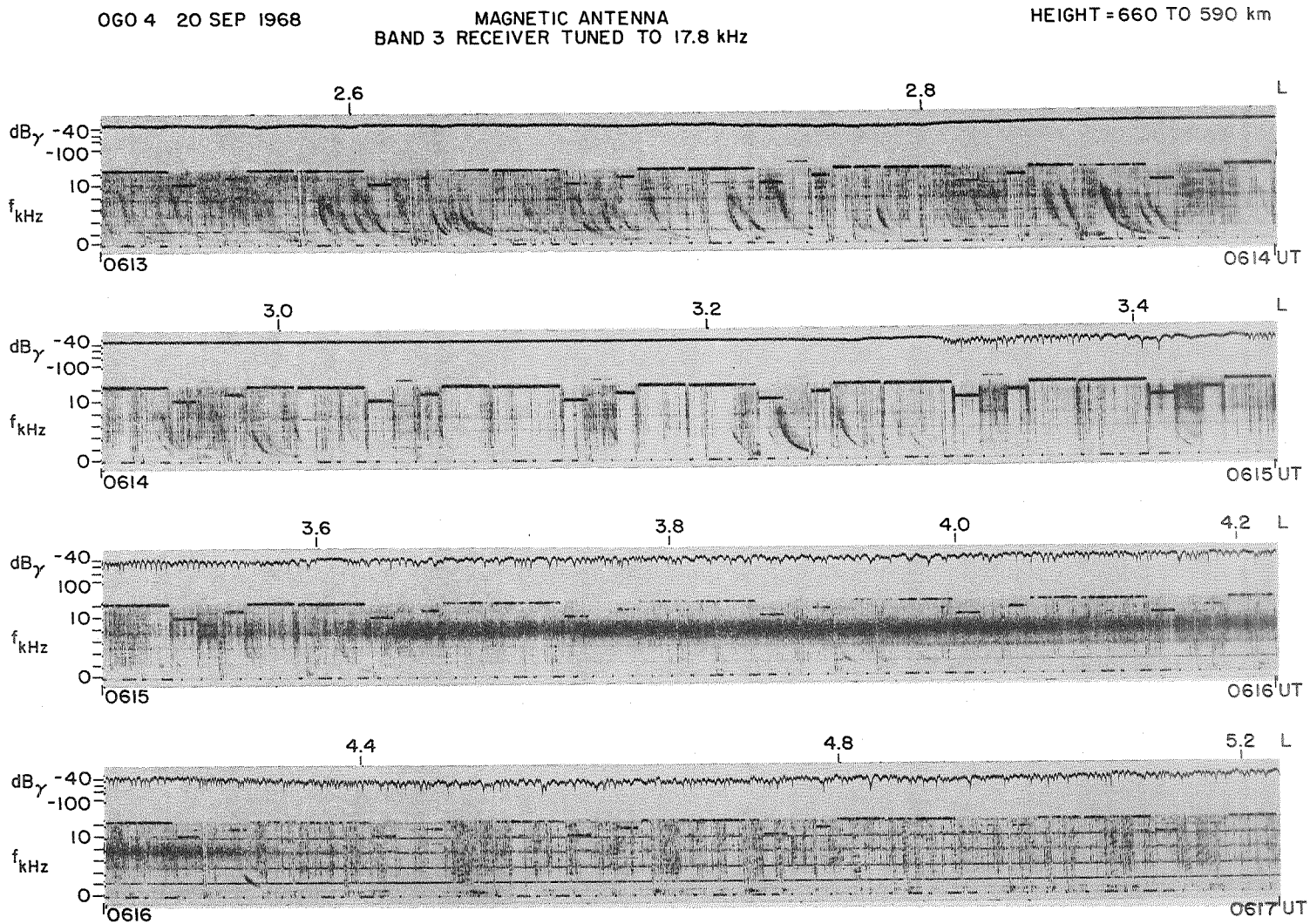

Figure 51. Magnetic field amplitude of NAA signal and 0 to 12.5 kHz broadband spectrum as functions of time UT and L value of OGO 4.

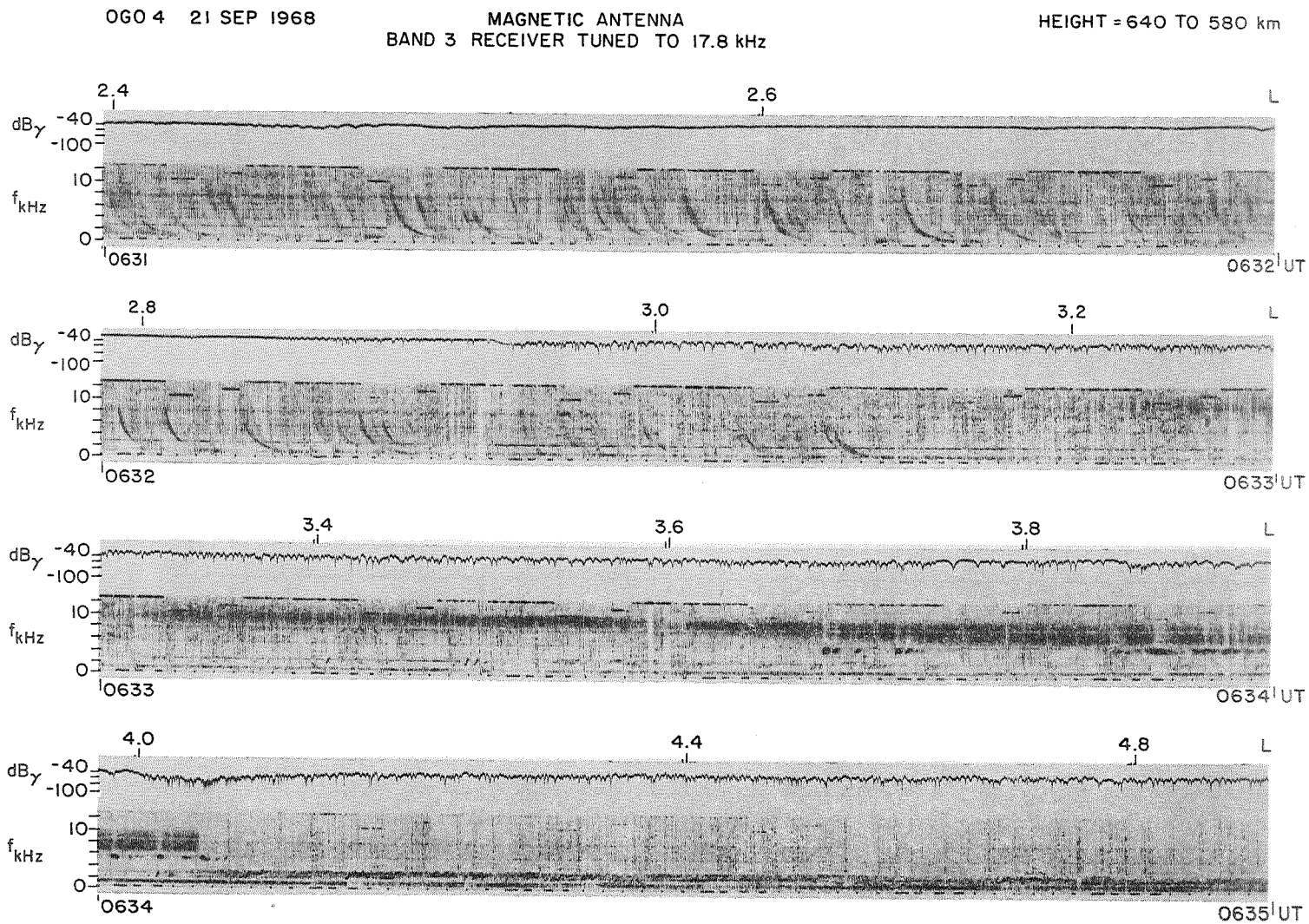

Figure 52. Repetition of the features displayed in Figure 51 for 21 September 1968.

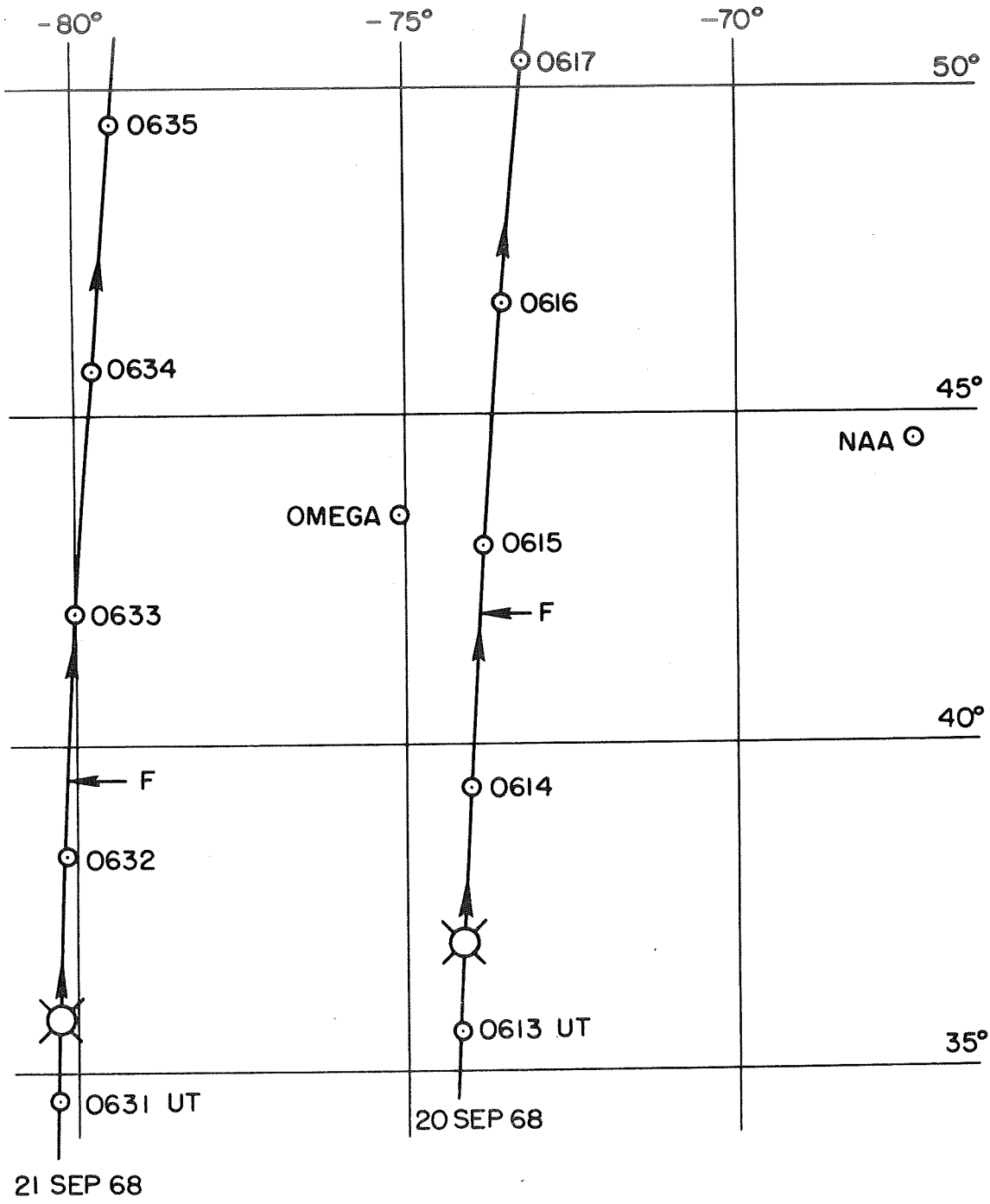

Figure 53. Ground projections of the two OGO-4 trajectories corresponding to the records of Figures 51 and 52.

mode of transmission, shifting the frequency between 17.80 and 17.85 kHz. These frequencies are detected equally inside the 500 Hz bandwidth of the band 3 stepping receiver whose output then displays a continuous trace as shown in Figures 51 and 52. Morse-code transmissions in the FSK mode can only be detected by the phase tracking receiver of OGO 4 which provides about 30 db separation between 17.80 and 17.85 kHz.

Figures 51 and 52 show that at low L values there is a steady NAA signal which is received together with a broadband spectrum of upgoing and downcoming whistler waves. The broadband spectrogram shows short whistlers and several transmission segments of Omega (New York) that are upgoing waves. Also displayed are long whistlers excited in the conjugate hemisphere that are downcoming waves at the satellite position. Next we observe that as the satellite moves northward there is a point where the NAA signal falls abruptly and then starts fading in a pseudo-periodic fashion. The position where the fading starts is indicated by an arrow F in Figure 53. At the same time the high-latitude erosion begins in the occurrence of downcoming whistlers; observe for example that the last panels of Figure 51 and 52 show only upgoing short whistlers and some traces of upgoing Omega waves. A close observation reveals that these upgoing whistlers present "choppy" traces indicating that fading is in fact occurring at all frequencies for upgoing waves. Another interesting feature presented by the records of Figures 51 and 52 is a band of noise between 6 and 10 kHz which is limited in space and begins about 1.5 degrees above the latitude of the NAA fading. The center frequency of the noise band decreases northward and disappears abruptly about 4.3 degrees later. Observe for example that the abrupt disappearance of noise in Figure 52 at 0634:05 UT is associated with a large reduction

of NAA signal which then increases again northward. This fact may be significant for the study of this "plasmapause noise" in conjunction with the related increase of attenuation observed at the boundaries of the noise region.

Figures 51 and 52 show that the signal from a mid latitude VLF transmitter is steady inside the plasmasphere and that the plasmapause crossing is associated with 1) high-latitude erosion in the occurrence of downcoming waves; 2) deep amplitude fading for upgoing waves; 3) a decrease of amplitude for upgoing signals as the fading begins; and 4) a band of plasmapause noise. Figure 11 in Chapter 2 shows for example the association between the abrupt decrease of NAA and Omega signals to the left of 0131:10 UT and the corresponding erosion for the downcoming whistlers (record BB of Figure 11). Figure 11 shows again that the rapid decrease of signals from NAA and Omega (New York) occurs at the northern boundary of the plasmapause noise (observe the noise band between $\sim$ 0131:07 UT and $\sim$ 0131:40 UT). In Figure 11 the NAA signal is measured in the 50 Hz passband of the phase tracking receiver and therefore the 17.80 to 17.85 kHz frequency shifting is detected. In this case the observation of amplitude fading is contaminated by the presence of Morse code and is discarded in the continuing discussion.

The amplitude fading of Figures 51 and 52 shows that the points of minimum amplitude are 20 to 40 db below the average level of the signal which, combined with the pseudo-periodic behavior of the fading, strongly suggests interference between two and only two waves of nearly equal amplitudes at the satellite height. This idea of interference between two waves of the same amplitude is pursued in the following discussion where three interference mechanisms are considered.

1. Interference Caused by Multiple Hops Below the Ionosphere

As indicated in Section B of Chapter 2 it is possible to observe interference between a ray that follows a direct trajectory transmitter-ionosphere-satellite and rays that bounce two or more times between the ground and the lower edge of the ionosphere before following a trajectory that also intercepts the satellite at the same point. However extensive full-wave calculations have shown that amplitude fading of the order of 5 db is predicted in this case. Therefore the fading characteristics displayed in Figures 51 and 52 rule out this multiple hop mechanism.

2. Interference Caused by Longitudinal Gradients of Ionization

Longitudinal gradients of ionization permit two waves launched in the whistler medium at different longitudes to interfere at the satellite height in the ionosphere. Therefore divergent rays originated from NAA and traveling northward may penetrate the ionosphere and interfere continuously at the height of a satellite that flies approximately in the north-south meridian. This mechanism requires longitudinal gradients of ionization outside the plasmasphere and no effective gradients inside the plasmasphere.

3. Interference Caused by Latitudinal Gradients of Ionization

Records of OGO-4 crossings of the plasmapause are characterized by an initial abrupt decrease of field intensity when the records are examined from mid to high latitudes. Observe for example the signals from NAA and Omega at 0131:10 UT in Figure 11 and the NAA signals in Figures 51 and 52 at the beginning of the fading regime. This rapid decrease of field intensity is probably caused by a defocusing of the upgoing waves at the high-latitude trough of electron density which is associated with the plasmapause. As indicated in Figure 40 there is a

rapid change in the sign of the latitudinal gradient of ionization at the trough which means that while the waves launched in the ionosphere inside the plasmasphere are pulled toward the equator the waves that propagate just outside the plasmasphere are pulled toward the pole. Therefore a defocusing of the electromagnetic field will certainly occur for waves excited from below.

On the other hand the F region of the ionosphere is highly variable at the polar side of the trough (see, for example, Calvert [1966]). Therefore the question arises whether or not irregularities of ionization may provide an amplitude fading pattern like those shown in Figures 51 and 52. The effect of small-size irregularities of electron density on the ray trajectories of waves excited from below is studied below.

The unmodulated ionospheric model $N(r)$ of Section D, Chapter 4 is used again with a modulating factor F_n such that the new profile of electron density is given by

$$N(r,\theta_o) = N(r)\, F_n \tag{6.1}$$

and we have used

$$F_n = 1 + \Delta \sin\left(\frac{\phi_o - \phi_1}{\Delta\phi}\right) \cdot \exp\left\{-\frac{(r-6490)}{H}\right\} \tag{6.2}$$

that is, the basic model $N(r)$ is modulated by a sinusoidal irregularity which is field oriented and that decreases with height. The notation is the same for Chapter 4 and here we have chosen

$$\Delta = 0.2\,, \qquad \phi_1 = 60^o\,, \qquad \Delta\phi = 0.2^o\,, \qquad H = 500 \text{ km} \tag{6.3}$$

The ray-tracing computer program of Walter [1969] produces ray trajectories in the above ionospheric model with the result shown in Figure 54. This figure shows the latitudes where a satellite at 600 km would receive the rays penetrating the ionosphere between the input latitudes of 59.95^{o} and 60.35^{o}. Also shown in Figure 54 is the modulating factor F_n at 120 km. Observe that F_n simulates latitudinal irregularities of 11 km in size (one half of the sine-wave period). Figure 54 shows that at any satellite point in the range of the figure the spacecraft receiver would detect signals simultaneously coming from different latitudes producing wave interference. However, Figure 54 also shows that the satellite would in general receive signals from more than two different latitudes. Usually four or five different rays are received at the same point. Therefore the ray behavior at 640 km given by Figure 54 does not justify the deep fading patterns of Figures 51 and 52.

C. CONCLUSIONS

In this chapter we have tried three different mechanisms of interference for interpreting the amplitude fading in upgoing VLF waves observed on OGO 4. We showed that interference caused by multiple hops below the ionosphere cannot provide 20 - 30 db amplitude fading. Although not completely convincing it seems that horizontal irregularities of electron density are the most probable cause of the fading. The hypothesis of latitudinal and/or longitudinal irregularities of electron density would require a smooth ionosphere inside the plasmasphere and a highly variable ionosphere at the polar side of the trough of ionization. This hypothesis matches exactly the findings of Calvert and Van Zandt [1966] and Calvert [1966], who found very steep latitudinal electron density

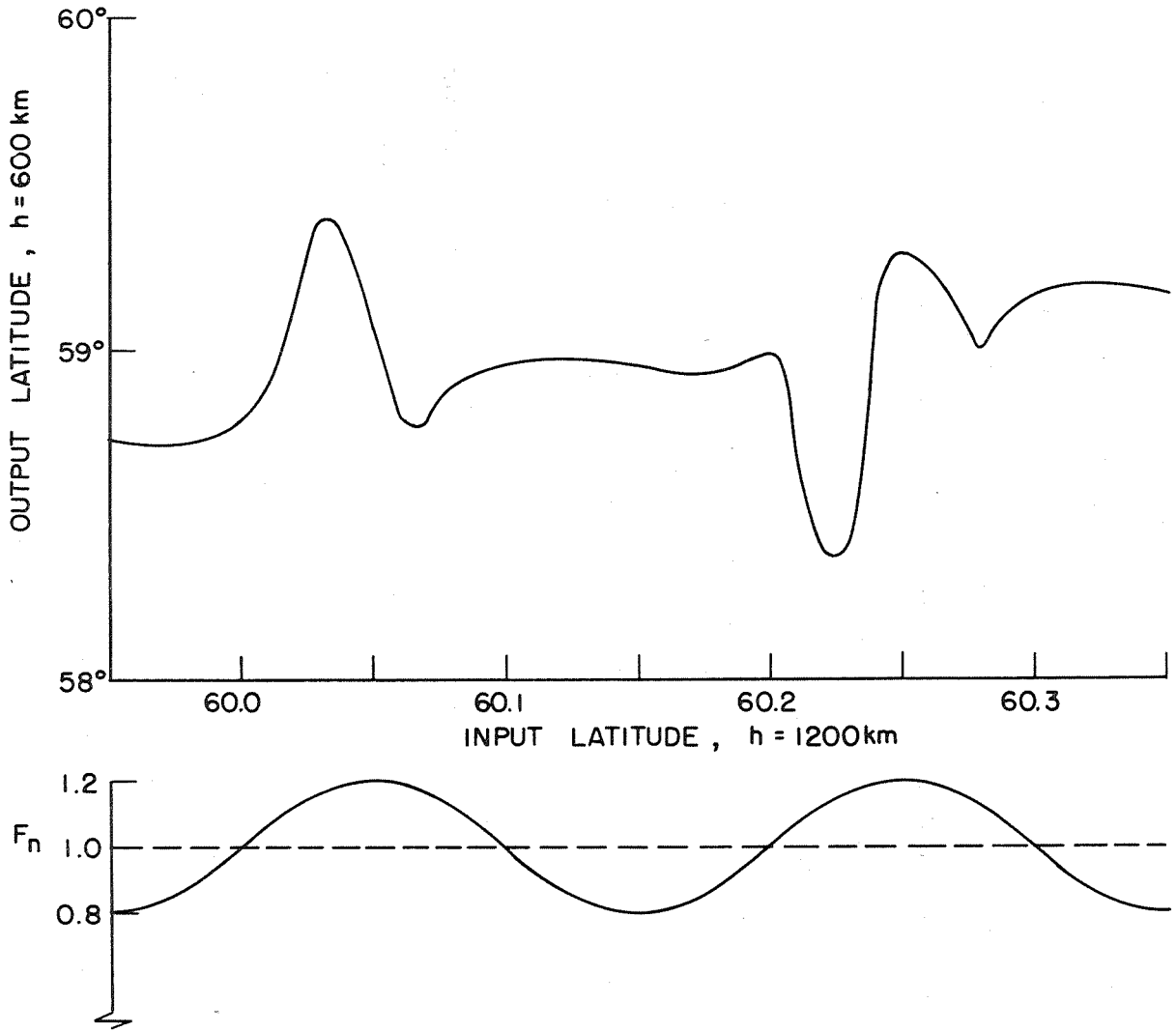

Figure 54. Receiving latitudes at 600 km for rays that start between the input latitudes of 59.95° and 60.35°. Also shown is the modulating factor F_n at 120 km (see text).

gradients in the topside F layer at high latitudes. They showed that the electron density gradients caused by irregularities at the equator side of the trough are relatively small and that the irregularity pattern changes substantially at high latitudes. They reported low size structures of electron density and very steep gradients at the polar side of the trough. For example, changes of 50% in a distance of 8 km have been observed at latitudes above the trough of ionization. Therefore the requirement of a variable ionosphere outside the plasmasphere that would be associated with amplitude fading for upgoing waves is confirmed experimentally. However, the details of the fading mechanism are not clear at this time.

REFERENCES

Angerami, J. J. and J. O. Thomas, Studies of planetary atmospheres, 1, the distribution of electrons and ions in the earth's exosphere, J. Geophys. Res., 69, 4537, 1964.

Aubry, M. P., Influence des gradients horizontaux de densité électronique sur la direction des normales d'ondes TBF dans l'ionosphère, Ann. Geophys., 23, 467, 1967.

Aubry, M. P., Some results of the FR-1 satellite experiment on the VLF wave field in the zone close to the transmitter, J. Atmos. Terr. Phys., 30, 1161, 1968.

Barrington, R. E., J. S. Belrose and W. E. Mather, A helium whistler observed in the Canadian satellite Alouette 2, Nature, 210, 80, 1966.

Brace, L. H., B. M. Reddy and H. G. Mayr, Global behavior of the ionosphere at 1000 kilometers altitude, J. Geophys. Res., 72, 265, 1967.

Brice, N. M., Discrete very low frequency emissions from the upper atmosphere, SEL-64-088, Radioscience Lab., Stanford Electronics Labs., Stanford University, Stanford, California, 1964.

Calvert, W., Steep horizontal electron-density gradients in the topside F layer, J. Geophys. Res., 71, 3665, 1966.

Calvert, W. and T. E. Van Zandt, Fixed-frequency observations of plasma resonances in the topside ionosphere, J. Geophys. Res., 71, 1799, 1966.

Carpenter, D. L., Electron-density variations in the magnetosphere deduced from whistler data, J. Geophys. Res., 67, 3345, 1962.

Carpenter, D. L., Whistler evidence of a "knee" in the magnetospheric ionization density profile, J. Geophys. Res., 68, 1675, 1963.

Carpenter, D. L., N. Dunckel and J. F. Walkup, A new very low frequency phenomenon: whistlers trapped below the protonosphere, J. Geophys. Res., 69, 5009, 1964.

Carpenter, D. L., F. Walter, R. E. Barrington and D. J. McEwen, Alouette 1 and 2 observations of abrupt changes in whistler rate and of VLF noise variations in the plasmapause - a satellite-ground study, J. Geophys. Res., 73, 2929, 1968.

Clemmow, P. C. and J. Heading, Coupled forms of the differential equations governing radio propagation in the ionosphere, Proc. Camb. Phil. Soc., 50, 319, 1954.

Crary, J. H., The effect of the earth-ionosphere waveguide on whistlers, Rept. No. 9, Radioscience Laboratory, Stanford Electronics Labs., Stanford University, Stanford, California, July 1961.

Deeks, D. G., D-region electron distributions in middle latitudes deduced from the reflexion of long radio waves, Proc. Roy. Soc. A, 291, 413, 1966a.

Deeks, D. G., Generalized full wave theory for energy-dependent collision frequencies, J. Atmos. Terr. Phys., 28, 839, 1966b.

Ficklin, B. P., M. E. Mills, L. E. Orsak, L. H. Rorden and R. H. Stehle, Description and operation of the instruments for the Stanford University/Stanford Research Institute Experiment (5002) to be flown on the POGO satellite, Tech. Memo No. 2, Stanford Research Institute, Menlo Park, California, March 1965.

Gurnett, D. A., S. D. Shawhan, N. M. Brice and R. L. Smith, Ion cyclotron whistlers, J. Geophys. Res., 70, 1665, 1965.

Gurnett, D. A., S. D. Shawhan and G. W. Pfeiffer, The hook whistler - a new equatorial whistler observed by Injun 3, UI 66-50, Dept. of Physics & Astronomy, University of Iowa, Iowa City, Iowa, 1966.

Helliwell, R. A., Exospheric electron density variations deduced from whistlers, Ann. Geophys., 17, 76, 1961.

Helliwell, R. A., Whistlers and Related Ionospheric Phenomena, Stanford University Press, Stanford, California, 1965.

Helliwell, R. A., J. H. Crary, J. H. Pope and R. L. Smith, The "nose" whistler - a new high latitude phenomenon, J. Geophys. Res., 61, 139, 1956.

Heyborne, R. L., Observations of whistler-mode signals in the OGO satellites from VLF ground station transmitters, SEL-66-094, Radioscience Lab., Stanford Electronics Labs., Stanford University, Stanford, California, November 1966.

Heyborne, R. L., R. L. Smith and R. A. Helliwell, Latitudinal cutoff of VLF signals in the ionosphere, J. Geophys. Res., 74, 2393, 1969.

Huxley, L. G. H., A discussion of the motion in nitrogen of free electrons with small energies with reference to the ionosphere, J. Atmos. Terr. Phys., 16, 46, 1959.

Leiphart, J. P., R. W. Zeek, L. S. Bearce and E. Toth, Penetration of the ionosphere by very-low-frequency radio signals-interim results of the Lofti experiment, Proc. IRE, 50, 6, 1962.

Mechtly, E. A. and L. G. Smith, Seasonal variation of the lower ionosphere at Wallops Island during the IQSY, J. Atmos. Terr. Phys., 30, 1555, 1968.

Muzzio, J. L. R., Ion cutoff whistlers, J. Geophys. Res., 73, 7526, 1968.

Phelps, A. V. and J. L. Pack, Electron collision frequencies in nitrogen and in the lower ionosphere, Phys. Rev. Letters, 3, 340, 1959.

Piggott, W. R., M. L. V. Pitteway and E. V. Thrane, The numerical calculation of wave fields, reflexion coefficients and polarizations for long radio waves in the lower ionosphere, II, Phil. Trans. Roy. Soc., London, A, 257, 243, 1965.

Pitteway, M. L. V., The numerical calculation of wave fields, reflexion coefficients and polarizations for long radio waves in the lower ionosphere, I, Phil. Trans. Roy. Soc., London, A, 257, 219, 1965.

Pitteway, M. L. V. and J. L. Jespersen, A numerical study of the excitation, internal reflection and limiting polarization of whistler waves in the lower ionosphere, J. Atmos. Terr. Phys., 28, 17, 1966.

Prasad, S. S., Nighttime ionic composition and temperature over Arecibo, J. Geophys. Res., 73, 6795, 1968.

Ratcliffe, J. A., The Magneto-Ionic Theory and Its Applications to the Ionosphere, Cambridge University Press, Cambridge, England (First Edition), 1959.

Reddy, B. M., L. H. Brace and J. A. Findlay, The ionosphere at 640 kilometers on quiet and disturbed days, J. Geophys. Res., 72, 2709, 1967.

Rorden, L. H., R. A. Helliwell and R. L. Smith, An interpretation of LOFTI-I VLF observations, AGARDOGRAPH 74, Pergamon Press, New York, 1964.

Scarabucci, R. R., Analytical and numerical treatment of wave propagation in the lower ionosphere, SEL-69-046, Radioscience Lab., Stanford Electronics Labs., Stanford University, Stanford, California, August 1669.

Sen, H. K. and A. A. Wyller, On the generalization of the Appleton-Hartree magnetoionic formulas, J. Geophys. Res., 65, 3931, 1960.

Shawhan, S. D., VLF ray tracing in a model ionosphere, UI-66-33, Dept. of Physics & Astronomy, University of Iowa, Iowa City, Iowa, August 1966.

Smith, R. L., Propagation characteristics of whistlers trapped in field-aligned columns of enhanced ionization, J. Geophys. Res., 66, 3699, 1961a.

Smith, R. L., Properties of the outer ionosphere deduced from nose whistlers, J. Geophys. Res., 66, 3709, 1961b.

Smith, R. L. and J. J. Angerami, Magnetospheric properties deduced from OGO-I observations of ducted and nonducted whistlers, J. Geophys. Res., 73, 1, 1968.

Smith, R. L., R. A. Helliwell and I. Yabroff, A theory of trapping of whistlers in field-aligned columns of enhanced ionization, J. Geophys. Res., 65, 815, 1960.

Storey, L. R. O., An investigation of whistling atmospherics, Phil. Trans. Roy. Soc., London, A, 246, 113, 1953.

Storey, L. R. O., Resultats preliminaires sur la propagation TBF dans la basse magnetosphere obtenus par la satellite FR-1, Space Res. VII, North-Holland Publ., Co., Amsterdam, p. 588, 1966.

Terman, F. E., Electronic and Radio Engineering, McGraw Hill Book Co., Inc., New York, (4th Edition), 1955.

Wait, J. R., Electromagnetic Waves in Stratified Media, Pergamon Press, New York, 1962.

Walter, F., Nonducted VLF propagation in the magnetosphere, SEL-69-061, Radioscience Lab., Stanford Electronics Labs., Stanford University, Stanford, California, October 1969.

Walter, F. and J. J. Angerami, The nonducted mode of VLF propagation between conjugate hemispheres; observations on OGO's 2 and 4 of the 'walking-trace' whistler and of Doppler shifts in fixed frequency transmissions, J. Geophys. Res., 74, December 1, 1969.